POLITECNICO
MILANO 1863

SCUOLA DI INGEGNERIA INDUSTRIALE
E DELL'INFORMAZIONE

Data-driven, class-based kinetic modeling of oxymethylene ethers combustion

Tesi di Laurea Magistrale in
Chemical Engineering - Ingegneria Chimica

Author: **Amedeo Puri**

Student ID: 97515
Advisor: Prof. Alessandro Stagni
Co-advisors: PhD. Timoteo Dinelli, PhD. Alessandro Pegurri
Academic Year: 2021-22

Publications and conferences

Conferences

- Amedeo Puri, Timoteo Dinelli, Alessandro Pegurri and Alessandro Stagni. Data-driven, class-based optimization methodology for the kinetic modeling of oxymethylene ethers (OME_{1-4}) combustion. In *11^{th} European Combustion Meeting*, Rouen, France, 26-28 April 2023.
- Amedeo Puri, Luna Pratali Maffei, Timoteo Dinelli, Alessandro Pegurri and Alessandro Stagni. Data-driven, class-based optimization methodology for the kinetic modeling of oxymethylene ethers (OME_{1-4}) combustion. In *16^{th} International Conference on Engines & Vehicles for Sustainable Transport*, Capri, Naples, Italy, 10-14 September 2023.

Abstract

Due to the vast array of variables present in combustion experiments, such as operating conditions and equipment type, a kinetic model needs to be capable of predicting combustion process changes across diverse environments. Literature provides numerous mechanisms containing thousands of reactions and species; however, due to the large number of reactions, the kinetic constants cannot be measured experimentally or calculated with high-level theories. Therefore, kinetic constants are typically assigned through reaction classes or rate rules, which classify reactions into specific groups based on common features or functional dependencies, assigning reference values for kinetic constants and propagating them throughout the class. This method ensures kinetic consistency in the mechanism obtained. Although literature provides numerous examples of parameter optimization to improve agreement with experimental data, the systematic perturbation of parameters for individual reactions without considering their overall interaction is not reasonable. This approach may perform well mathematically, but it can disrupt the consistency between kinetically similar reactions.

In this work, a reaction-class-based optimization is performed, where reaction-class kinetic constants are calibrated instead of perturbing each parameter differently. This guarantees obtaining a more consistent yet physically sound model. The methodology presented has been applied, as a case study, to the optimization of the $OME_{1\text{-}4}$ model, selecting as the optimization targets seven different classes of reaction identified through a sensitivity analysis carried out over the range of interest. After the optimization, a validation of the kinetic mechanism is performed over a wide range of experimental conditions in order to evaluate the mechanism's performance by considering a variety of properties, including Ignition Delay Times in Shock Tubes, speciations in Jet Stirred and Plug Flow Reactors, and Laminar Flame Speeds. This comprehensive validation ensures that the optimized mechanism is accurate and predictive over a range of conditions, and can be used with confidence for further analysis and simulations.

At the end of the study, the final kinetic mechanism was compared with both the detailed and the lumped mechanisms, highlighting that the new mechanism generally outperforms the old ones while maintaining physical consistency. The obtained results pave the way

for a broader field of research, where not only the optimization but also the generation of kinetic mechanisms for heavier OMEs could be explored.

Keywords: Optimization, Reaction classes, e-fuel, kinetic-modeling

Sommario

In virtù dell'ampia gamma di variabili presenti negli esperimenti di combustione, come le condizioni operative e il tipo di attrezzatura, un modello cinetico deve essere in grado di prevedere i cambiamenti del processo di combustione in diversi ambienti. La letteratura scientifica offre numerosi meccanismi che includono migliaia di reazioni e specie chimiche; tuttavia, a causa del grande numero di reazioni coinvolte, le costanti cinetiche non possono essere misurate sperimentalmente o calcolate con teorie avanzate. Pertanto, di solito, le costanti cinetiche vengono assegnate tramite classi di reazioni o rate-rules. Le reazioni sono quindi raggruppate in classi specifiche in base a caratteristiche comuni o dipendenze funzionali rispetto ai reagenti o ai prodotti, assegnando valori di riferimento per le costanti cinetiche e propagandoli all'interno della classe. Tale metodo garantisce, altresì, la coerenza cinetica del meccanismo ottenuto. Sebbene la letteratura scientifica fornisca numerosi esempi di ottimizzazione dei parametri per migliorare la corrispondenza con i dati sperimentali, la perturbazione sistematica degli stessi per singole reazioni senza considerare la loro interazione complessiva non è ragionevole. Tale approccio, infatti, potrebbe funzionare bene dal punto di vista matematico, ma non preserverebbe la coerenza tra reazioni cineticamente simili.

In questo lavoro, si è svolta un'ottimizzazione basata sulla classificazione delle reazioni, in cui sono state calibrate le costanti cinetiche delle classi di reazioni anziché perturbare ciascun parametro separatamente. L'uso di questa metodologia ha permesso di arrivare ad un modello più coerente e fisicamente corretto. L'approccio proposto è stato applicato come case-study all'ottimizzazione del modello $OME_{1\text{-}4}$, selezionando come obiettivi di ottimizzazione sette diverse classi di reazioni identificate attraverso un'analisi di sensitività condotta nell'intervallo di interesse. Dopo l'ottimizzazione, si è eseguita una validazione del meccanismo cinetico su una vasta gamma di condizioni sperimentali per valutare le sue prestazioni considerando una varietà di proprietà, tra cui i Tempi di Ignizione in Shock Tubes, speciazioni in reattori Jet Stirred e Plug Flow e Velocità di Fiamma Laminare. Questa validazione completa assicura che il meccanismo cinetico ottimizzato sia accurato e predittivo in una vasta gamma di condizioni.

Il meccanismo cinetico così ottimizzato è stato quindi confrontato con il dettagliato e il

lumped, evidenziando un generale miglioramento garantendo però una consistenza fisica. I risultati ottenuti aprono la strada ad un nuovo campo di ricerca, in cui sarà possibile applicare questa procedura non solo per ottimizzare meccanismi ma anche generarne di nuovi per OME più pesanti.

Parole chiave: Ottimizzazione, Classi di reazioni, e-fuel, Modellazione cinetica

Contents

List of Figures

List of Tables

List of Abbreviations

Abbreviations	Description
SSP	Shared Socioeconomic Pathways
DME	DiMethyl Ether
DMM	DiMethoxy Methane
OME	OxyMethilene Ether
SMR	Steam Methane Reforming
PtF	Power to Fuel
GA	Genetic Algorithms
CM	Curve Matching
CFD	Computational Fluid Dynamics
IDT	Ignition Delay Times
LFS	Laminar Flame Speed
PFR	Plug Flow Reactor
JSR	Jet Stirred Reactor
ST	Shock Tube
RCM	Rapid Compression Machine
NTC	Negative Temperature Coefficient

List of Symbols

Variable	Description	SI unit
$\boldsymbol{A}$	pre-exponential factor	mol/cm^3/s
$\boldsymbol{\beta}$	temperature exponential	-
$\boldsymbol{E_a/R}$	activation energy	cal/mol
$\boldsymbol{f}$	uncertainty factor	-
$\boldsymbol{P}$	Pressure	bar
$\boldsymbol{R}$	Universal gas constant	cal/mol/K
$\boldsymbol{k}$	Kinetic constant	$(mol/cm^3)^{(1-n)}/s$
$\boldsymbol{\phi}$	Fuel-Air Equivalence ratio	-
$\boldsymbol{\lambda}$	Air-Fuel Equivalence ratio	-
$\boldsymbol{\nu}$	Stoichiometric coefficient	-
$\boldsymbol{x}$	Molar fraction	-
$\boldsymbol{s}$	sensitivity coefficient	-
$\boldsymbol{T}$	Temperature	K
$\boldsymbol{t}$	time	s

1 | Introduction

The climate has always played a key role in the development of the human race, but it could also be the cause of its end. The increasing number of catastrophic phenomena that are happening during these years demands a solution. After the COP XXVI in Glasgow in October 2021, Nations agreed on the need to focus on renewable energy and stop using fossil fuels, so that by 2050 the rise in temperature will reach a maximum of 1.5 degrees with respect to the 1850-1900. The COP XXVII was intended to be a forum for reconfirming the proposals from the previous year, but the invasion of Ukraine by the Russian Federation completely shifted the focus of the event. The Prime Ministers and their foreign ministers had to find a solution to the cost of the gas and electricity, which since the beginning of the war is continuously rising due to the european sanctions towards Russia [36]. Even if the average annual GHG emissions the rate of growth between 2010 and 2019 (1.3% per year) was lower than that between 2000 and 2009 (2.1% per year) [1], still the last 30 years are the most critical ones. Historical cumulative net CO_2 emissions from 1850 to 2019 were 2400±240 $GtCO_2$. Of these, more than half (58%) occurred between 1850 and 1989 [1400±195 $GtCO_2$], and about 42% between 1990 and 2019 [1000±90 $GtCO_2$] [1]. According to the new 2023 report by IPCC (Intergovernmental Panel on Climate Change) there are very few possibilities to not overcome the 1.5°C limit global warming, at the actual time Global GHG emissions in 2030 associated with the implementation of Nationally Determined Contributions (NDCs) announced prior to COPXXVI would make it harder to limit warming below 2°C if no additional commitments are made or actions taken. The actual NDCs would be similar to or only slightly below 2019 emission levels and higher than those associated with modelled mitigation pathways that limit warming to 1.5°C [1] (Fig.1.1a).The assessment in [1] indicates that there is a high likelihood that the global temperature will surpass the 1.5°C threshold in the 21st century, thereby rendering the SSP1-1.9 scenario almost unattainable. Immediate action needs to be taken to mitigate the situation.

There are several risks associated with exceeding the 1.5°C global warming limit. In most regions of Africa, Asia, North America and Europe, heavy precipitation and flooding

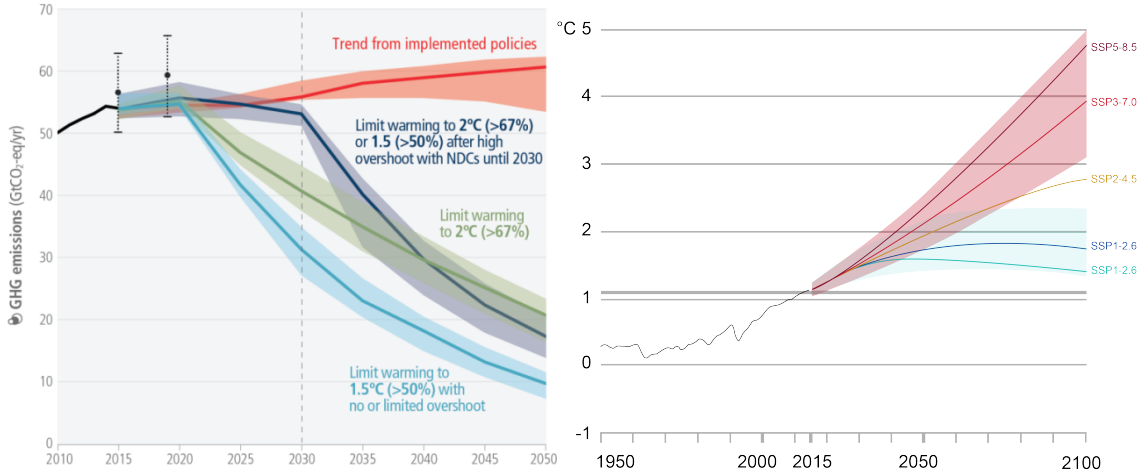

(a) Global GHG emissions [1].

(b) Temperature for SSP-based scenarios over the 21^{st} century [1].

Figure 1.1: GHGs emissions and Temperature projection [1].

events are expected to intensify and occur more frequently. If the increase of temperature reaches 2°C or higher, these changes are projected to expand to more regions and become even more significant. Additionally, more frequent and severe agricultural and ecological droughts are expected in Europe, Africa, Australasia, and North, Central and South America. Other anticipated regional changes include an increase in the intensity of tropical cyclones and/or extratropical storms, as well as increases in aridity and fire weather, as shown in Figure 1.2. It is important to note that the transportation sector is the second largest emitter of greenhouse gases, as shown in Figure 1.3. The emissions from this sector contribute to the global warming phenomenon, which is caused by greenhouse gases such as carbon dioxide (CO_2), methane (CH_4), nitrous oxide (N_2O), hydrofluorocarbons (HFCs), perfluorocarbons (PFCs), sulphur hexafluoride (SF_6), and natrium trifluoride (NF_3), as outlined in a report by the EEA [2]. These gases have the ability to absorb energy and slow the rate at which energy escapes to space, thus warming the Earth. Different greenhouse gases have varying effects on global warming due to their radiative efficiency and lifetime in the atmosphere.

To tackle this issue, the EU has recently approved a package of laws called *fit for 55*, which aims to reduce climate-damaging emissions by 55% by 2030 compared to 1990 levels and achieve climate neutrality by 2050 [37]. The package includes a specific section for the transportation sector, which mandates that all new cars entering the market from 2035 should be zero-emission vehicles.

According to this, electric vehicles seem to be the natural choice but as far as fossil fuels are

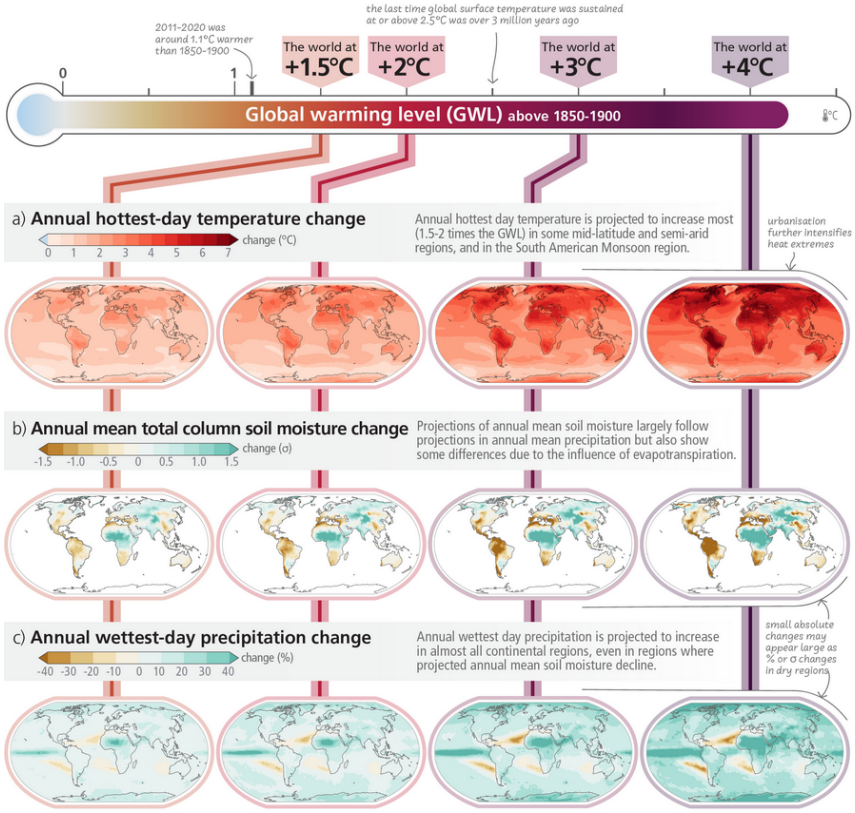

Figure 1.2: Projected changes of annual maximum daily temperature, annual mean total column soil moisture CMIPand annual maximum daily precipitation at global warming levels of 1.5°C, 2°C, 3°C, and 4°C relative to 1850–1900 [1].

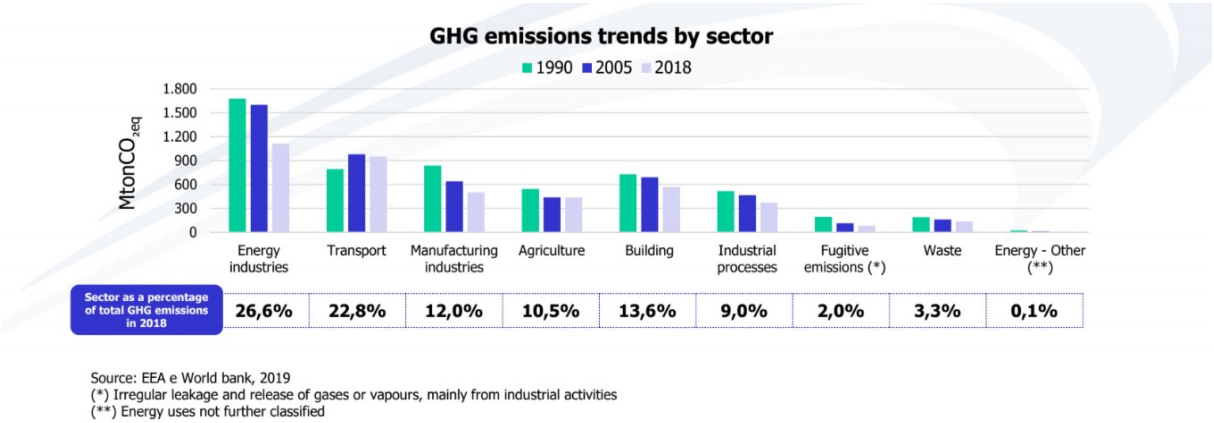

Figure 1.3: GHG emissions per sector [2].

used to produce the electricity needed, instead of nuclear energy or renewable energy, the problem is only shifted. According to the IEA, the current sources of electrical energy are presented in Figure 1.4. From 2010 to 2019, there have been sustained decreases in the unit costs of solar energy (by 85%), wind energy (by 55%), and lithium-ion batteries (by 85%),

and large increases in their deployment. Electricity from PV and wind is now cheaper than electricity from fossil sources in many regions, electric vehicles are increasingly competitive with internal combustion engines, and large-scale battery storage on electricity grids is increasingly viable[1][36]. However, in addition to the issues related to the disposal of lithium batteries and the high cost of the raw materials required to produce them, which have been exacerbated by the current market crisis, another pressing problem is that the existing electric grid is unable to meet the increasing demand. Therefore, short-term solutions involving the use of e-fuels appear to be the most viable option.

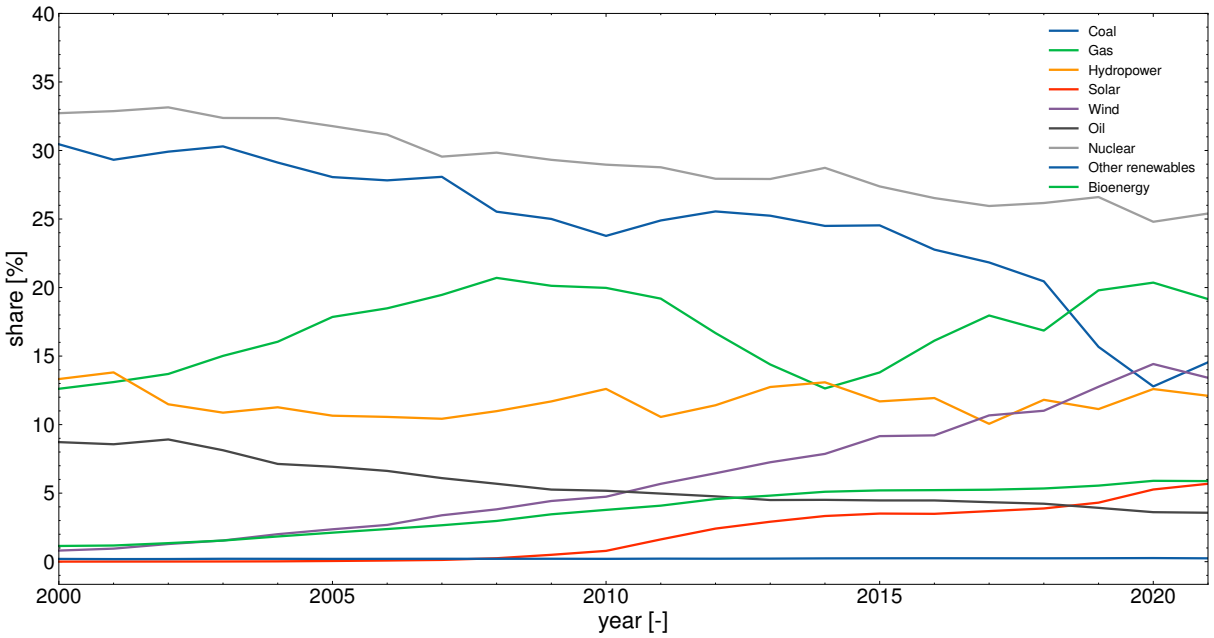

Figure 1.4: Share of energy production by source, Europe 2000-2021 [3].

E-fuels, where "e" stands for electro, are a type of fuel that stands out from the broader family of fuels due to their unique manufacturing process. E-fuels are produced using carbon dioxide (CO_2) and hydrogen (H_2) as raw materials, which are combined through the process of hydrogenation. Hydrogen is typically obtained through the electrolysis of water, while carbon dioxide can be sourced through direct air capture or from a point source[4] (Fig. 1.5). E-fuels have a major advantage in that they can be utilized in engines designed for fossil fuels and transported via pipelines built for traditional gasoline and other fuels. However, their primary drawback is their high cost in comparison to fossil fuels, owing to the cost of producing hydrogen via electrolysis, which ranges from 2.5-10 US dollars per kilogram of hydrogen (H_2) [36]. Although hydrogen can be produced through steam methane reforming at a relatively low cost of 1-2 US dollars per kilogram of hydrogen (H_2) [36], using this method would defeat the purpose of using e-fuels since it still relies on traditional fuels. Despite this, many projects are utilizing this technology,

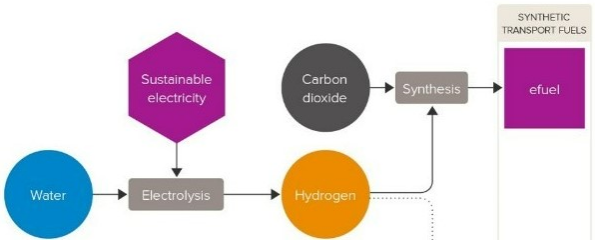

Figure 1.5: Overview of the production process of a generic e-fuel [4].

and according to the IEA annual report [36], global electrolysis capacity could reach 134-240 GW by 2030. In recent years, the production of hydrogen via electrolysis has gained popularity due to the availability of a wide range of machinery that can produce this compound, such as SOEC, PEM or Alkaline [38–40]. The key factor in the entire process is the method by which the electric energy is produced, as highlighted in Figure 1.4. Thanks to current policies, the so-called "green-hydrogen" is experiencing a boost. As shown in Figure 1.6, it is expected that the EU will play a key role as manufacturer of hydrogen.

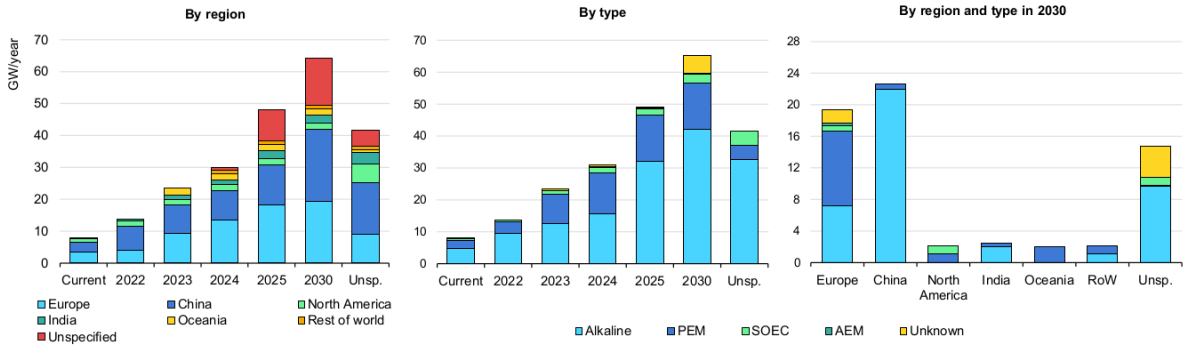

Figure 1.6: Electrolyser manufacturing capacity by region and type to 2030 [5].

The "Unsp" reportd in Fig. 1.6 in year includes manufacturing facilities for which the start year is unknown; while the "Unsp" in region includes manufacturing facilities for which the geographical location is unknown [5].

1.1. Oxymethylene Ethers (OMEs)

OMEs are organic compounds that contain a CH_2O group in their structure, with a methylene group (i.e. CH_3) at the ends. Generally, their structure can be summarized as $CH_3O[CH_2O]_nCH_3$. The number of times this group appears in the molecule determines its nomenclature, for instance, the simplest one is DiMethyl Ether (DME), which is known

as OME_0. The next one is DiMethoxy Methane (DMM), referred to as OME_1, and other OMEs are named based on the number of $[CH_2O]$ groups present in the molecule, as shown in Fig.1.7.

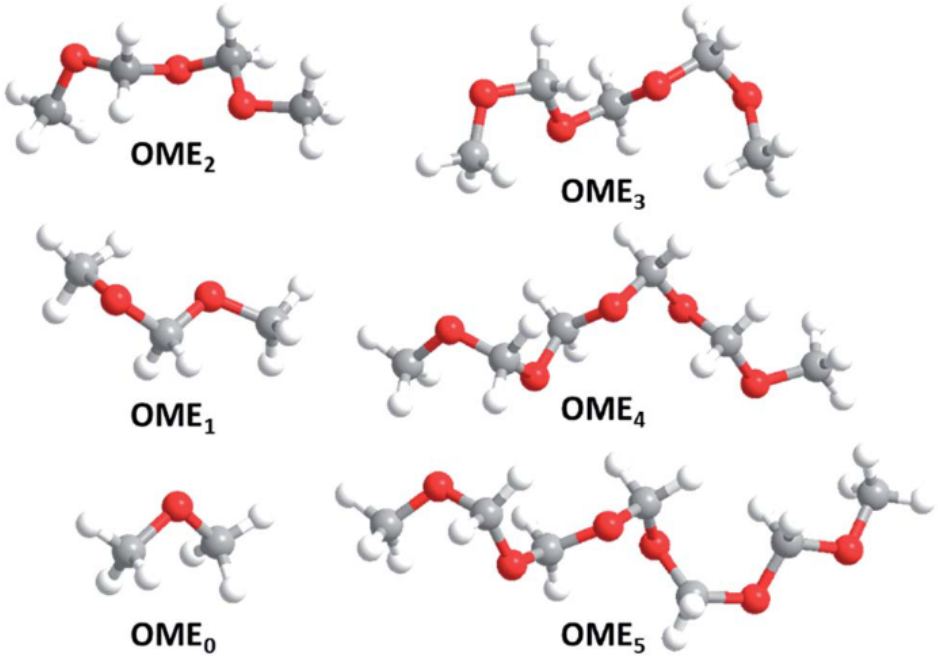

Figure 1.7: OME from 0 to 5, grey C, white H, red O [6].

The interest shown by the scientific community towards this family of compounds is due to the high oxygen content and the absence of carbon-to-carbon bonds, both factors lead to practically soot-free combustion because it inhibits the formation of soot precursors such as acetylene (C_2H_2) in the combustion process, as pointed out by Sun et al.[41]. Another critical point, which increases the interest in these compounds, is their good auto-ignition characteristics for compression-ignition engine applications. There are many studies [23, 35, 42] which show promising results when the OMEs are used as diesel fuel substitutes or additives, in particulate for $OME_{3\text{-}6}$ due to the higher flash point and higher kinematic viscosity.

1.1.1. Properties

When it comes to OMEs, their ability to reduce soot formation during combustion is a crucial factor. This is because OMEs contain activated methylene groups next to oxygen atoms ($–O–CH_2–$) in their chemical structure, which lead to the formation of hydroperoxides (OME-QOOH) in the early stages of combustion. These hydroperoxides then decompose into OH-radicals, which subsequently degrade soot precursors through oxidative

processes [43] (see also the Jacobs et al. [44]). As a result, OMEs are able to significantly reduce soot formation during combustion in diesel engines [8].

DMM and DME are limited as fuels due to their physical properties. DMM has a high boiling point and low volatility, which makes it difficult to mix with diesel fuel and leads to poor combustion performance. DME, on the other hand, has a low boiling point and high vapor pressure, which can cause problems with fuel storage and handling. Additionally, its low viscosity can affect the fuel injection system in diesel engines, making it challenging to use DMM and DME as fuels without significant modifications to the engine and fuel systems. However, the addition of DME to diesel fuel, starting with the simplest OME, has been shown to increase vapor pressure and lower viscosity, according to [45]. Although this can lead to a reduction of solubility at lower temperatures [45], engine modifications can be made to accommodate the increase in vapor pressure and changes in injection behavior resulting from the lower viscosity [46]. Due to similar reasons, DMM is also not used.

Despite these limitations, many authors have pointed out that OMEs starting from 2 have enormous potential, with their higher viscosity and lower flash points making them easy to add to diesel fuel and use in common diesel engines, as shown in Table 1.1.

Properties	**OME_1**	**OME_2**	**OME_3**	**OME_4**	**OME_5**	**OME_{3-5}**	**Fossil Fuel**
Density at 15°C (g/cm^3)	0.859	0.978	1.031	1.074	1.106	1.057	0.835
Oxygen (wt%)	42.1	45.2	47	48.1	48.9	48	≃0
Cetane number	24	64	71	82.5	95	80	54
Flash point (°C)	-32	12	51	84	112	62	>55
Boiling point (°C)	42	105	156	202	242	140-318	200-360
Melting point (°C)	-	-70	-4.3	-10	18	-18	≃-9
Vapor pressure at 25°C (mbar)	485	238	40	7	1.3	-	≃10
Kin. viscosity at 40°C (mm^2/s)	0.37	-	-	-	-	1.2	2-4.5
Lubricity (μm)	759	-	53.4	465	437	386	<460
lower heating value (MJ/I)	20.15	20.19	20.3	20.4	20.45	21	35.6
h_{vap} at 15°C rel. to heating value (%)	1.54	1.34	1.24	1.17	1.11	≃1.2	0.8

Table 1.1: Fuel properties of OME_n and fossil diesel complying to the EN590 Norm. [35].

The mix of column 7 is the commercially available OME mixture, it is as follows: 0.1 wt% OME_1, 0.2 wt% OME_2, 45 wt% OME_3, 25 wt% OME_4, 17 wt% OME_5, 7 wt% OME_6, 3 wt% OME_7, 1 wt% OME_8 [35].
As it is possible to notice from the table 1.1, the cetane number of $OME_{2\text{-}5}$ is between 64 and 95, higher than the one of the common diesel, which is only 54. This is also another reason why OMEs are so attractive as alternative fuels. Another important property is the flash point, due to safety reasons. While for $OME_{1\text{-}2}$ this value is way too low, the $OME_{n>3}$ show a flash point higher than the one of diesel. The problem related to the OMEs is with the longer ones because they could precipitate at low temperatures and

could clog filters or other parts of the fuel system.

1.1.2. Synthesis

The synthesis of the OMEs (from 1 to n) is based on methanol as raw material, the process chain can be seen in Fig.1.8. As it is possible to notice from Fig.1.8, to produce OMEs two intermediates must be produced, both starting from formaldehyde (CH_2O), mainly produced via the Silver process (Oxidative dehydrogenation of methanol) [47].

1. Trioxane process (Anhydrous process): trimerization of formaldehyde, usually catalyzed by H_2SO_4 [48] (preferred method)
2. Methyal (DMM) process (Aqueous process): heterogeneously catalyzed reactive distillation [49]

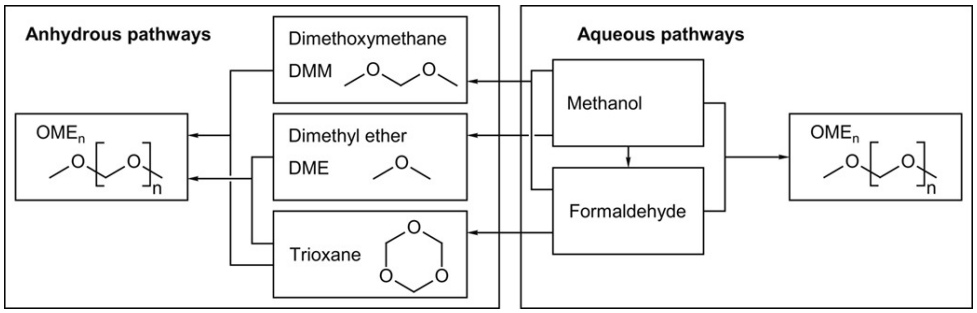

Figure 1.8: Synthesis pathways for OME[7].

The mechanism of production of the OMEs (Fig. 1.9) through the anhydrous process, once the two intermediates are produced, consists of 3 steps:

1. trioxane is converted to formaldehyde over an acidic catalyst -
2. Formaldehyde, the monomer of OMEs, oligomers and reacts with DMM to OME_2
3. OME_2 reacts with formaldehyde to give OME_{n+1}

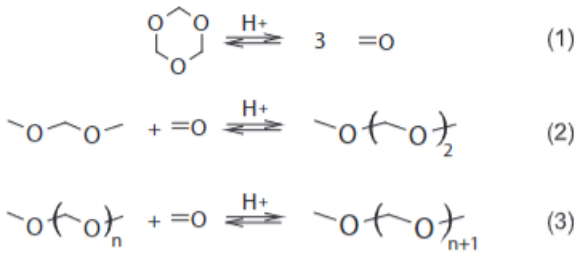

Figure 1.9: Reaction scheme of the POMDME formation [8].

Once the reaction is carried out, there is a train distillation through which the mixture of interest, typically $OME_{3\text{-}4}$ is carried out, while the others are recycled back to the reactor. As pointed out by Hackbarth et al. [7], the advantages of this strategy are a high OME selectivity, low amounts of by-products and a comparatively simple product separation, usually by distillation.

In recent years, a promising approach has emerged that involves the direct synthesis of OMEs from methanol and formaldehyde (the second process summarized in Figure 1.8). However, this method has its drawbacks, such as the formation of by-products, particularly hemiacetals due to incomplete acetalization, as well as water from acetalization reactions, which need to be separated from the reaction mixtures [7]. Compared to the Trioxane process, the OME yields are significantly lower, and the $OME_{1\text{-}5}$ content in the product mixtures is typically around 35% (compared to 70% in the anhydrous process). Nonetheless, recent progress has been made to overcome these challenges. For example, Schmitz et al. [50] have designed a new process that includes a significantly improved distillation procedure, while Oestreich et al. [51, 52] have proposed an extraction method for the work-up of aqueous OME mixtures.

The problem related to both of these processes is methanol. As widely known, methanol is produced through the hydrogenation of CO [47]. Nowadays the H_2 needed for the process is mainly produced via SMR due to economic and efficiency reasons (see Figure 1.6). This means that the production of the OME through the process presented in Fig. 1.8 is not environmentally feasible until the production of CH_3OH is carried out in a zero-emission way. Recently a very promising route of production of methanol has gained attention: the direct hydrogenation of CO_2 [47]. This process, based on an In_2O_3/ZrO_2 much more selective than the common CZA catalyst (Cu Zn Al_2O_3, Copper, Zinc and Alumina respectively), has shown promising results thanks to the demonstrative plant based in Iceland. The plant uses the CO_2 emitted by a nearby geothermal power plant. The carbon dioxide is then purified to make it suitable for downstream methanol synthesis and compressed. The hydrogen needed is produced via electrolysis of water and added to carbon dioxide into the reactor. The last step is the purification of methanol from water through distillation. The production of methanol is about 4000 tons per year, using a total of 5500 tons per year of CO_2 [53].

The other and more interesting, from an environmental point of view, route to produce OMEs is based on the reaction of green H_2, hydrogen produced via electrolysis powered by renewable energy, and CO_2. From Fig. 1.10 it is possible to notice the two routes suggested by Deutz et al.[9] both starting from methanol, which is produced from CO_2 combined via catalytic reduction with hydrogen.

1. First route (Scheme 1, Fug. 1.10): DMM is produced via a condensation reaction from methanol and formaldehyde (FA) [9, 54, 55]. However, since the production of formaldehyde first involves an oxidative step, the overall route is redox-inefficient.
2. Second route (Scheme 2, Fig. 1.10): Deutz et al. consider a purely reductive approach to produce DMM which was recently demonstrated based on the direct transformation of methanol with CO_2/H_2 to catalytically generate the central CH_2-unit of the OME molecule [9, 56, 57].

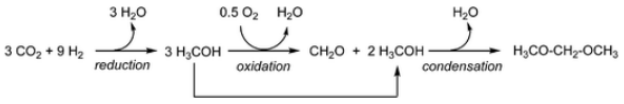

Scheme 1

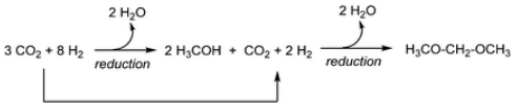

Scheme 2

Figure 1.10: Two main possible pathways of DMM synthesis from CO_2 and renewable H_2 [9].

1.2. Reaction classes

Studying the combustion mechanism of OMEs is crucial in developing more efficient combustion techniques that aim to reduce environmental impact, diversify energy sources, and utilize them wisely. As Lu et al. [10] state, the development of kinetic mechanisms that can describe the oxidation and pyrolysis of various fuels is essential in achieving this goal. Combustion is a complex process that involves a wide range of chemical reactions and a large number of species (Fig. 1.11). To accurately model and predict the combustion process, it is necessary to use a kinetic mechanism, which is a set of variables that describe the chemical reactions and their kinetics. The model includes the Arrhenius rate parameters for each reaction, which describe the formation and consumption of each chemical species in the combustion process. Because combustion experiments can be performed under a wide range of conditions, a kinetic model needs to be able to predict the combustion process reasonably well across the entire operating space. The rate constants can be determined experimentally, computed with quantum chemistry tools, or estimated based on

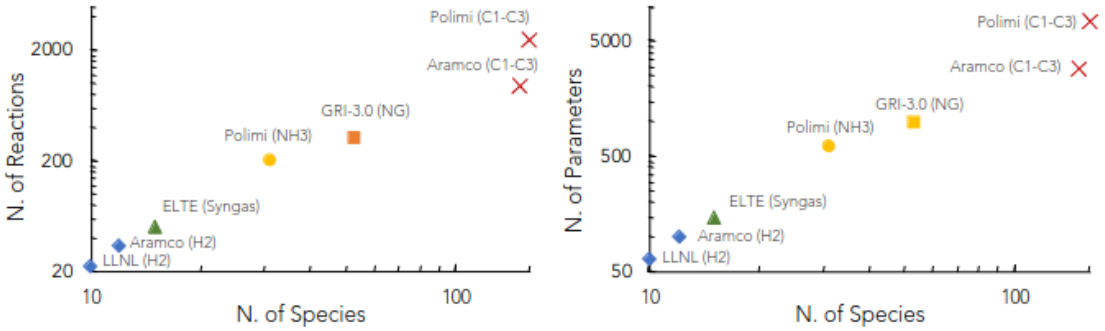

Figure 1.11: Size of some detailed mechanisms for hydrogen, ammonia, natural gas and low-hydrocarbons available in literature. Adapted from Lu and Law [10], courtesy of Andrea Bertolino [11].

analogies with similar compounds for which kinetic subsets already exist [58, 59]. During the last decade, the determination of the rate constants for the kinetic mechanism was characterized by the massive employment of even more sophisticated theoretical methods (e.g. ab initio transition state theory-based master equation, AI-TST-ME [60]). This was justified by the improved theoretical methods and algorithms currently available, and by the capability of measuring rate constants for elementary steps in a more accurate way, thus providing an immediate validation target for the theoretical results [60–63].

However, adopting the ”best” rate constant parameters may not result in better model performance, particularly when considering a broad spectrum of experimental targets [59, 64]. This is due to multiple reasons, not least the fact that in the majority of the models, the rate parameters were estimated by means of analogy rules and semi-empirical correlation for the estimation of the thermodynamics and transport properties moreover every rate constant is affected by uncertainty [64, 65]. Therefore, due to the intrinsic hierarchical nature of detailed mechanisms and due to the way they are developed, introducing a single accurate rate parameter or a new one for an entire reaction class, might strongly perturb the equilibrium and the consistency between different modules.

In the development process of a kinetic mechanism, the determination of the kinetic constants is followed by the tune of these rate parameters by means of comparison against experimental or computational data. Typically, performing a sensitivity analysis on rate parameters allows choosing the important rate constants which are needed to be tuned [66]. The tuning of the rate constant can be performed manually or automatically through an optimization procedure by minimizing or maximizing an objective function. Then an adapted set of rate constants is reached after the iterative optimization procedure and a good agreement between model prediction and experimental data can be obtained.

Recently, several frameworks were developed to automate the tuning process of the rate parameters [15, 67–69]. However, all of them perturb each parameter independently not considering the underlying consistency between the reaction classes. In literature there are several examples of parameters optimization [67–70] with the purpose of obtaining a better agreement with the experimental data, however parameters for each reaction are systematically perturbed not paying attention to their overall interaction. Therefore, reactions are often grouped into classes based on their common features or functional dependencies, and a reference value for the kinetic constant is assigned to the entire class [58]. This method is called reaction class optimization, and it is used to ensure the kinetic consistency of the mechanism. The goal of this method is to preserve the physical consistency of the mechanism by treating in the same way kinetically similar reactions equally, while also addressing the optimization challenges that arise during the process. An attempt towards reaction class-based optimization has been made by Cai et al. [71], where they optimized the rate-rules of n-heptane combustion kinetic mechanism.

In this work, a reaction-class-based optimization is presented, where the reaction class kinetic constants are calibrated instead of perturbing each parameter differently. This allows obtaining a consistent yet physically sound model. The overall optimization process has been implemented as an extended capability of `OptiSMOKE++` [15], a code suite for modeling reactive flows through detailed kinetics, for the first time. The methodology presented has been applied, as a case study, to the optimization of the $OME_{1\text{-}4}$ model, selecting as the optimization targets different classes of reaction identified through a sensitivity analysis carried out with `OpenSMOKE++` [72] and post-processed with `PySMOKEPostProcessor`. The case study is the kinetic combustion mechanism of oxymethylene ethers (OMEs). The ultimate purpose of the present work is to present a new way to optimize a kinetic mechanism taking into account of the physical consistency that the reactions belonging to different classes must ensure. After the optimization, a validation over a wide range of experimental conditions has been automatically performed exploiting `SciExpeM` [73] as a framework.

1.3. Aim and structure of the thesis

This work is organized as follows: **Chapter 2** presents the methodology adopted in this work, with a focus on the tools most commonly used in the optimization of kinetic mechanisms. **Chapter 3** details the tools used in the study. It starts with the description of how `OptiSMOKE++` works, then the identification of the most selective reaction through the use of `pySMOKEPostProcessor`, followed by the test case on two kinetic mechanisms

exploiting a first approach to class-based optimization: the substitution method. After highlighting the critical points of this first method and the need for more accuracy, the calculation of scaling factors based on the detailed mechanism was computed. Finally, the methodology involves optimizing the lumped mechanism using `OptiSMOKE++` applying reaction classes with the proper scaling factor is presented, highlighting the optimization targets. **Chapter 4** presents the results obtained with this new approach processed within `OpenSMOKE++` and the comparisons with other experiments through the use of `SciExpeM`. Finally, **Chapter 5** discusses the conclusion and future work, including possible applications of this mechanism.

2 | Methodology

The purpose of this chapter is to provide an overview of the theoretical concepts underlying the methods employed in this thesis for kinetic modeling, optimization, scaling factor determination, uncertainty factor and sensitivity analysis.

2.1. Kinetic Modeling

The kinetic mechanism, describing the oxidation and pyrolysis of DMM and higher OMEs was built up following the principles of hierarchy and modularity starting from the `CRECK` kinetic framework [58, 74, 75]. For the past 20 years, the `CRECK modelling group` at Politecnico di Milano has been creating a kinetic mechanism for the oxidation and pyrolysis of various fuels, ranging from hydrogen and methane to complex ones like diesel and jet fuels. The objective of this universal model is to assist in designing effective combustion devices by precisely describing the production of harmful substances such as Nitrogen Oxides (NO_x), Polycyclic Aromatic Hydrocarbons (PAH), and soot. The group has implemented two simplifying concepts, Hierarchy and Modularity, as constructing a complex mechanism all at once is not feasible because of the huge quantities of information needed. Regardless of the oxidized fuel, the same set of small molecules will be generated eventually. Therefore, when examining the combustion of a new molecule, the model can be quickly modified and updated by assessing only the set of reactions specific to the new molecule. The subgroup of reactions at a higher hierarchical level will remain unchanged (see Figure 2.1). The modules referred to H_2/O_2 and C_1-C_2 had been adopted according to Metcalfe et al. [77] and subsequently improved from the work of Bagheri et al. [74]. The module referred to C_3 has been added from the work of Burke et al. [78]. Then the DME oxidation pathways for low and high temperature was obtained from Burke et al. [79] and improved by Stagni et al. [12], in order to have a better prediction of intermediate species such as formic (HOCHO) and carbonic (HOCOOH) acid. Furthermore the H-abstraction reactions by H, HO_2, and CH_3 were updated accordingly to the work of Cavallotti et al. [80] (see Fig. 2.2).

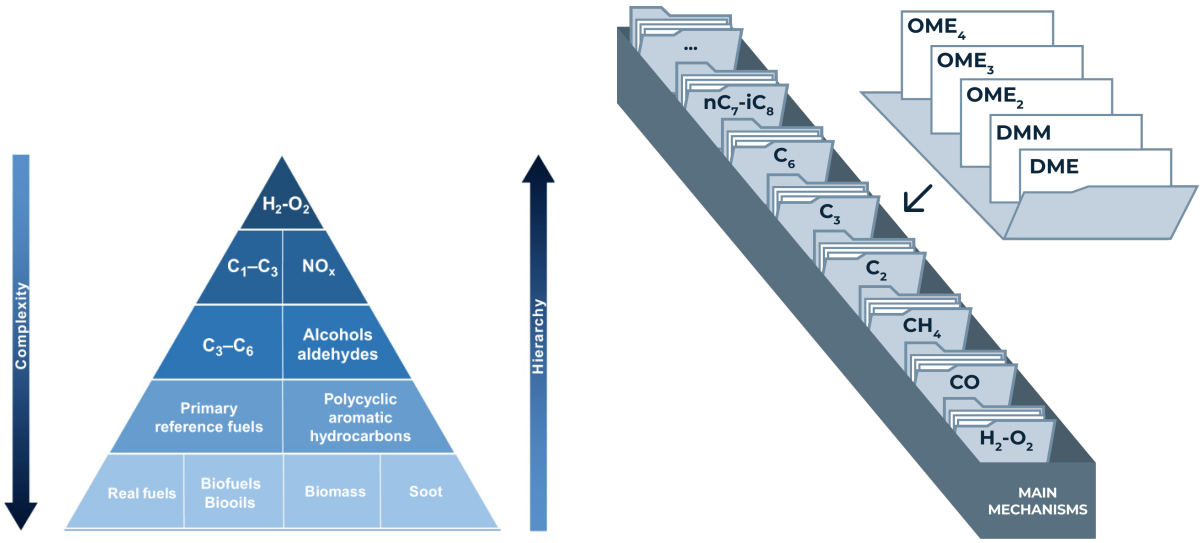

(a) Hierarchical approach for the species contained in the mechanism [76].

(b) Modular approach when inserting the mechanism of a new set inside the general mechanism.

Figure 2.1: Hierarchical and Modular approaches used in the mechanism developed by the `Creck modeling group` at the Politecnico of Milano

The DMM sub-mechanism was integrated from the work of Jacobs et al. [44] with minor modifications. Then higher OMEs (s = 2-4) were taken from the sub-mechanism proposed by Cai et al. [23], which was generated, adopting a reaction class-based methodology with the principle of hierarchy in order to obtain an automatic generation process for the reactions and their kinetic parameters. The model of Cai was built upon taking as a reference the model of Jacobs. The detailed model, so obtained, consists of 282 species and 2657 reactions (see Fig. 2.3).

Then the detailed model underwent an automatic lumping procedure. The primary objective of the chemical lumping technique is to minimize the number of species and reactions in a model while maintaining a high level of precision. To achieve this, various species are combined into single pseudospecies with averaged thermodynamic and transport characteristics. As a result, the rates of reactions must be adjusted accordingly to account for the merging of reactants and products. The final lumped model consists of 176 species and 2486 reactions. The resulting mechanism is the one that underwent the numerical optimization by reaction classes explained in the next sections.

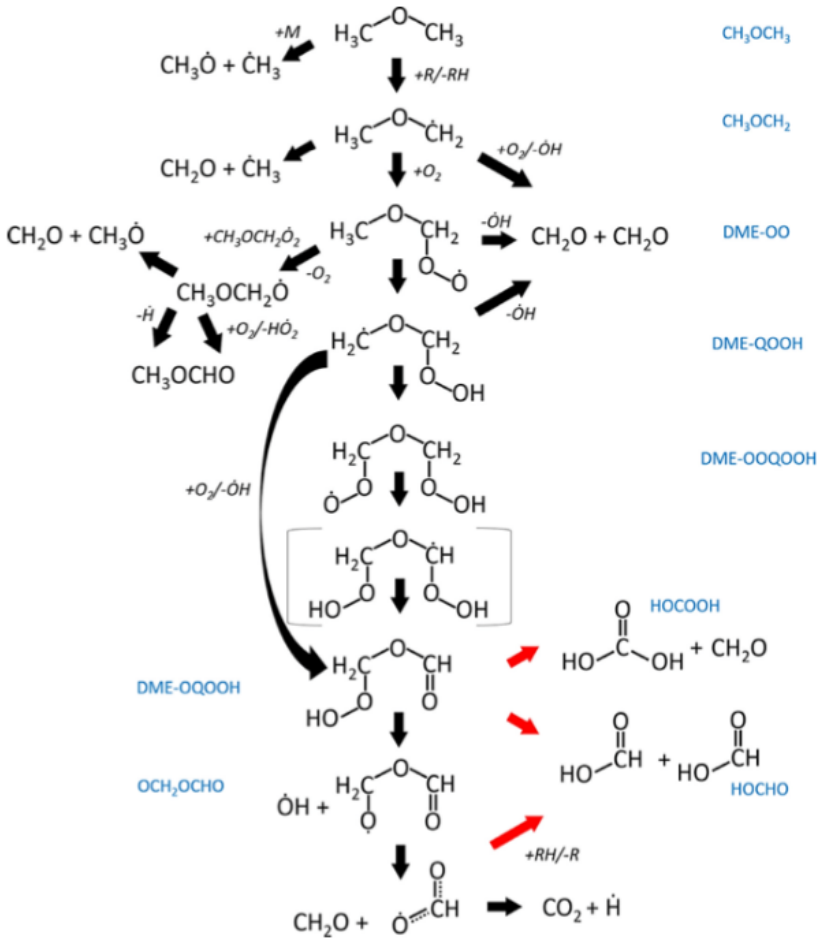

Figure 2.2: DME low-, medium- and high-temperature oxidation pathways. Red arrows highlight routes added to improve the original model [12].

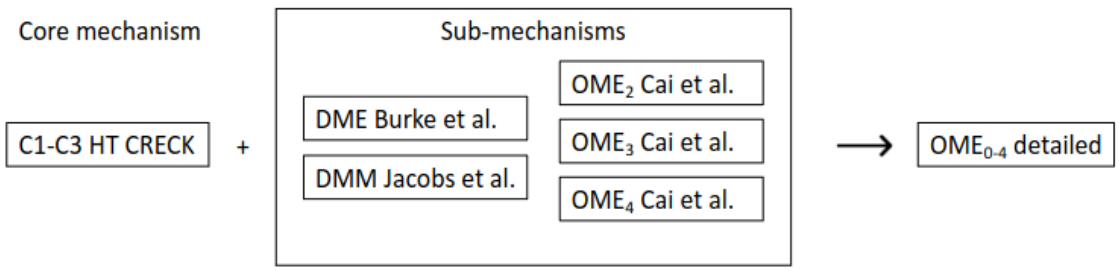

Figure 2.3: The core C_1-C_3 mechanism was supplemented with sub-mechanisms involving DME, DMM, and OMEs in order to form the OME kinetic mechanism structure.

2.2. Gradient-based and gradient-free algorithms

Optimization is the process of finding the best solution to a problem by adjusting the values of the parameters within a set of constraints. There are two main methods for optimization: gradient-based and gradient-free methods. Gradient-based optimization methods rely on the gradient of the error function with respect to the parameters [81–83]. The gradient is a vector that points in the direction of the steepest increase in the error function. The most popular gradient-based optimization method is the gradient descent (GD) algorithm, which updates the parameter vector x at each iteration according to Eq.2.1 [84, 85].

$$x(k+1) = x(k) - \alpha \cdot \nabla E(x(k)) \tag{2.1}$$

where α is the step size or learning rate. This kind of algorithm is widely used not only for its simplicity of application but also for its potential. Because of these main reasons, it is commonly used to minimize a wide range of different error functions.

Gradient-free optimization methods are a class of optimization techniques that do not rely on computing the gradient of the error function. The reason for their name is that they can update the parameters without relying on gradient information, as stated in [86].

Some popular gradient-free optimization methods include:

- Random search: It is a simple method that generates random samples from the parameter space and evaluates the error function at each sample. The method can be used to find a global minimum of the error function, but it is generally less efficient than gradient-based methods [87].
- Simulated Annealing: It is a more sophisticated gradient-free method that is inspired by the annealing process in metallurgy. The method starts with a high "temperature" and gradually decreases it over time. At high temperatures, the algorithm is allowed to make large random changes to the parameters, but as the temperature decreases, the changes become smaller and the algorithm becomes more likely to find a good local minimum [88].
- Evolutionary Algorithms (EAs): are a family of optimization algorithms that are inspired by the process of natural evolution. They are used to find the best solution (or a near-optimal solution) to a given optimization problem. They are particularly useful when the problem is complex and has many local optima or when the problem is non-linear or non-differentiable [89]. EAs typically work by generating a population of potential solutions and iteratively evolving this population over time by

applying genetic operators such as crossover (recombination), mutation and selection. The solutions that are better suited to the problem are more likely to survive and reproduce, while the less suitable solutions are less likely to survive. This process continues until a satisfactory solution is found or a stopping criterion is met. Examples of evolutionary algorithms include: Genetic Algorithm (GA), Differential Evolution (DE), Particle Swarm Optimization (PSO) and Evolutionary Strategy (ES) [90, 91].

When dealing with highly non-convex error functions or when the gradient is challenging to compute or not computable, gradient-free methods can be advantageous. Although they may not be as efficient as gradient-based methods, they have the ability to locate global minima and are capable of handling situations where the gradient is unavailable or difficult to compute.

Each optimization method, whether it be gradient-based or gradient-free, has its own strengths and limitations. Gradient-based methods are often faster and more efficient, but they can become trapped in local minima. On the other hand, gradient-free methods may be slower but can locate global minima in certain scenarios.

The selection of an optimization method should be based on the specific problem at hand and the characteristics of the error function. If the error function has numerous local minima, a gradient-free method may be the better option. Conversely, if the error function is well-behaved and smooth, a gradient-based approach may be more appropriate.

The high non-linearity of the objective function makes it challenging to employ gradient-based algorithms in optimizing a kinetic scheme because of the high non-linearity of each kinetic constant. In this regard, Elliott et al. [69] conducted an extensive investigation into the use of Evolutionary/Genetic Algorithms (EA/GA) for optimization problems involving intricate kinetics. The study found that EA/GA are highly suitable for exploring objective-function spaces with high dimensionality [70]. Based on these findings, GA was chosen as the preferred method for conducting the optimization.

2.2.1. Genetic Algorithms

In the present work, a Genetic Algorithm (GA) is used as gradient-free method with an initial population (S) of 100 solutions. GA is an optimization technique inspired by natural selection and Darwin's theory of evolution. Similar to biological evolution, GA aims to find the optimal solution to a problem by starting with a population of initial solutions and using the principles of natural selection, crossover, and mutation. The GA process begins with the creation of a random population of solutions, called *generation*

0. Each solution is represented as a chromosome, which contains a string of genes that encode the parameters of the problem to be solved. For example, if one is trying to find the optimal solution to a mathematical function, the genes can represent the values of the variables of the function (in this case the kinetic parameters of a rate constant: A, beta and E/R, see Fig. 2.4).

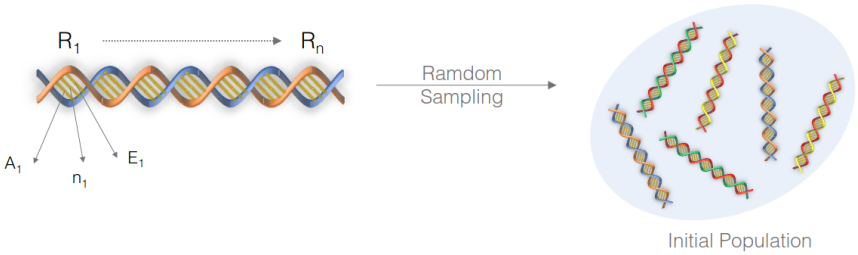

Figure 2.4: Graphical representation of a DNA string in a genetic algorithm applied to chemical kinetics, courtesy of Bertolino A. [11].

GA proceeds through a series of iterative stages. In each iteration, the fitness value of each solution in the population is calculated, which is the measure of how well each solution fits the problem. Two random solutions are selected for reproduction in the genetic algorithm. This is accomplished through the application of the crossover technique, where two DNA strings swap their parameters according to a probability called the *crossover rate* (p_c). The resulting offspring are then inserted into the new population, and they may mutate according to a probability called the *mutation rate* (p_m). After these stages are complete, the resulting population size is twice that of the initial one ($2S$), so a replacement procedure occurs. During this final stage, some of the lower-performing solutions from the previous generation are replaced with the new ones generated in the previous stages. To ensure a balance between global and local search, the replacement procedure selects $S/2$ strings with the highest fitness values from the final population, and the remaining $S/2$ from the top $3S/2$ strings [11]. The values of $p_c = 0.65$ and $p_m = 0.5$ were selected according to Elliot et al. [69]. The process of selection, crossover, and mutation is repeated for a certain number of generations until a satisfactory solution is found or the maximum number of generations is reached, see Figure 2.5.
As pointed out by Elliot et al., one significant advantage of this algorithm is its ability to explore a population of points rather than a single point, which enhances its potential for optimization.

- A population-based approach enables GA to explore a larger solution space and consider a wider range of potential solutions. This makes it more likely that GA will find a global optimum rather than getting stuck in a local optimum.

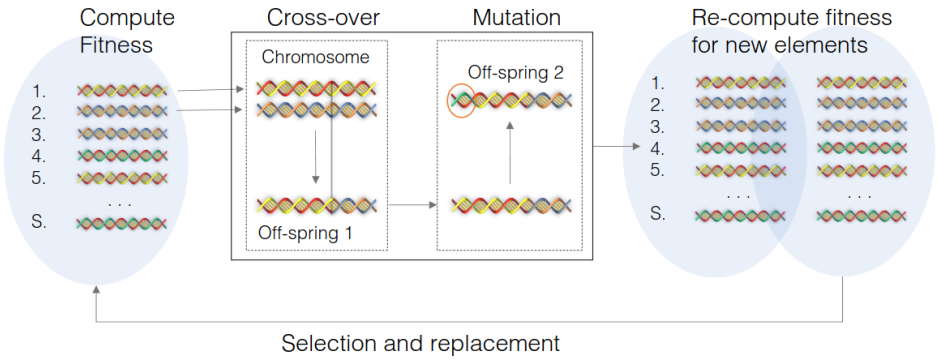

Figure 2.5: Graphical representation of an example generation in Genetic Algorithms, courtesy of Bertolino A. [11].

- GA is less sensitive to initial conditions than gradient-free algorithms that rely on starting from a single point. With GA, the quality of the initial population is less critical since the population will evolve and adapt over time through the use of selection, crossover, and mutation operations.
- The population-based approach of GA allows it to concurrently explore multiple regions of the search space. This enables GA to take advantage of parallel computing resources to further enhance its optimization performance.

2.3. Objective function: the curve matching index

2.3.1. L^2-norm

In every optimization problem, the optimal solution is determined based on the objective function (Obj), which is a measure of how closely the current evaluation (Y_{sim}) matches the experimental targets (Y_{exp}). Several options are available in evaluating this function, one of the most commonly used is the L^2-norm, also known as the Least Squares (LS) method. In this method, the residual between the experimental data (Y_{exp}) and the simulated value (Y_{sim}) is squared for each data point (j) in each data set (i) and then summed to give the objective function. This function is then minimized to find the optimal solution. The L^2-norm is popular because has the desirable property of giving more weight to larger errors, which helps to identify and correct significant discrepancies that is why in the formula the deviation standard is used[15]:

$$Obj = \sum_{i}^{N} \frac{1}{N_i} \sum_{j}^{N_i} \left(\frac{Y_{ij}^{exp} - Y_{ij}^{sim}}{\sigma_{ij}} \right)^2 \tag{2.2}$$

In the above equation, each parameter corresponds to:

- N: total number of data sets;
- N_i: number of data points in data set i;
- $\frac{1}{N_i}$: weights the Obj based on the number of data points in each data set

There are two limitations when comparing simulation results with experimental data using the L^2-norm function, which calculates the sum of squared deviations between the prediction of the model and the experimental data.

1. Although this approach yields significant results and is reliable, robust, and simple, its limitation lies in its inability to consider the shape of the curves, as assessed by Bernardi et al. [13].
2. This method can only be used to compare and rank different models if there is a consistent population of models available for comparison. When dealing with novel fuels for which no suitable model exists in literature, the comparison between the model and experiments must be made in absolute terms rather than relative terms, as pointed out by Pelucchi et al. [76].

2.3.2. CurveMatching Index

A first step toward the solution to both limitations was introduced by Bernardi et al.[13], where the Curve Matching framework was first presented. In this scenario, a multi-index technique has been suggested, which depends on the functional examination of model and experimental values, rather than a distance measure for each point. B-spline interpolation is used to obtain a functional estimation of both the model and experimental values (and their derivatives), and the second derivatives are smoothed by implementing a roughness penalty. A generalized cross-validation approach is applied to the first derivative of the function to assign it the appropriate weight, resulting in a reasonable approximation of both data points and first derivatives [76, 92].

The core of the Curve Matching approach relies on a multifaceted analysis of the dissimilarity between the corresponding functional sets of models and experiments, respectively. To this purpose, four indices, or dissimilarity measures, are evaluated. They were chosen with the purpose of providing a multifaceted, and objective evaluation of the dissimilarity between the two functions. The indices were selected in such a way as to cover the range [0,1], with 0 meaning maximum dissimilarity, and 1 perfect similarity. Let f and g be two curves and f' and g' their first derivatives (obtaining by interpolating smoothed splines),

respectively the functional estimation of the experimental data and model evaluation [93]. Let D be the intersection of the domains of the two functions and let 2.3 be the norm of a curve h in the L^2-space. [70, 76]

$$||h|| = \sqrt{\int_D h(x)^2 dx} \tag{2.3}$$

The dissimilarity indices introduced here are defined as:

$$d^0_{L2}(f,g) = \frac{1}{1 + \dfrac{||f-g||}{|D|}} \in (0,1) \tag{2.4}$$

$$d^1_{L2}(f,g) = \frac{1}{1 + \dfrac{||f'-g'||}{|D|}} \in (0,1) \tag{2.5}$$

$$d^0_p(f,g) = 1 - \frac{1}{2}\left|\left|\frac{f}{||f||} - \frac{g}{||g||}\right|\right| \in (0,1) \tag{2.6}$$

$$d^1_p(f,g) = 1 - \frac{1}{2}\left|\left|\frac{f'}{||f'||} - \frac{g'}{||g'||}\right|\right| \in (0,1) \tag{2.7}$$

Individually, d^0_{L2} depends on the area enclosed by f and g, while d^1_{L2} evaluates the same quantity between their respective derivatives. Hence, the first generalizes a classical L2-norm, while the second extends it. The graphical representation of how the CM works is presented in Figure 2.6. On the other side, the Pearson dissimilarity measures d^0_p and d^1_p indicate perfect matching if f and g and their derivatives, only differ by vertical translation [11]. These last indicators are obtained from the Pearson similarities reported in Equations 2.8 and 2.9.

$$\rho^0_p(f,g) = \frac{\langle f,g\rangle}{||f||||g||} \tag{2.8}$$

$$\rho^1_p(f,g) = \frac{\langle f',g'\rangle}{||f'||||g'||} \tag{2.9}$$

Where the quantity $\langle f,g\rangle$ and $\langle f',g'\rangle$ are evaluated through Eq. 2.10.

$$\langle f,g\rangle = \int_D f(x)g(x)dx \tag{2.10}$$

As ρ_p indicates the cosine of the angle formed by the two functions, it serves as a measure of the correlation between them, reflecting how similar their shapes are [13]. These

similarities are related with d_p^0 and d_p^1 through the Eq. 2.11.

$$d_p = \sqrt{\frac{1-\rho_p}{2}} \tag{2.11}$$

The CM index is a function of the indexes presented in the equations above 2.4, 2.5, 2.6

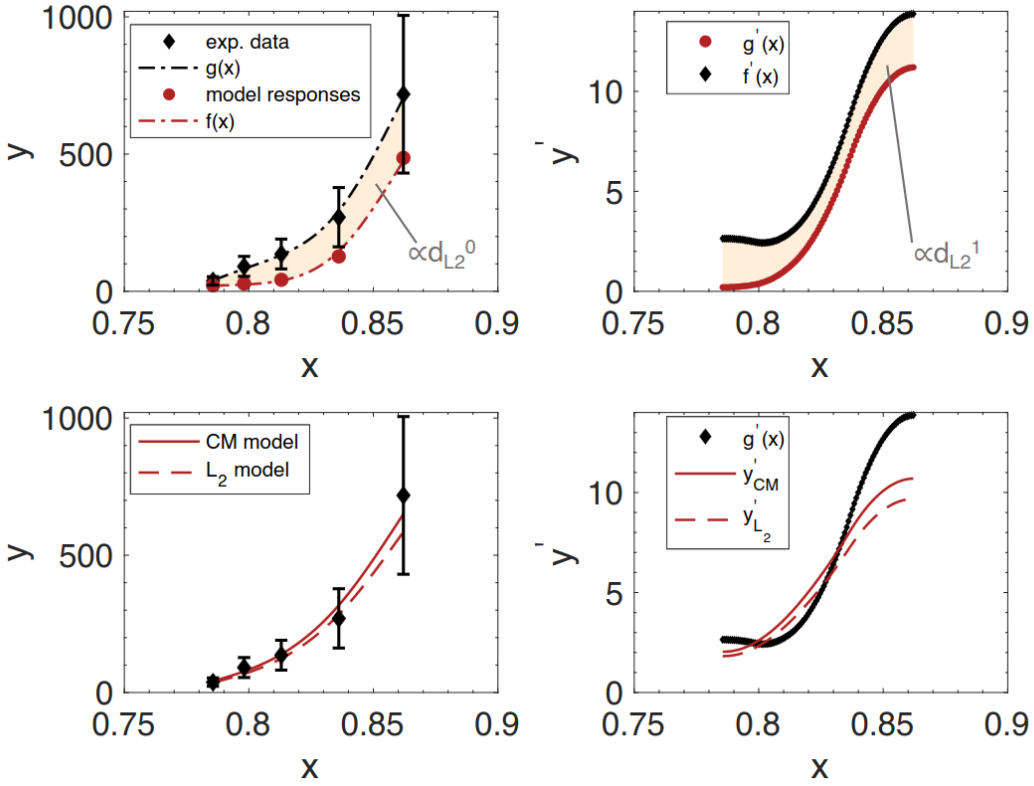

Figure 2.6: Graphical representation of how the splines of f and g and their derivatives are compared in the CM framework. The top figures show the functional estimation of f and g with respect to the data provided (left), and their derivatives (right). The bottom figures present a comparison between an optimization carried out with the CM and the L^2-norm with respect to the experimental data (left) and their derivatives (right). Courtesy of Bertolino A. [11].

and 2.7. Thus the Score of the CurveMatching will be computed as reported in Equation 2.12 and the global objective function assumes the form reported in Equation 2.13.

$$CM_i = \frac{d_{i,L_2}^0 + d_{i,L_2}^1 + d_{i,Pe}^0 + d_{i,Pe}^1}{4} \in (0,1) \tag{2.12}$$

$$Obj = \frac{1}{N}\sum_{i}^{N}(1 - CM_i) \tag{2.13}$$

The CM procedure is explained in Fig.2.7.

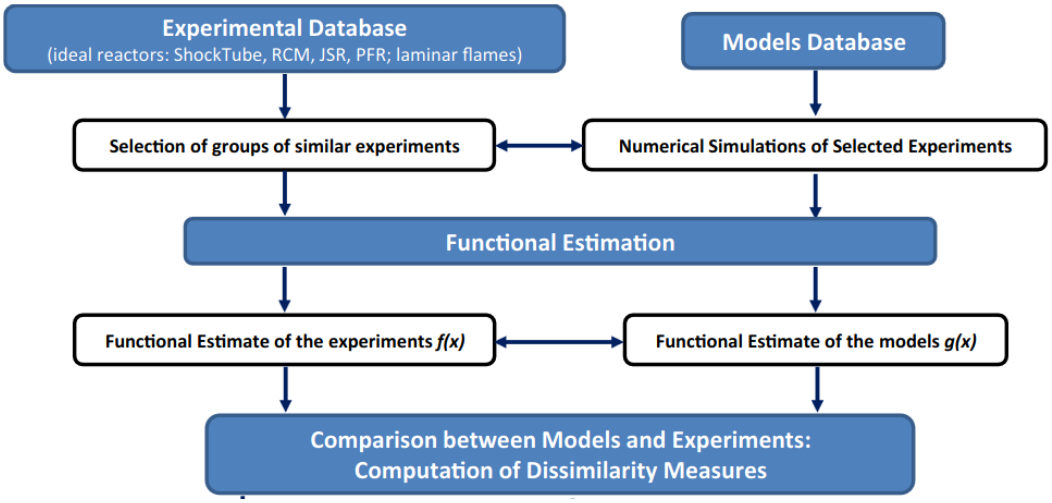

Figure 2.7: Schematic of the CM framework [13].

Bootstrapping and experimental error

As such, the functional curve representing experimental data does not include any information about the experimental uncertainty of the measures. In order to account for the uncertainty in the evaluation of the CM index 2.12, a bootstrapping procedure [94] on the experimental data is carried out. Considering each experimental data point and the related uncertainty, a sufficiently high set of values is randomly generated, assuming that they are normally distributed with an average corresponding to the data point, and a standard deviation equal to the experimental uncertainty. Figure 2.8 displays an example of the application of the bootstrap procedure for laminar flame speed data, where 7 Gaussian distributions (i.e. one for each data point) were sampled 10 times to generate as many bootstrap variations. A set of 50 bootstrap variations (N_b=50) for each data point was adopted after verifying the substantial independence of the final output on a further broadening of the set [11].

Taking into account of this procedure the new objective function becomes as described in Eq. 2.14.

$$Obj = \frac{1}{N}\sum_{i}^{N}\left(1 - \frac{1}{N_b}\sum_{j}^{N_b} CM_{i,j}\right) \tag{2.14}$$

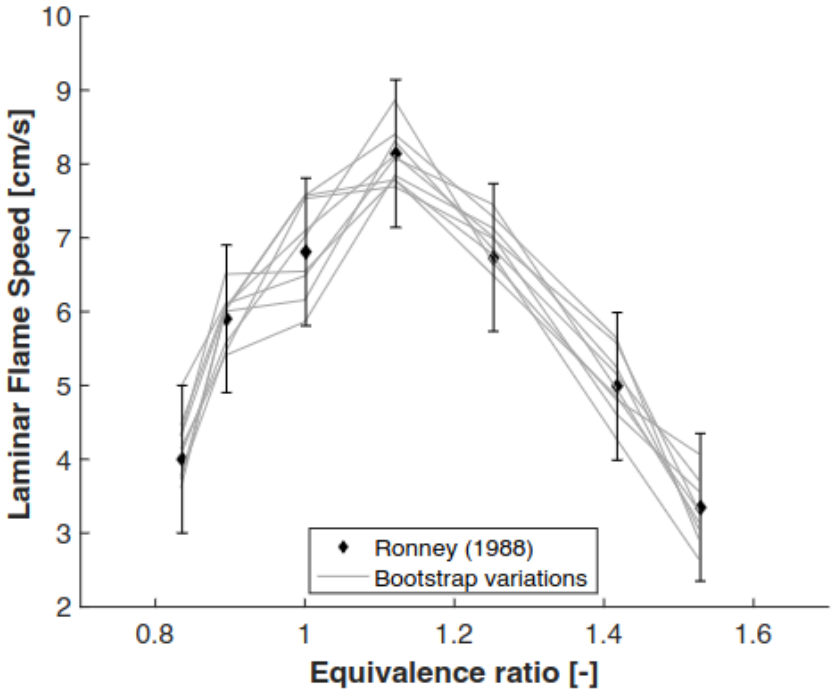

Figure 2.8: Example of bootstrap procedure with 10 variations [11]. Experimental data from [14].

Where N_b in Equation 2.13 is the number of bootstrap variations.

2.4. Scaling factor

The optimization of kinetic mechanisms for combustion models can be a challenging task due to the large number of reactions involved. However, it is well-known that reactions belonging to a specific class often share a common reference parameter. This observation has led to the development of a strategy that optimizes only the three Arrhenius parameters for the reference kinetic and then scales the reaction rate of other reactions in the same class accordingly. This approach leverages the shared characteristics of reactions within a class and allows for more efficient optimization of combustion mechanisms. In order to optimize the reference kinetic parameters the following rules were applied:

$$f^{A}_{scaling} = \frac{ln(A_{opt})}{ln(A_{ref})} \tag{2.15}$$

$$f_{scaling}^{\beta} = \beta_{opt} - \beta_{ref} \tag{2.16}$$

$$f_{scaling}^{\frac{E}{R}} = \left(\frac{E}{R}\right)_{opt} - \left(\frac{E}{R}\right)_{ref} \tag{2.17}$$

The equations above reflect the idea that if there is a relationship between the reference kinetic parameter and the parameter of a reaction belonging to a class of reactions by a factor of two then, once the reference kinetic parameter is optimized, this proportion must remain constant, and this must be valid for all the three Arrhenius parameters.

2.5. Uncertainty factor

When optimizing kinetic parameters for chemical reaction mechanisms, it is important to ensure that the optimized parameters stay within their prescribed uncertainty bounds, so an uncertainty factor (f_r) is assigned to each parameter in the form described in Eq. 2.18.

$$f_r = \frac{k_{max} - k_0}{ln(10)} = \frac{k_0 - k_{max}}{ln(10)} \tag{2.18}$$

Where:

- k_0: is the rate constant of the nominal mechanism;
- k_{max}: is the upper limit of the evaluation (computed as $k_{max} = k_0 \cdot 10^{f}$);
- k_{min}: is the lower limit of the evaluation (computed as $k_{min} = k_0 \cdot 10^{-f}$).

A penalty function can be implemented to increase the objective function value for parameter combinations that violate the uncertainty limits of the rate constants. This ensures that the optimizer finds the optimal combination of parameters that satisfies the constraints. However, penalty functions should not be used with gradient-based optimization approaches, as these algorithms depend on the slope of the objective function, which is disrupted by the penalty function. Non-gradient-based global optimizers are more suitable for constrained optimization problems such as kinetic mechanism optimization when combined with a penalty function.

In the present Thesis, an uncertainty factor f = 0.5 was assumed as a conservative choice. Using a 0.5 uncertainty factor practically means that the corresponding maximum variation of the optimized rate constant with respect to its original value is of about a factor 3. In Fig. 2.9 is shown an example of an optimized rate constant. The k_{opt} falls inside the

uncertainty region for the whole temperature range, respecting the limits imposed by k_{min} and k_{max}. As it is possible to notice the optimized rate constant falls into the admitted region bounded by k_{max} and k_{min}.

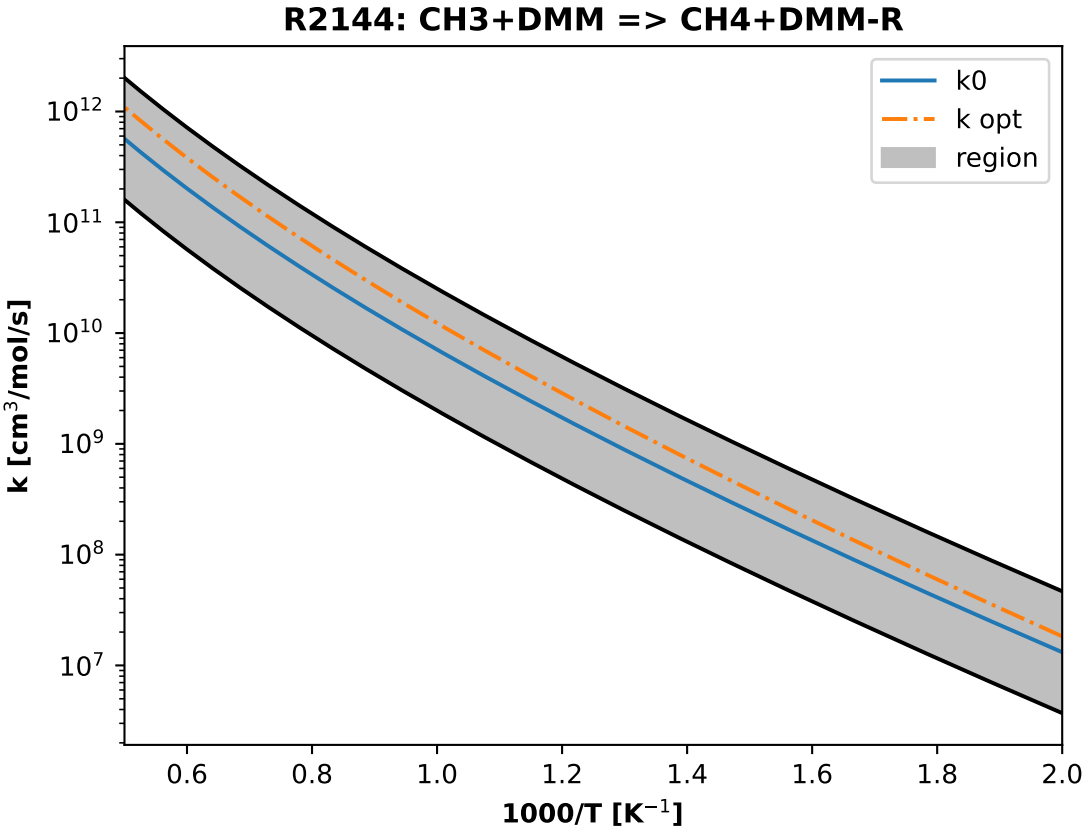

Figure 2.9: Rate coefficient for reaction R2144 of the kinetic mechanism described in 2.1, k_0 is the nominal rate constant, k_{opt} is the optimized one and region is the domain whose upper limit is k_{max} and the lower one k_{min}.

2.6. Sensitivity analysis

Enhancing the accuracy of a model is a crucial task. However, when dealing with large models containing hundreds or thousands of parameters, considering all of them simultaneously can be computationally challenging, even with advanced and efficient tools. Sensitivity analysis provides a means of identifying the relative importance of parameters and enables researchers to focus their efforts on those parameters that have the most significant influence on predictions.

2.6.1. Local Sensitivity Analysis

Reacting gas mixtures are typically simulated using ideal reactors such as perfectly stirred, batch, and plug flow reactors, as well as laminar flames. The behavior of a reacting mixture can be described by a system of coupled, first-order Ordinary Differential Equations (ODE), which can be written as follows:

$$\begin{cases} \dfrac{d\boldsymbol{y}}{d\xi} = \boldsymbol{f}(\boldsymbol{y}, \xi, \boldsymbol{p}) \\ \boldsymbol{y}(\psi_0) = \boldsymbol{y_0} \end{cases} \tag{2.19}$$

The vector of unknowns, denoted by y in Equation 2.19, includes variables such as temperature, pressure, and species concentration. The independent variable, denoted by ξ, represents either time or spatial coordinate, and f(y, ξ, p) is a non-linear function of both the unknowns and kinetic model parameters, p. To calculate the first-order sensitivity coefficients for the i^{th} unknown and the j^{th} parameter, Equation 2.20 is used.

$$s_{ij}^{1} = \frac{\partial y_i}{\partial p_j} \tag{2.20}$$

3 | Workflow

The upcoming chapter outlines the tools employed in this study. Initially, the chapter presents the toolbox `OptiSMOKE++` and `DAKOTA`. Then the sensitivity analysis technique used to identify the crucial reactions in the mechanism and create classes is elaborated. Two test cases are presented, utilizing the substitution method once a reference specie is identified. The chapter emphasizes the most critical aspect of this tool and describes the necessity of scaling factors for each class and how they are calculated. Finally the input method to `OptiSMOKE++` is presented with the optimization targets used in this work.

3.1. Data driven optimization

The tool used in this work to apply the reaction classes optimization is `OptiSMOKE++`[15]. This software is a toolbox developed by A. Bertolino and M. Furst which applies heuristic optimization processes to obtain uncertain kinetic parameters. The software utilizes Data-Driven Optimization, a technique that employs data to facilitate the optimization of a process. In this method, information is obtained from the system or process being optimized and is utilized to make informed decisions about adjusting parameters or settings to enhance performance. This method proves to be particularly beneficial when handling extensive and reliable experimental data sets, such as the database created in `SciExpeM`. In order to work in the chemical region to avoid disturbances by mass transfer, this toolbox can only operate with ideal reactors, such as Batch reactors (adopted to simulate Shock Tubes, STs), Rapid Compression Machines (RCMs), Jet Stirred Reactors (JSRs) and Plug Flow Reactors (PFRs). The entire toolbox is written in `C++` because the numerical simulations are performed in `OpenSMOKE++` [72], entirely developed in `C++` too, while the `DAKOTA` (Design Analysis Kit for Optimization and Terascale Application) [95] toolkit, written in `C++` too, handles the optimization. Dakota is a powerful and flexible open-source software package that is designed to perform optimization, uncertainty quantification and model calibration in a wide range of applications. Some of the key features of Dakota include:

- Support for both gradient-based and gradient-free optimization algorithms, allowing

users to choose the best method for their specific problem.

- An extensible architecture that allows users to easily couple Dakota with their own models and simulation codes, which can be written in any programming language.
- The ability to handle large-scale optimization problems by leveraging parallel and distributed computing resources.
- Support for a wide range of optimization techniques, including local and global optimization methods, and methods for handling nonlinear and nonconvex problems.
- The ability to perform uncertainty quantification and sensitivity analysis, which allows users to understand the effects of input uncertainty on the output of their models.
- it is written in `C++` so there is direct and fast communication between `DAKOTA` and `OpenSMOKE++`.

The selection of `DAKOTA` as the toolkit for handling optimization within the `OptiSMOKE++` suite was influenced by all of these features. Inside the original toolbox proposed by Furst et al., all the parameters of the selected rate constants are expressed according to the modified Arrhenius expression where the logarithmic form is adopted (Equation 3.1).

$$ln(k) = ln(A) + \beta ln(T) - \frac{E_a}{R}\frac{1}{T} \tag{3.1}$$

In order to reduce the computational cost, `OpenSMOKE++` uses the rate constant expressed in Eq. 3.2.

$$k = exp\left(ln(A) + \beta ln(T) - \frac{E_a}{R}\frac{1}{T}\right) \tag{3.2}$$

The parameters undergoing the optimization are: the pre-exponential factor A, the temperature exponent β and the activation energy E_a. They are considered as continuous random variables, usually assumed to be uniformly or normally distributed. Furthermore, during the optimization, they are subjected to non-linear constraints derived from Eq.2.18 (see Section 2.5). In case the parameters proposed by Dakota violate these boundaries, a penalty function is automatically applied and the procedure starts again. Figure 3.1 illustrates the general workflow of the `OptiSMOKE++` framework. Upon reading the input file, the code modifies the kinetic scheme parameters and verifies that they all fall within the specified uncertainty bounds, subject to a non-linear constraint of $k_{min} \leq k \leq k_{max}$. In case any of the parameters are outside the limits, a penalty function is applied, and simulations are skipped to save computational resources. Otherwise, `OpenSMOKE++` con-

ducts the simulations and computes the objective function based on the results obtained. At this stage, DAKOTA proposes a new set of parameters based on the objective function value, and the process repeats until one or more of the stopping criteria are met.

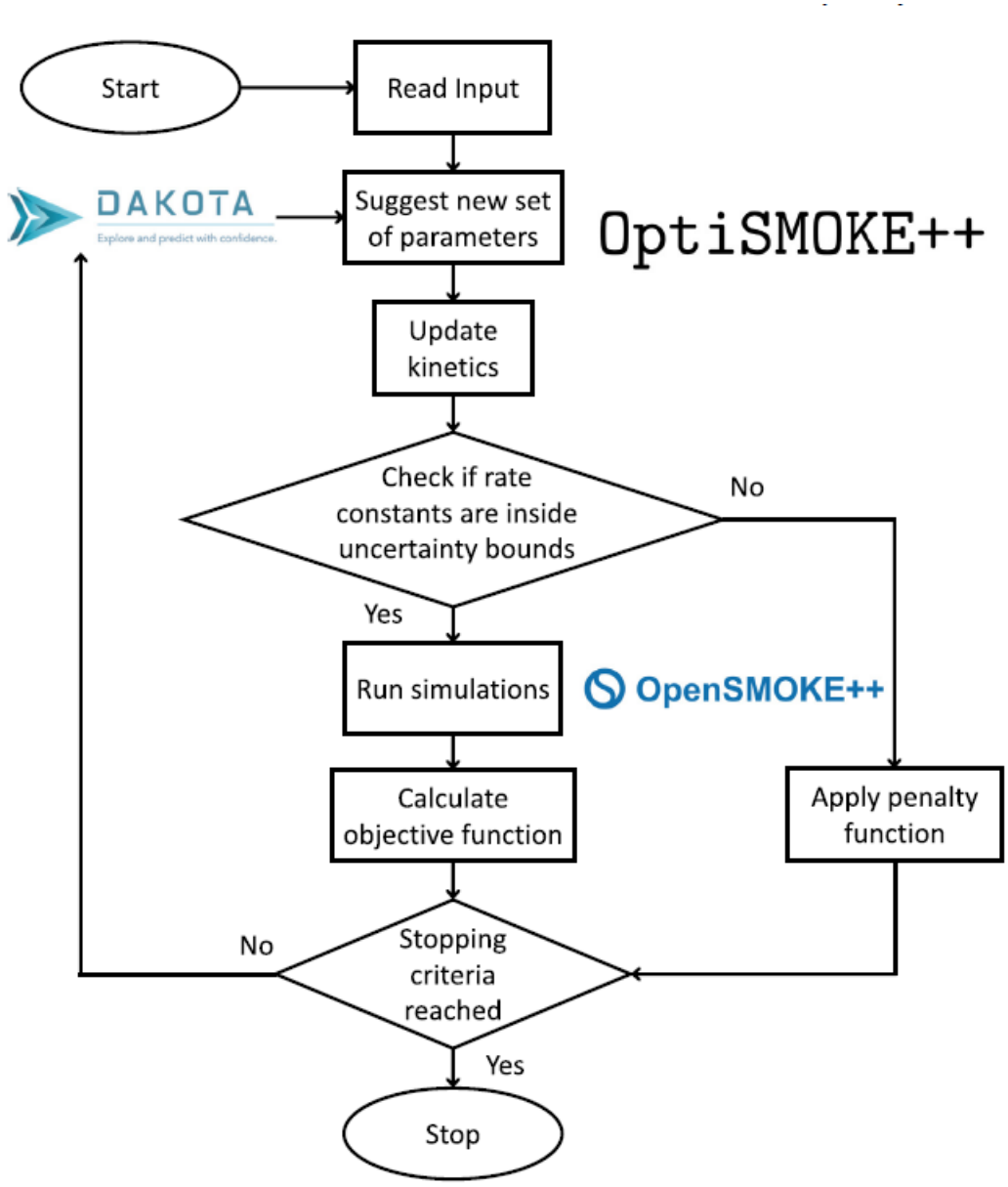

Figure 3.1: OptiSMOKE++ schematic workflow [15]

3.2. Identification of the classes

In order to properly select the reactions which are more important in the kinetic scheme a sensitivity analysis is performed. The sensitivity analysis can be performed either globally or locally, depending on the choice of the user, and can be carried out on a specific species of interest at a specified time. As it will be better explained in detail in Section 3.6.1, the optimization target of this thesis are Ignition Delay Times of $OME_{1\text{-}4}$ so a local sensitivity analysis can be more suitable for this work. To determine the most significant times at which to perform sensitivity analysis, two reference times are chosen: one at which only 1% of the species has been converted, and another at which 99% has been converted. The time interval between these two reference times is then divided into n segments, where n is a user-defined value (n = 3 for this work). The local sensitivity analysis has been performed following the steps below for a given temperature:

1. Calculate the natural logarithmic difference between the times at a certain T.
2. Divide the logarithmic difference by the natural logarithm of the n value to obtain Δt.
3. Create a vector with points spaced Δt apart. The first point in the vector corresponds to the time at which the DMM is 99%, while the last point corresponds to the time at which the DMM is 1% (Fig. 3.3).
4. Perform a sensitivity analysis for each time in the vector. Normalize the sensitivity coefficients relative to the maximum absolute value, and save the coefficients and their indexes in a `.csv` file.
5. Copy all the `.csv` files in a single file.
6. To avoid duplication of indexes, only include the highest absolute value of each index in the summary `.csv` file (Fig. 3.3).

The resulting `.csv` file contains the most sensitive reactions for the cases analyzed and are finally plotted using `PySMOKEPostProcessor` as in Figure 3.2.

The complete list of the sensitivity analysis carried out for DMM ϕ = 1, P = 10 atm, T = 600-1300 K can be found in appendix B. The kinetic mechanism used in this workflow is the one described in Section 2.1, the lumped one. The sensitivity analysis is done by calculating sensitivity coefficients using the `OpenSMOKE++` framework, which requires the kinetic mechanism and a sensitivities file containing sensitivity coefficients and reaction indices in `.XML` format [72]. In this framework a first order sensitivity analysis is carried out according to the equation 2.20 reported in Section 2.6. In this case, the y is the molar

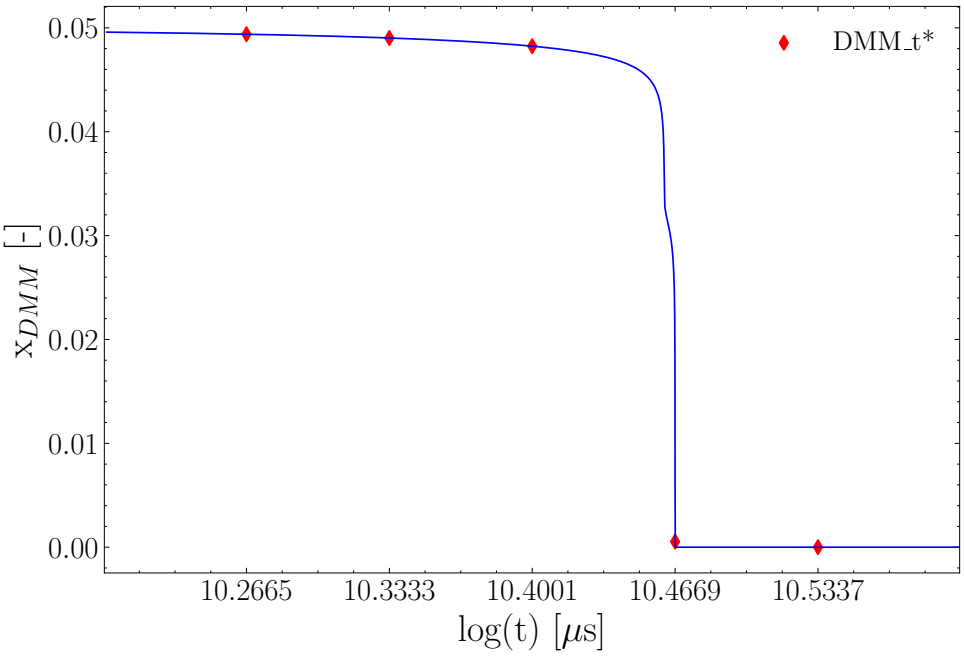

Figure 3.2: Example of times chosen for the local sensitivity analysis for DMM $\phi = 1$, P = 10 atm, T = 600 K (i.e., Case 0).

fraction of the target specie (i.e., DMM) while p is the kinetic constant of one of the n reactions taken for the sensitivity. According to the these results, it is possible to identify several important reactions but only the ones that involve the starting compound (i.e., DMM) at this stage can be taken into account avoiding the radicals. This choice has been made in order to work with species that are not lumped. According to this procedure, the reactions with the higher sensitivity coefficients are summarized in Tab. 3.1 and they are all the H-abstractions of the mechanism involving the starting species.

Reaction Class	Summary
H-abstraction by OH	$OH + OME_n \rightarrow H_2O + OME_n - R$
H-abstraction by H	$H + OME_n \rightarrow H_2 + OME_n - R$
H-abstraction by O	$O + OME_n \rightarrow OH + OME_n - R$
H-abstraction by HO_2	$HO_2 + OME_n \rightarrow H_2O_2 + OME_n - R$
H-abstraction by O_2	$O_2 + OME_n \rightarrow HO_2 + OME_n - R$
H-abstraction by CH_3	$CH_3 + OME_n \rightarrow CH_4 + OME_n - R$
H-abstraction by CH_3O_2	$CH_3O_2 + OME_n \rightarrow CH_3O_2H + OME_n - R$

Table 3.1: Summary of the reaction classes identified.

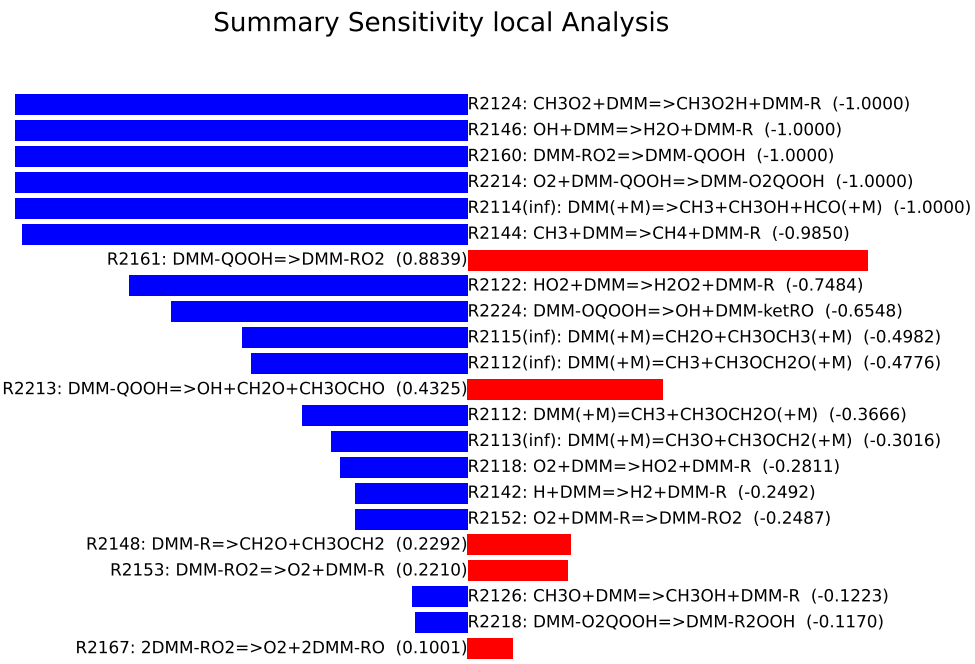

Figure 3.3: Summary of the local sensitivity analysis for DMM $\phi = 1$, P = 10 atm T = 600-1300 K.

3.3. Substitution

The first approach followed after the identification of the classes has been to identify a reference specie and then substitute the kinetic parameters optimized for it in the other compounds. To verify the consistency of the approach, the initial trial involved testing the mechanism developed by Pelucchi et al. [96] on the combustion of linear alcohols, followed by using the mechanism outlined in Section 2.1. The limitations of this approach are highlighted, indicating that some refinements may be necessary in several cases.

3.3.1. Test case 1: Alcohol mechanism

The kinetic mechanism of oxidation of Butanol, Pentanol, and Hexanol was chosen as the most suitable case study since previous research has shown that linear alcohols exhibit intriguing characteristics. Specifically, for the aforementioned compounds, the kinetic constant parameters are nearly identical due to their molecular structure. Pelucchi et al. [96] developed the kinetic mechanism that was optimized by class, and it was later validated. Several deviations between model results and experimental data can be observed in the

work of Pelucchi et al. [96]. For this reason, the opportunity of optimizing the mechanism to increase confidence in its prediction emerged. For this purpose, the `OptiSMOKE++` toolbox was used applying the class-based optimization. The reaction classes identified for this optimization are summarized in Table 3.2, the choice was based on the sensitivity analysis performed on the mechanism. Whereas the experimental targets are JSR mole fraction measurements of different species related to n-butanol, n-pentanol and n-hexanol oxidation taken at different equivalence ratios (0.5, 1.0 and 2.0) and pressures (1 and 10 atm).

Reaction Class	Summary
H-abstraction by HO_2	$HO_2 + C_nH_{2n+1}OH \rightarrow H_2O_2 + C_nH_{2n+1}OH - R$
H-abstraction by CH_3	$CH_3 + C_nH_{2n+1}OH \rightarrow CH_4 + C_nH_{2n+1}OHOH - R$
H-abstraction by OH	$OH + C_nH_{2n+1}OH \rightarrow H_2O + C_nH_{2n+1}OH - R$
H-abstraction by H	$H + C_nH_{2n+1}OH \rightarrow H_2 + C_nH_{2n+1}OH - R$
Beta-scission 1	$C_nH_{2n-1}OH \rightarrow H + C_{n-1}H_{2n-1}CHO$
Beta-scission 2	$C_nH_{2n-1}OH \rightarrow CH_3OCHO + C_{n-2}H_{n+1}$
Dehydration	$C_nH_{2n+1}OH \rightarrow H_2O + C_nH_{2n}$
O_2 addition to α	$O_2 + C_nH_{2n+1}OH - R \rightarrow HO_2 + C_{n-1}H_{2n-1}CHO$

Table 3.2: Summary of the reaction classes used for the alcohols optimization.

The validation data required depends on the focus of the investigation. This includes experimental data from various sources, such as Rosado Reyes et al. [16], Vasu et al. [20], Yujing et al. [17], McGillen et al. [19], and Pang et al. [18], for the kinetic constants, and the molar fraction provided by Jankowska et al. [21]. According to Pelucchi et al. [96] the uncertainty factor has been chosen to be 0.5. Buthanol was utilized as the reference component for each test, with only its kinetic parameters optimized while those of Pentanol and Hexanol were directly substituted. As observed in figures 3.4, 3.5, 3.6, and 3.7, optimization yields better agreement with experimental data despite the imperfections of the initial mechanism. As mentioned before, The mechanism developed by Pelucchi et al. [96] exhibits a strong correlation with the experimental data, as evidenced by figure 3.4a, which shows that the CM index improves from 0.907 to 0.912 after approximately 800 iterations of optimization (for further details on how the CM works see Section 2.3.2).

The substitution method is demonstrated to be a reliable technique in all the cases depicted in Fig. 3.4, Fig. 3.5, Fig. 3.6 and Fig. 3.7 as it exhibits excellent consistency with the experimental data.

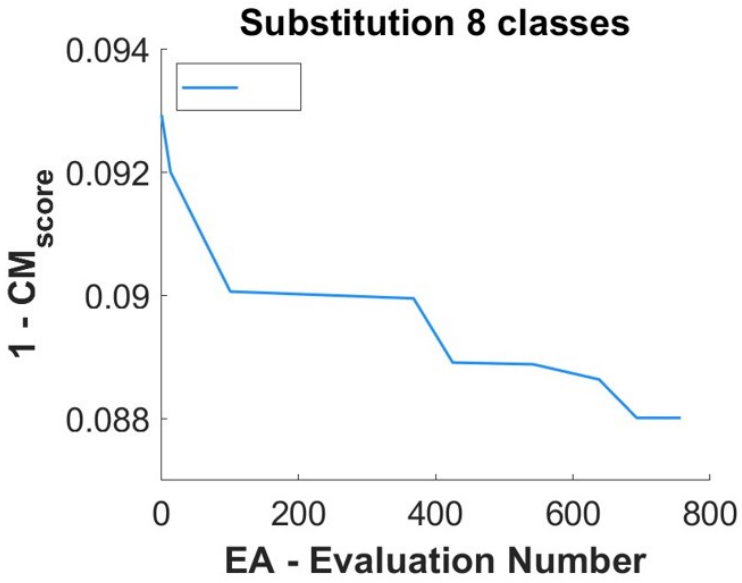

(a) 1 - CM_{score} with the number of iterations.

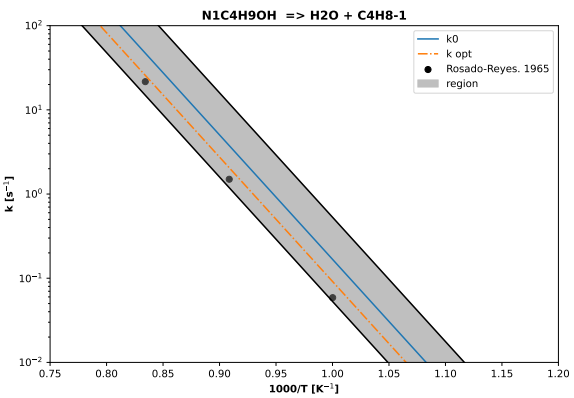

(b) Total rate constant of the dehydration reaction.

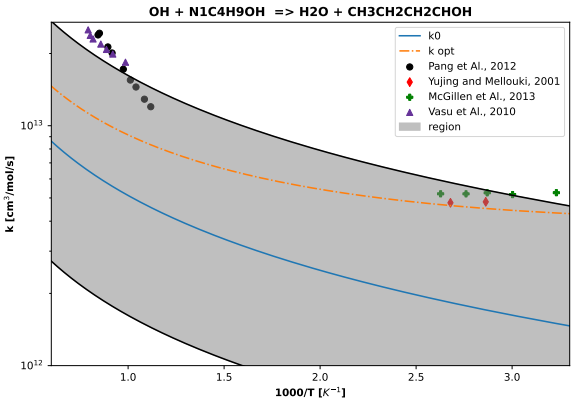

(c) Total rate constant of H-atom abstraction reaction by OH.

Figure 3.4: Number of Iterations of the optimization procedure (Fig. 3.4a). The total rate constant of dehydration reaction from n-butanol [16] (Fig. 3.4b)) and Total rate constant of H-atom abstraction reaction by OH on n-butanol [17–20](Fig. 3.4c) both with the nominal and the optimized models.

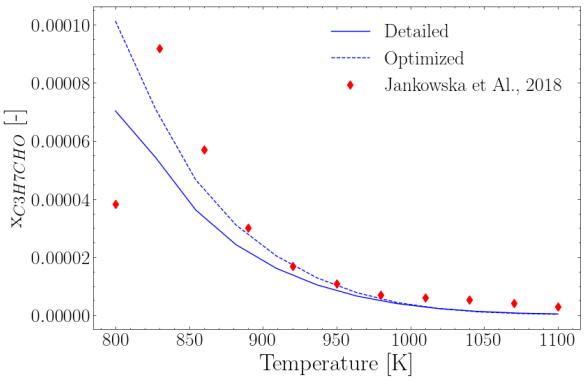

(a) Concentration profile of butanal (C_3H_7CHO) at P = 10 bar and $\phi = 2$.

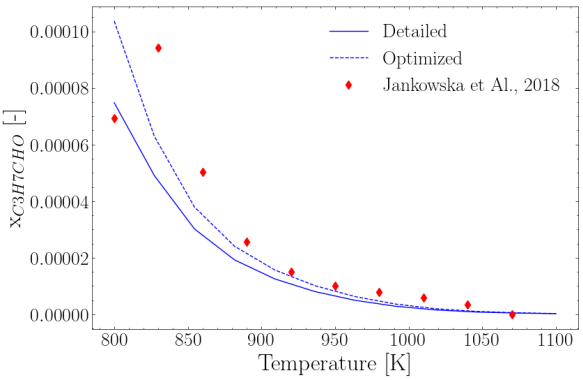

(b) Concentration profile of butanal (C_3H_7CHO) at P = 10 bar and $\phi = 0.5$.

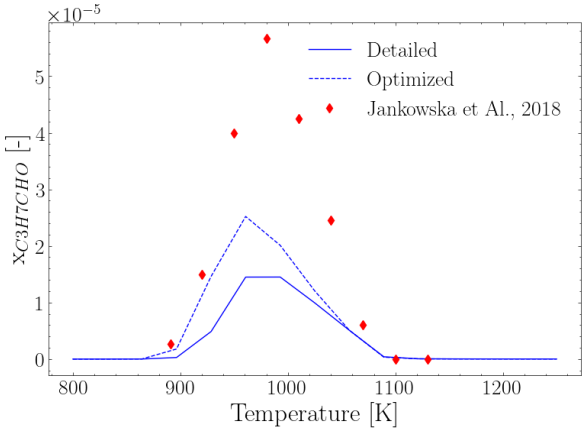

(c) Concentration profile of butanal (C3H7CHO) at P = 1 bar and $\phi = 0.25$.

Figure 3.5: Mole fraction of Butanal (C_3H_7CHO) measured in a JSR by Jankowska et al. et al.[21] for $\phi = 2$ (Fig. 3.5b), $\phi = 0.5$ (Fig. 3.5b) and $\phi = 0.25$ (Fig. 3.5c) and model predictions.

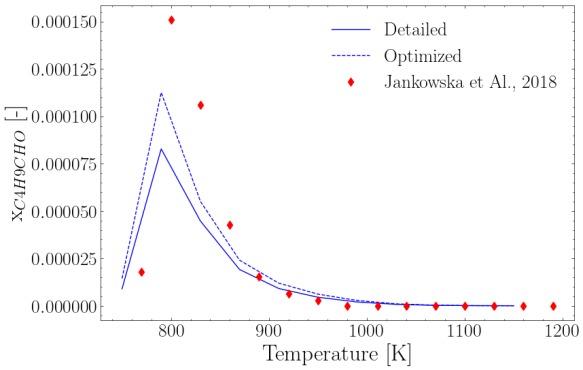

(a) Concentration profile of butanal (C_4H_9CHO) at P = 10 bar and $\phi = 1$.

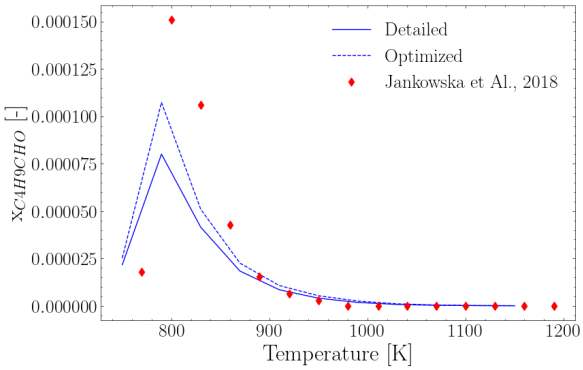

(b) Concentration profile of butanal (C_4H_9CHO) at P = 10 bar and $\phi = 0.5$.

Figure 3.6: Mole fraction of Pentanal (C_3H_7CHO) measured in a JSR by Jankowska et al. et al.[21] for $\phi = 1$ (Fig. 3.6a) and $\phi = 0.5$ (Fig. 3.6b) and model predictions.

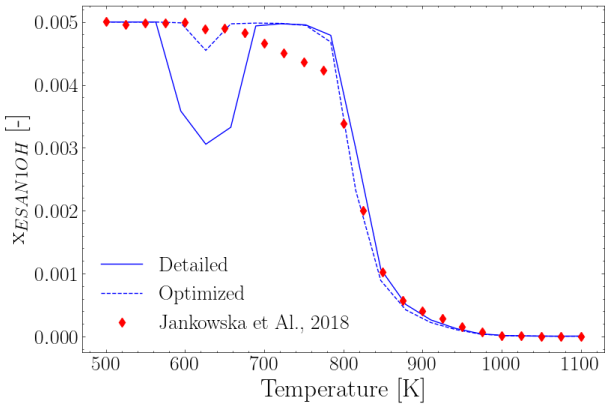

(a) Concentration profile of n-hexanol ($ESAN1OH$) at P = 1 bar and $\phi = 0.5$.

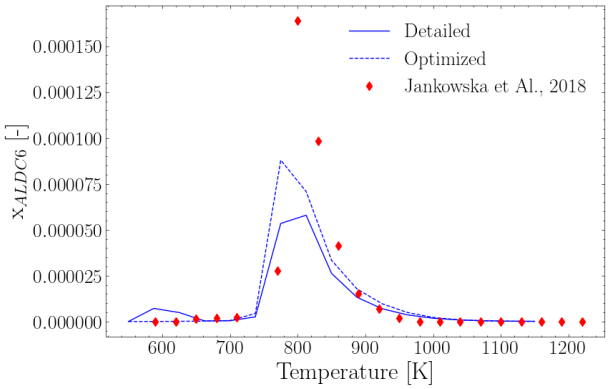

(b) Concentration profile of n-hexanal (ALDC6) P = 10 bar and $\phi = 2$.

Figure 3.7: Mole fraction of n-hexanol ($ESAN1OH$) measured in a JSR by Jankowska et al. et al.[21] for $\phi = 0.5$ (Fig. 3.7a) and Mole fraction of n-hexanal ($ALDC6$) measured in a JSR $\phi = 0.5$ (Fig. 3.7b) and model predictions.

3.3.2. Test case 2: $OME_{1\text{-}4}$

The same substitution procedure has been applied to the kinetic mechanism described in Section 2.1. The classes used for this test sample are the ones summarized in table 3.1. The kinetic constants for $OME_{2\text{-}4}$ are the same as the DMM, which is the reference specie. The optimization of the mechanism has been applied for almost 1500 iterations, Fig. 3.8. For this test case, the optimization targets are the IDTs from the article of Jacobs et al. [22] and the ones of Gillispie [24] for DMM and IDTs from Cai et al.[23] for $OME_{2\text{-}4}$. The findings are summarized in Figures 3.9, 3.10, and 3.11. Due to the focus on demonstrating the potential of the method rather than its performance, only a limited number of validation results are provided in this test case. The optimization procedure generally demonstrates good agreement with the experimental data and the detailed mechanism. However, accuracy is insufficient in most cases. Figure 3.9 highlights some issues with the approach. To improve the level of accuracy between the model and the validation experiments, additional steps must be taken. The fundamental problem with hydrogen abstraction during combustion is that the longer the hydrocarbon chains, the greater the possibility that hydrogen abstraction can occur at different positions, leading to a mixture of products with different structures. The insufficient accuracy between the model and experimental data is due to the fact that this approach does not consider the various possibilities that each species can have based on its molecular structure.

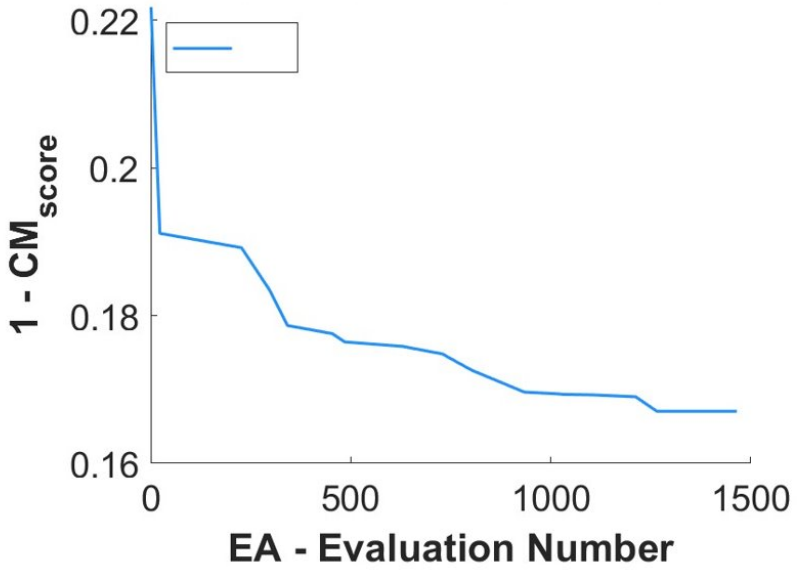

Figure 3.8: 1 - CM_{score} with the number of iterations.

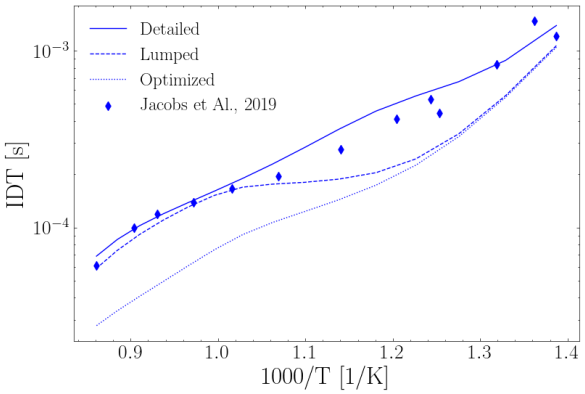

(a) DMM IDT at $\phi = 1$ and P = 40 bar. DMM is diluted in air.

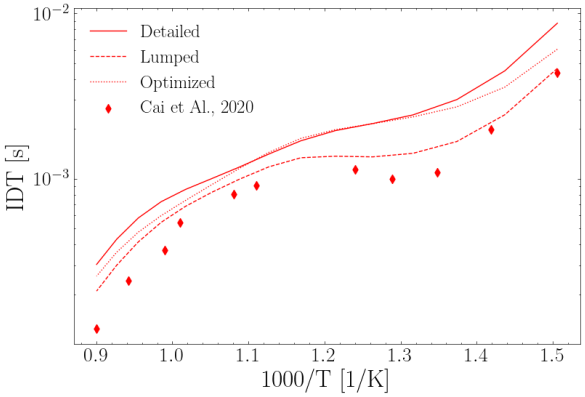

(b) OME_2 IDTs at $\phi = 1$ and P = 10 bar.

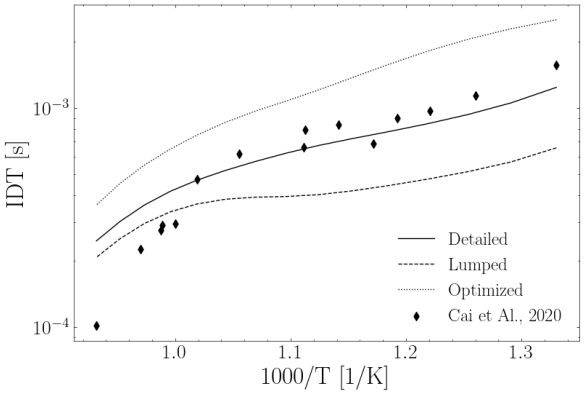

(c) OME_4 IDTs at $\phi = 1$ and P=10 bar [23].

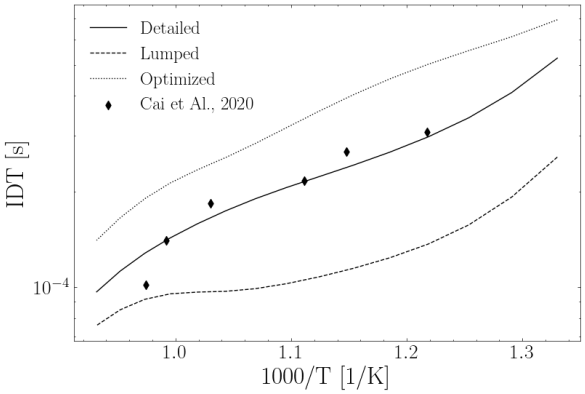

(d) OME_4 IDTs at $\phi = 1$ and P=20 bar [23].

Figure 3.9: DMM IDT measured in a ST by Jacobs et al. [22] 3.9a and $OME_{2\text{-}4}$ IDT measured by Cai et al. [23] 3.9b , 3.9c, 3.9d at $\phi = 1$ and model predictions.

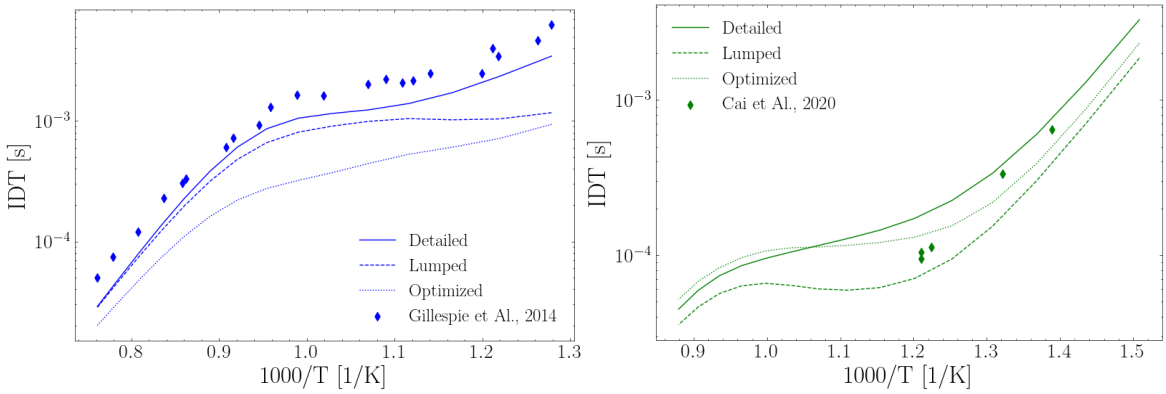

(a) DMM IDT at $\phi = 2$ and P = 9 bar. DMM and O_2 are diluted in 99% Ar.

(b) OME_3 IDT at $\phi = 2$ and P = 20 bar.

Figure 3.10: DMM IDT measured in a ST by Gillespie[24] 3.10a and OME_3 IDT measured by Cai et al. [23] 3.10b at $\phi = 0.5$ and model predictions.

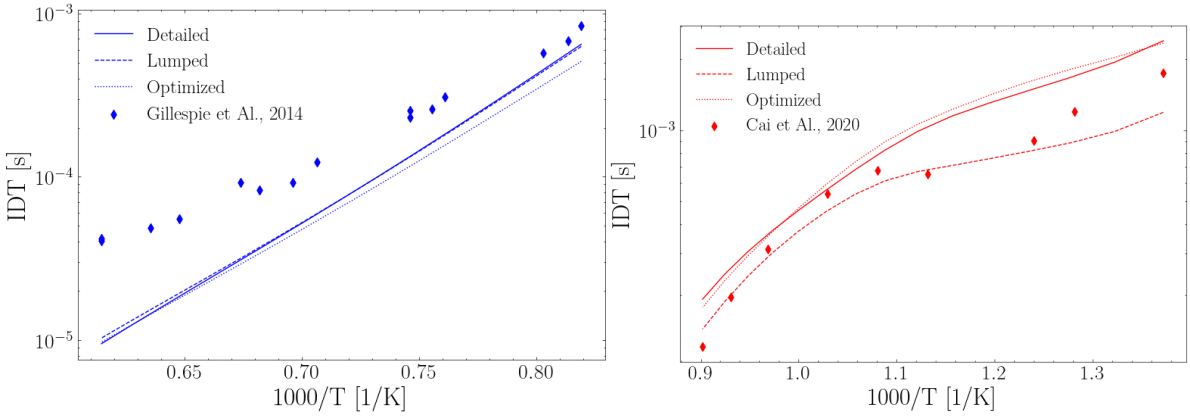

(a) DMM IDT at $\phi = 0.5$ and P = 1 bar. DMM and O_2 are diluted in 99% Ar.

(b) OME_2 IDT at $\phi = 0.5$ and P = 20 bar.

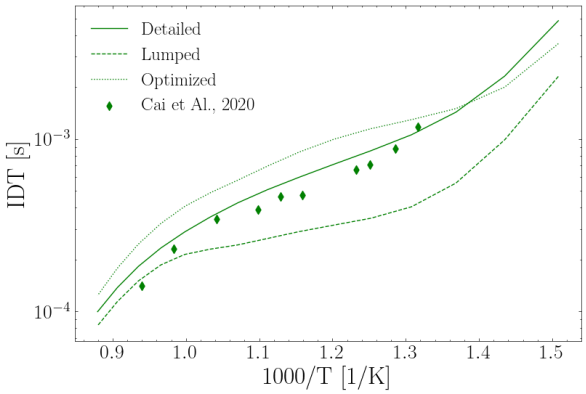

(c) OME_3 IDT at $\phi = 0.5$ and P = 20 bar.

Figure 3.11: DMM IDT measured in a ST by Gillespie[24] 3.11a and $OME_{2\text{-}3}$ IDT measured by Cai et al. [23] 3.11b, 3.11c at $\phi = 2$ and model predictions.

3.4. Kinetic Analysis

In the detailed mechanism, the H abstraction by OH produces different radicals according to the molecular structure of the reactant: the positions are directly related to the number of carbon atoms. This Section provides a concise and detailed examination of DMM, OME_2, OME_3, and OME_4, aiming to emphasize the importance of this information and the underlying causes of the substitution inadequacy of the method. The focus of this investigation is solely on the H-abstraction by OH, as all H-abstractions operate similarly.

3.4.1. DMM

The H abstraction by OH can happen in two different positions for the DMM, Fig. 3.12a and it produces two different radicals according to the reactions 3.3 and 3.4.

$$OH + DMM => H_2O + DMM - RX1 \tag{3.3}$$

$$OH + DMM => H_2O + DMM - RX3 \tag{3.4}$$

Based on the information presented in Figure 3.12b, the radical-producing reaction with a higher kinetic constant is the one that generates RX1, suggesting that RX1 is more likely to be formed compared to RX3.

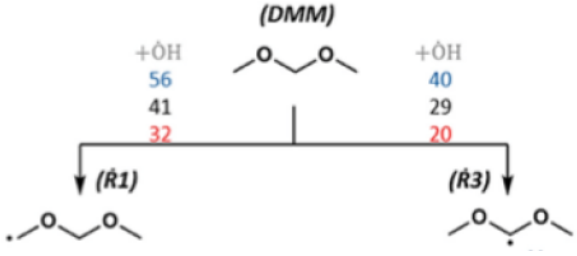

(a) Positions where the H-abstraction is likely to occur for DMM [22].

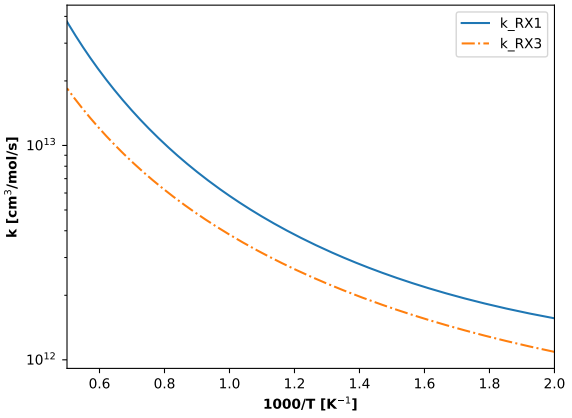

(b) Plot of the kinetic constant for DMM-RX1 and DMM-RX3.

Figure 3.12: Kinetic study for DMM.

3.4.2. OME_2

OME_2 has a symmetrical structure so two positions are available: the ones at the ends and the ones at the centers (Fig. 3.13). Two radicals are formed according to the reactions 3.5, 3.6.

$$OH + OME_2 => H_2O + OME_2 - RX1 \tag{3.5}$$

$$OH + OME_2 => H_2O + OME_2 - RX3 \tag{3.6}$$

As in the case of the DMM, for OME_2 too the radical with the higher kinetic constant, hence the one likely to be produced, is the OME_2-RX3, as reported in Fig. 3.13b.

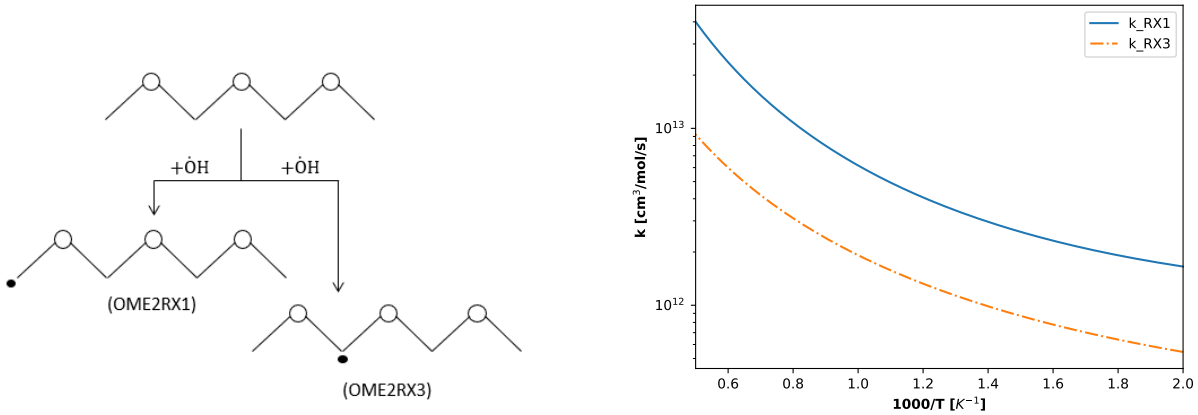

(a) Positions where the H-abstraction is likely to occur for OME_2.

(b) Plot of the kinetic constant for OME_2-RX1 and OME_2-RX3.

Figure 3.13: Kinetic study for OME_2.

3.4.3. OME_3

For the OME_3, three positions are available (Fig. 3.14) in which the H-abstraction by OH is likely to happen:

1. the C atom in the center
2. the two C atoms in the ends
3. the two C in β positions

The 3 radicals are formed according to the reactions listed above (reactions 3.7,3.8,3.9).

$$OH + OME_3 => H2O + OME_3 - RX1 \tag{3.7}$$

$$OH + OME_3 => H2O + OME_3 - RX3 \tag{3.8}$$

$$OH + OME_3 => H2O + OME_3 - RX5 \tag{3.9}$$

For OME_3, the radical that is more likely to be produced is the OME_3-RX1, as it is possible to notice from Fig.3.14b.

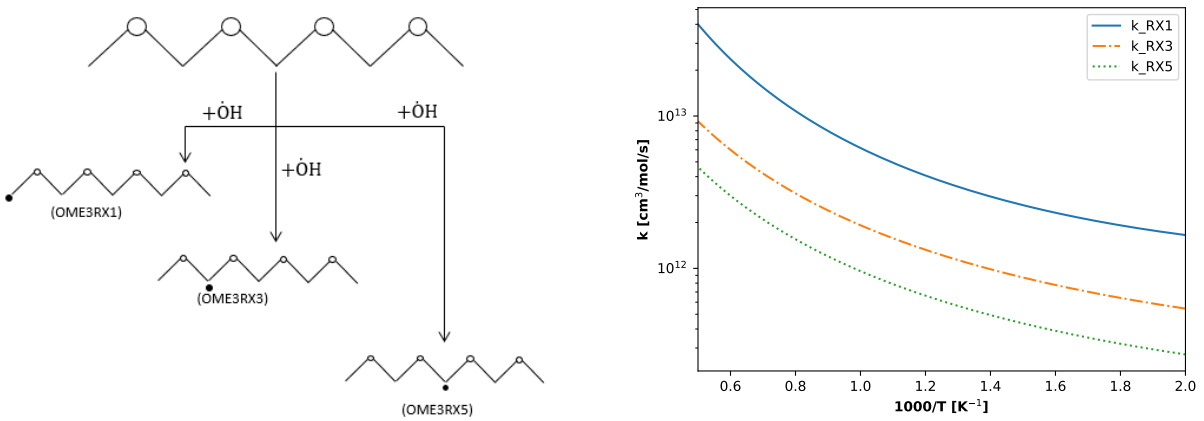

(a) Positions where the H-abstraction is likely to occur for OME_3.

(b) Plot of the kinetic constant for OME_3-RX1, OME_3-RX3 and OME_3-RX5.

Figure 3.14: Kinetic study for OME_3.

3.4.4. OME_4

The OME_4 shows the same positions as OME_3 but in the central position the possibility in which is likely to happen the H-abstraction is double with respect to the one of the OME_3 (Fig.3.15). The reactions involved in the formation of the three radicals are listed below (reactions 3.10,3.11,3.12).

$$OH + OME_4 => H2O + OME_4 - RX1 \tag{3.10}$$

$$OH + OME_4 => H2O + OME_4 - RX3 \tag{3.11}$$

$$OH + OME_4 => H2O + OME_4 - RX5 \tag{3.12}$$

It is worth noting that RX3 and RX5 exhibit the same kinetic constant, which can be attributed to the fact that both radicals involve an H-abstraction from a methylene group. The bond energy of a C-H bond in a methylene group (C bonded to two H atoms) is around

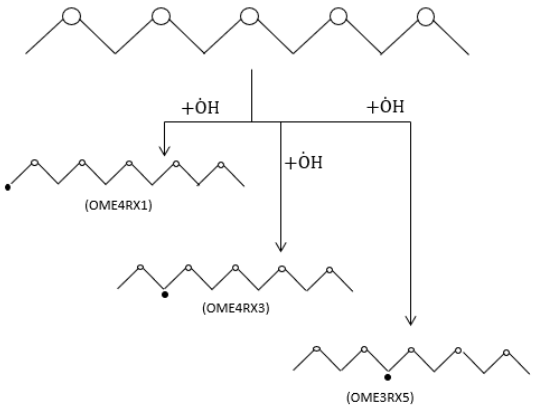

(a) Positions where the H-abstraction is likely to occur for OME_4.

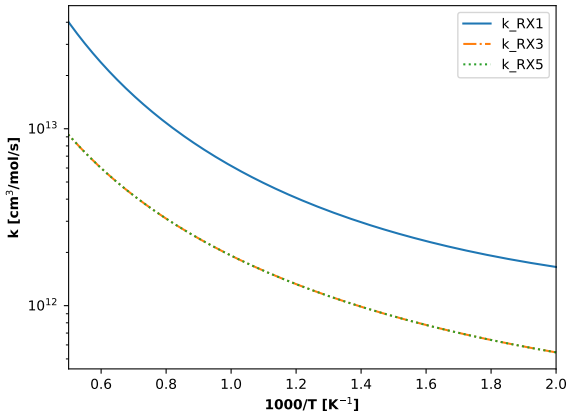

(b) Plot of the kinetic constant for OME_4-RX1, OME_4-RX3 and OME_4-RX5.

Figure 3.15: Kinetic study for OME_4.

435 kJ/mol, while the bond energy of a C-H bond in a methyl group (C bonded to three H atoms) is around 415 kJ/mol. This means that the bond between the carbon atom at the center of the chain (forming RX3 and RX5) and the neighboring hydrogen has a higher bond energy compared to the bond between the carbon atom at the end of the chain (forming RX1) and the neighboring hydrogen. As a result, the radical RX1 is more likely to be formed during the reaction due to the lower energy required to break the C-H bond.

3.4.5. Conclusions

The results of the $OME_{1\text{-}4}$ test sample discussed in Section 3.3.2 and the short kinetic study highlight the potential advantages of employing scaling factors to optimize chemical reactions. Scaling factors, which account for chain length and are derived from the detailed mechanism, can improve the accuracy of predicting reaction rates and product yields, as will be explained in Chapter 4.

However, it is worth noting that the calculation of scaling factors can be computationally intensive, especially for reactions involving radicals as reactants. Advanced techniques such as quantum mechanics or molecular dynamics simulations may be required for such cases.

Despite these challenges, the potential benefits of incorporating scaling factors in the optimization process make it a worthwhile investment. It can lead to a better understanding and prediction of the underlying chemistry behind the oxidation of these compounds.

3.5. Evaluation of the scaling factors

To properly evaluate the scaling factors per each of the three constants a kinetic study has been performed for each of the classes identified in the sensitivity analysis (see Section 3.4) and summarized in Tab.3.1. The methodology exploits for these calculations consists of several steps:

1. Identification of all the radicals formed in the detailed mechanism (as shown per each specie in the reactions reported in Section 3.4).
2. Calculation of the kinetic constant of each radical in the range 500-2000 K.
3. Identification of the so-called k_{tot} per each temperature simply summoning up the kinetic constant of each radical (i.e., horizontal lumping).
4. Extrapolation of the new kinetic parameters of the k_{tot} simply interpolating the k_{tot} obtained per each temperature in the range 500-2000 K.

Following the procedure assessed in Section 2.4, it was possible to find per each class a k_{tot} per each specie and then evaluate the scaling factor of the mechanism. In the tables 3.3, 3.4, 3.5 the scaling factor for the classes chosen are reported for each of the three variables.

Reaction Class	OME_2	OME_3	OME_4
H-abstraction by OH	0.35	0.60	0.96
H-abstraction by H	1.11	3.24	6.52
H-abstraction by O	1.28	1.62	1.96
H-abstraction by HO_2	12.9	26.2	42.1
H-abstraction by O_2	163.0	294.0	432.0
H-abstraction by CH_3	25.6	65.1	117.0
H-abstraction by CH_3O_2	0.57	0.67	0.82

Table 3.3: Summary of the scaling factor for A of each reaction class used within the optimization.

Reaction Class	OME_2	OME_3	OME_4
H-abstraction by OH	0.12	0.06	0.01
H-abstraction by H	-0.13	-0.23	-0.29
H-abstraction by O	0.04	0.05	0.06
H-abstraction by HO_2	-0.11	-0.16	-0.19
H-abstraction by O_2	-0.43	-0.45	-0.46
H-abstraction by CH_3	-0.18	-0.26	-0.30
H-abstraction by CH_3O_2	0.13	0.11	0.09

Table 3.4: Summary of the scaling factor for beta of each reaction class used within the optimization.

Reaction Class	OME_2	OME_3	OME_4
H-abstraction by OH	-142.6	-71.6	-12.7
H-abstraction by H	74.7	147.0	195.0
H-abstraction by O	-92.4	-130.0	-151.0
H-abstraction by HO_2	-37.0	-36.0	-30.0
H-abstraction by O_2	408.0	436.0	450.0
H-abstraction by CH_3	146.0	216.0	257.0
H-abstraction by CH_3O_2	349.0	225.0	145.0

Table 3.5: Summary of the scaling factor for E/R of each reaction class used within the optimization.

3.6. Numerical Optimization

The optimization procedure is divided into different steps:

1. identification of the optimization target: this step involves identifying the specific goal that the optimization procedure aims to achieve.
2. Simulation of the cases: once the optimization target has been identified, the next step is to select the cases that will be used for optimization.
3. Creation of the `.txt` file: after the cases have been selected, the next step is to create a `.txt` file that contains the necessary information for the optimization process.
4. Starting of the optimization: once the `.txt` file has been created, the optimization process can begin. This typically involves running the optimization algorithm that iteratively searches the parameter space to find the optimal solution. During the optimization process, the algorithm evaluates each case using the information provided in the `.txt` file.
5. Construction of the final mechanism: once the objective function reaches a plateau the procedure can be stopped and `OptiSMOKE++` merges the optimized reactions with the starting mechanism

3.6.1. Optimization Target

The whole database of experimental results for $OME_{1–4}$ is reported in Chapter 3, and consists of 56 datasets divided into:

- IDTs in Batch Reactors;
- speciations in JSRs and PFRs;
- LFSs in premixed laminar flames.

A selection process was performed to divide the datasets into optimization and validation targets. Among the DMM experiments, IDTs, taken from Jacobs et al. [22] and Gillespie [24], are the selected optimization targets, covering a wide range of temperatures (T $\simeq$ 700–1800 K), pressure (P = 1 - 40 bar) and composition (ϕ = 0.5 - 2). $OME_{2–4}$ sub-mechanisms were optimized on all the IDT experiments by Cai et al. ([23]), performed at T $\simeq$ 600–1100 K, P = 10–20 bar and ϕ = 0.5–2. Figure 3.16 summarizes all the data points from 9 datasets chosen as optimization targets, represented in a temperature, pressure and equivalence ratio space. The whole range of experimental conditions was largely covered for the optimizations.

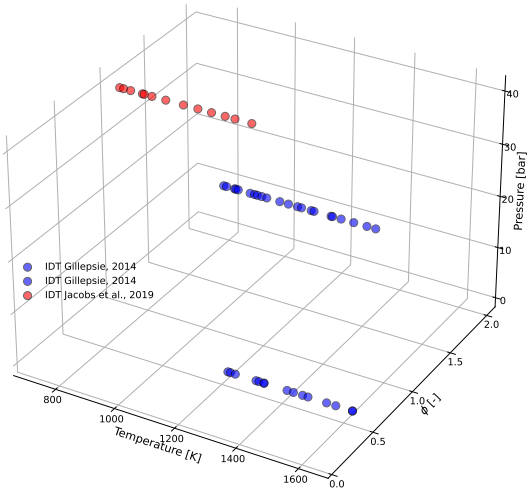

(a) DMM Optimization database.

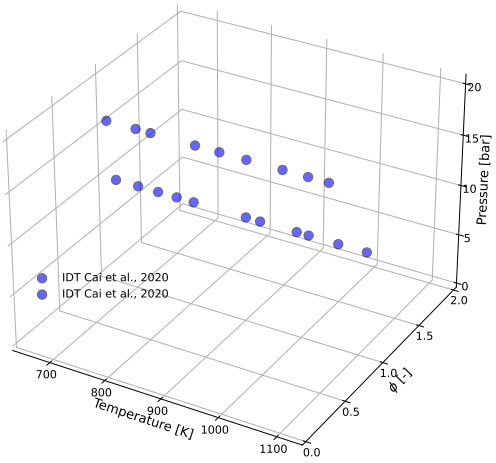

(b) OME_2 Optimization database.

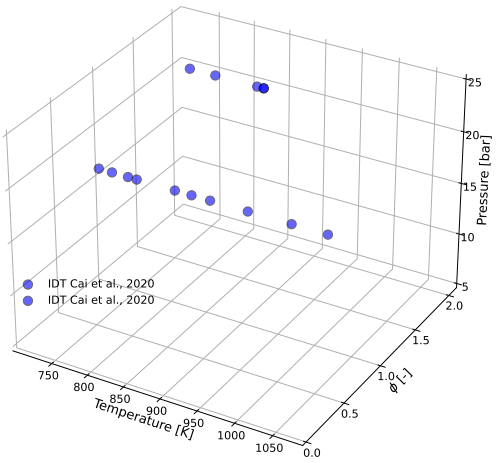

(c) OME_3 Optimization database.

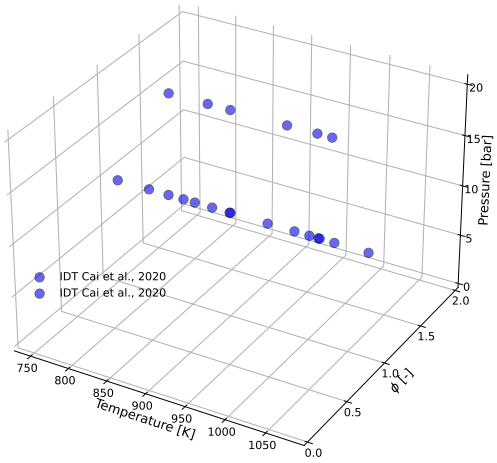

(d) OME_4 Optimization database.

Figure 3.16: Experimental data on $OME_{1\text{-}4}$ adopted as optimization targets, in terms of Temperature, Pressure and Equivalence ratio.

3.6.2. Reaction classes input

In order to submit to `OptiSMOKE++` the class organization, a function has been inserted inside the environment of the toolbox able to read the reactions that belong to a specific class and all the parameters (i.e., uncertainties, scaling factors, etc ...). As it is possible to notice from the above list, some very interesting features have been added to `OptiSMOKE++`. The `.txt` file allows to deeply customize our optimization, meaning that we can select the parameter to be optimized for each reaction belonging to the class and also to not optimize the reaction itself. It also allows running a specific case of optimization: the substitution.

The `.txt` file structure is reported in Alg.3.1.

Algorithm 3.1 `OptiSMOKE++` Reaction Classes Input

1: Name of the class
2: List of reactions belonging to the class
3: Uncertainty factors
4: Target of optimization
5: Scaling factor for lnA
6: 1 or 0 to select the reaction to optimize for lnA
7: Scaling factor of $beta$
8: 1 or 0 to select the reaction to optimize for $beta$
9: Scaling factor of E/R
10: 1 or 0 to select the reaction to optimize for E/R

4 | Validation and results

In this chapter, the results obtained from the optimization per class are presented for the four species and validated against a wide range of experimental values. For each species, the results are divided according to the fuel and the simulation type. In all the subsections the results are organized in plots where the detailed, the lumped and the optimized model are plotted within the experimental results obtained by different authors. All simulations are carried out with `OpenSMOKE++`[72]. IDTs measure in STs have been simulated in Batch Reactors, using the same definition adopted in the corresponding paper. The match between such amount of experiments and models is validation. Typically, this evaluation is done manually, where experimental data and model outcomes are graphed together, and it is left to the discretion of the scientist to determine if the model is acceptable based on the degree of agreement observed. This traditional approach has been employed since the inception of science, but it is subjective and relies on the expertise of the scientist and the specific experiments being conducted. As a result, the same comparison can be deemed acceptable by some, excellent by others, and inadequate by others [76]. So that at the end of each section, a summary table comparing the CM index of each simulation is given in order to try to quantify how "well" or not the new proposed model behaves with respect to the lumped and detailed one.

4.1. DMM

The DMM experimental database is extensive, encompassing a variety of operational parameters, and depicted in Figure 4.1. It comprises 30 datasets, which include IDTs in STs [22, 24–26], LFSs [24], specieations in PFRs by Marrodan et al. [27] and in JSRs by Vermeire et al. [28]. Out of these 3 experimental datasets were identified as optimization targets (as reported in Section 3.6.1), while the remaining 27 were used for performance validation. Further validations are available in Appendix **??**.

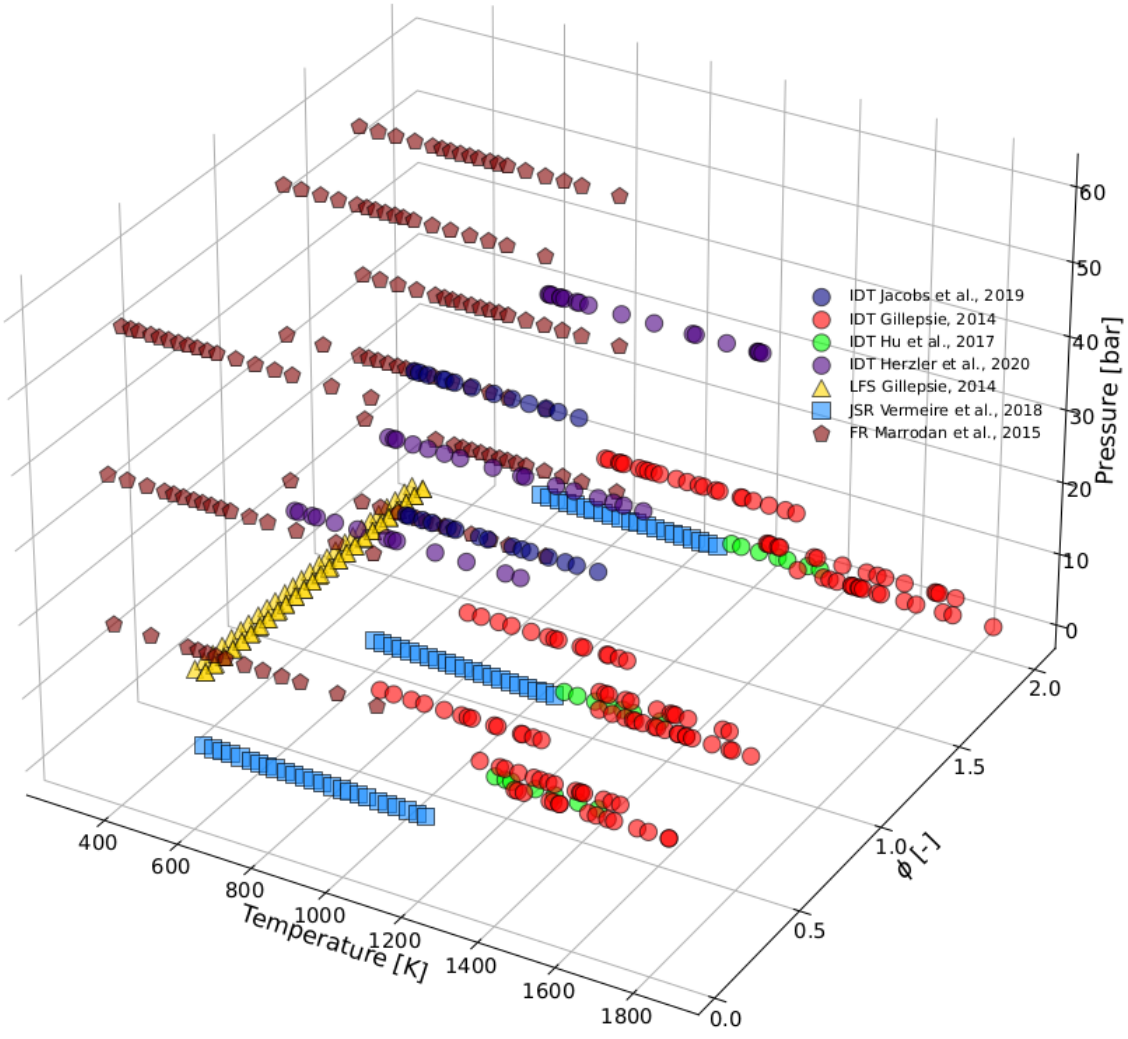

Figure 4.1: Database of experimental values for DMM.

4.1.1. Ignition Delay Times

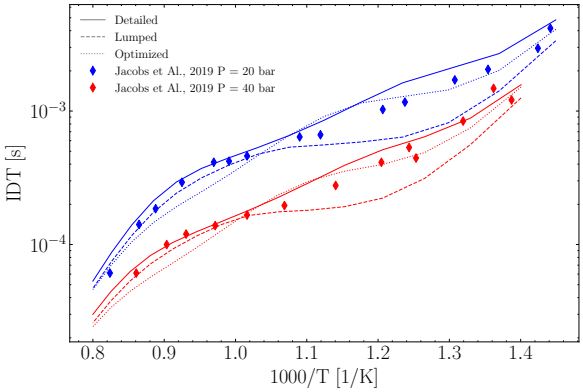

(a) IDTs of DMM/Air at $P = 20-40bar$ and $\phi = 1$.

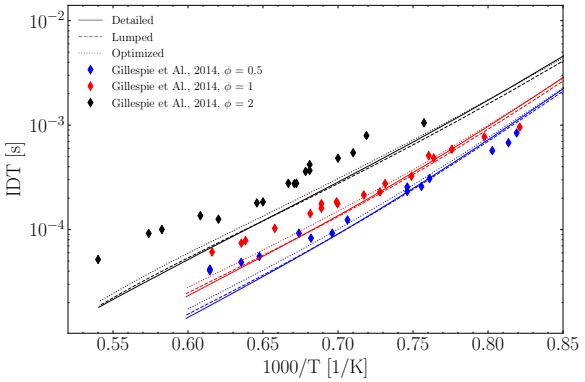

(b) IDTs of DMM/O_2 at $P = 1bar$ and $\phi = 0.5-2$. The mixture is diluted in 99% Ar.

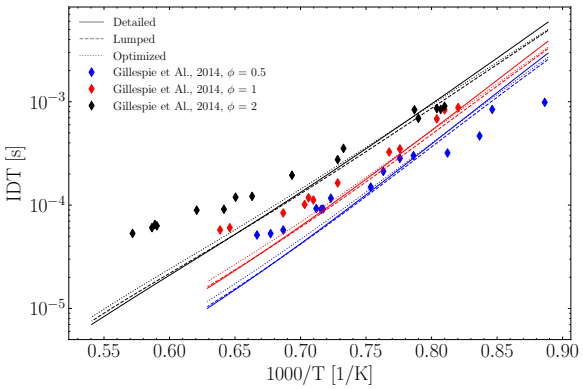

(c) IDTs of DMM/O_2 at $P = 3.5bar$ and $\phi = 0.5-2$. The mixture is diluted in 99% Ar.

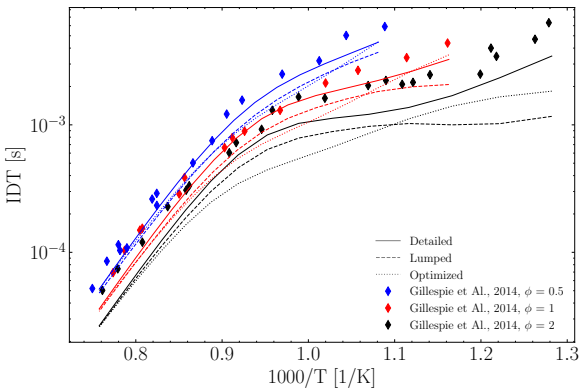

(d) IDTs of DMM/O_2 at $P = 9bar$ and $\phi = 0.5-2$. The mixture is diluted in 99% Ar.

Figure 4.2: IDTs of DMM measured in a ST by Jacobs et al. [22] 4.2a and Gillespie [24] Fig. 4.2b, Fig. 4.2c and Fig. 4.2d, compared with the detailed mechanism (solid line), the lumped one (dashed line) and the optimized too (dotted line).

IDTs experiments at medium and high temperature combustion (T $\simeq$ 750 - 1800 K) were gathered by Gillespie [24] across a range of equivalence ratios (ϕ = 0.5 - 2) and pressures (P $\simeq$ 1 - 9 bar). Meanwhile, Jacobs et al. [22] conducted experiments at ϕ = 1, lower temperatures (T $\simeq$ 700 - 1200 K), and higher pressures (P = 20 - 40 bar).

Figure 4.2a clearly shows that the optimized model outperforms both the Detailed and Lumped models at medium-low temperatures. This outcome was expected because in a combustion process the higher the temperature the lower is the structure of the molecules that are crucially involved. Even if the experimental values at P = 40bar was not used as optimization target, this trend is confirmed in the case of lower pressure (i.e., P = 20 bar) too.

Additionally, to demonstrate the effectiveness of the presented procedure, Figure 4.2b, Figure 4.2c, and Figure 4.2c display three different DMM datasets measured at distinct equivalence ratios. Despite using only P = 1 bar at $\phi = 0.5$ and P = 9 bar at $\phi = 2$ as optimization targets, the model still reasonably reproduces the trends and exhibits good performance with some exceptions.

Based on low-pressure results of Gillespie (Figures 4.2b and 4.2c), it seems that high-temperature reactivity is overestimated, particularly for rich conditions. This phenomenon is observed in all three mechanisms, as the lumping process and the optimization one primarily affect low-temperature kinetics. Similarly, the NTC (Negative Temperature Coefficient) region at P = 9 bar (Figure 4.2d) shows excessive reactivity, but the error is amplified in the lumped mechanism and not recovered by the optimized process. Figure 4.2c is noteworthy because, despite not utilizing any of the experimental data as targets for optimization, the optimized model exhibits excellent agreement with the experimental data.

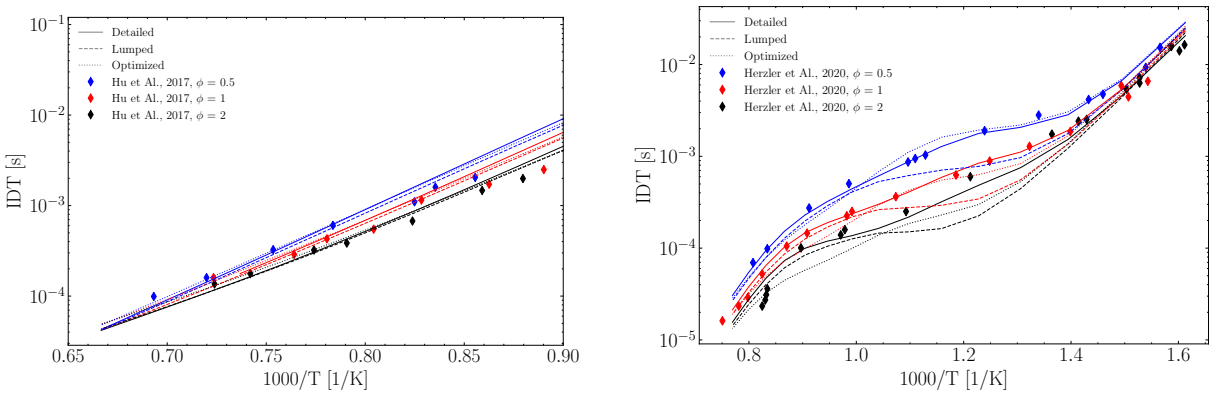

(a) IDTs of DMM/O_2 at $P = 2atm$ and $\phi = 0.5$–2. The mixture is diluted in about 95% Ar.

(b) IDTs of DMM/Air at $P = 30bar$ and $\phi = 0.5$–2.

Figure 4.3: DMM IDTs measured in a ST by Hu et al. [25] Fig. 4.3a and Herzler et al. [26] Fig. 4.3b, compared with the detailed mechanism (solid line), the lumped one (dashed line) and the optimized too (dotted line).

The results of the ST experiments conducted by Hu et al. [25] and Herzler et al. [26] are depicted in Figure 4.3. Hu et al. conducted their experiments at a temperature range of approximately 1100-1400 K and a pressure of 2 atm, while Herzler et al. conducted theirs at a temperature range of approximately 600-1400 K and a pressure of 30 bar. Both sets of experiments investigated the effects of different fuel-to-air ratios ($\phi = 0.5$, $\phi = 1$ and $\phi = 2$).

As stated previously, Figure 4.3a indicates that the optimization process does not have

a deep impact at high-temperature reactivity, and accurate predictions of the original model are maintained in the other two. The NTC behavior in Figure 4.3b is enhanced in the lumped chemistry, and recovers after optimization, still the high- and medium-temperature range is not perfectly matched especially in lean conditions ($\phi = 0.5$). Although neither dataset was used as the optimization target, both were employed solely for validation purposes and it is worth noting that the experimental data show remarkable consistency with the results obtained.

4.1.2. Laminar Flame Speeds

Among the all datasets presented in Figure 4.1, Gillespie [24] has only conducted LFS measurements for DMM at P = 1 atm, at three distinct temperatures (298 K, 328 K, and 358 K), covering a range of equivalence ratios from $\phi = 0.6$ to 1.8.

The detailed mechanism yields results that are in agreement with the experiments, with only a minor overestimation that increases with temperature and occurs at the maximum velocity (i.e., $\phi \simeq 1.2$). Since DMM LFS is solely governed by C_1-C_3 reactions, the lumping process does not affect the behavior of the model and the optimization partially recovers the error introduced by this operation.

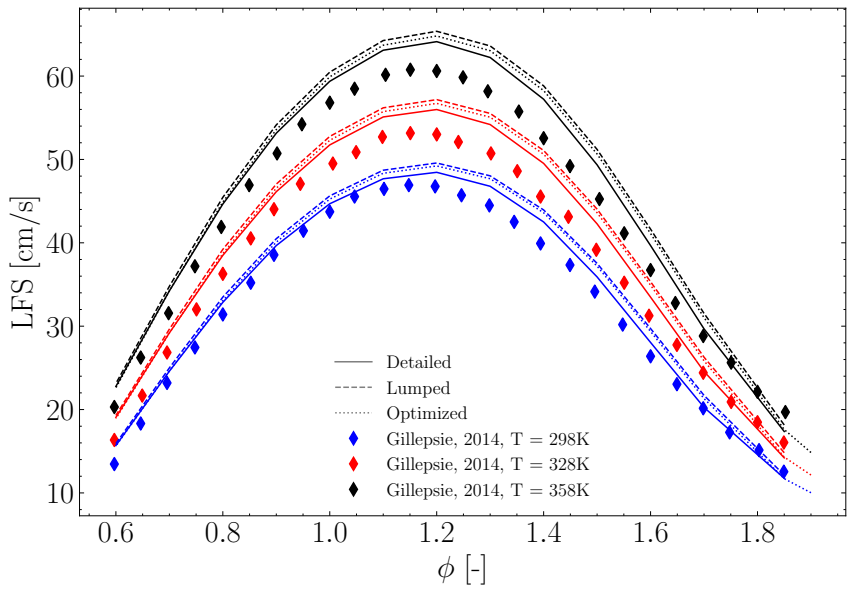

Figure 4.4: DMM LFSs measured by Gillespie [24], compared with the detailed mechanism (solid line), the lumped one (dashed line) and the optimized too (dotted line). Experiments are carried out at atmospheric pressure and T = 298–358 K. DMM is diluted in Air.

4.1.3. Plug Flow Reactors

Figures 4.5, 4.6, and 4.7 display the species concentration data obtained from Marrodan et al. [27] in a PFR under varying conditions of λ (i.e., fuel-air ratio, $\lambda = 0.7/1/20$). The experiments were conducted over a wide range of pressures (20-60 bar) and temperatures (400-1100 K).

The three mechanisms provided satisfactory representations of the DMM mole fraction but overestimated its reactivity at lower temperatures, particularly at high pressures and λ values. CO and CO_2 showed some inconsistencies, particularly at T $>$ 700 K, indicating incomplete combustion in the models. The lumping process caused modifications in the simulation results, leading to poor accuracy in intermediate combustion species like CH_3OCHO, CH_2O and CH_4. Even if these datasets were not employed as optimization targets, the good agreement of the obtained results confirms the consistency of this approach.

The final mechanism also led to performance improvements for CH_4 too, describing. But for other species, like for CH_3OCHO and CH_2O, the poor agreement of the lumped model is only partially recovered, in both cases the production and the subsequent destruction are way too anticipated with decreasing both the λ and the pressure.

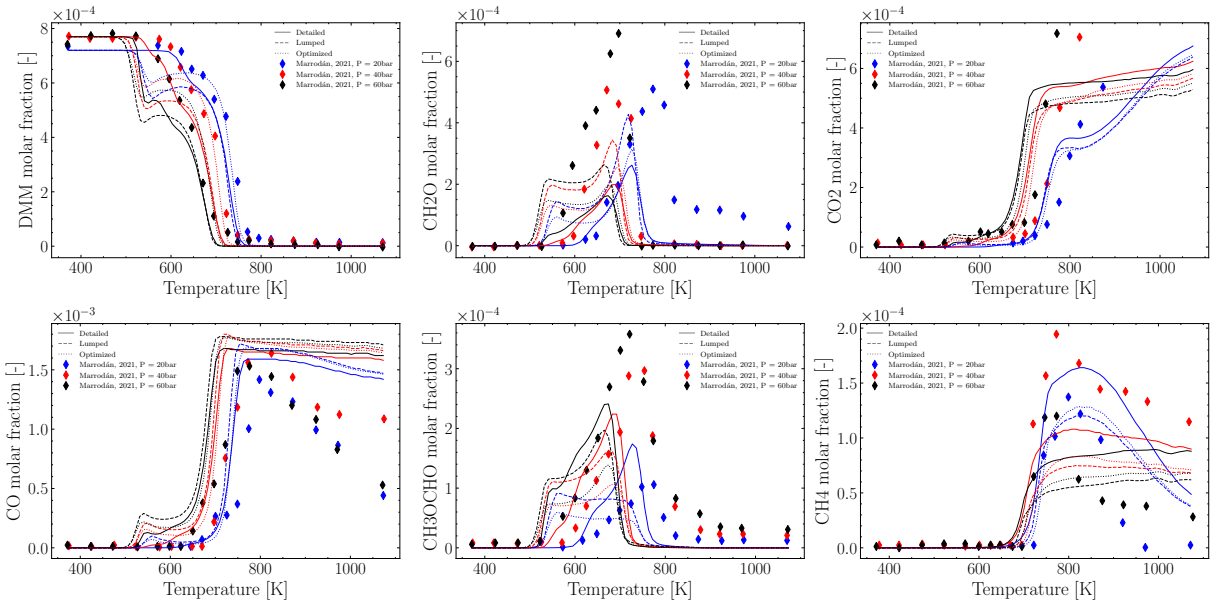

Figure 4.5: Marrodan et al. [27] experiments on DMM combustion in a PFR, measuring species mole fractions and comparing to model predictions. The experiments were carried out under conditions of $\lambda = 0.7$ and P = 20-60 bar, with DMM and O_2 diluted in N_2.

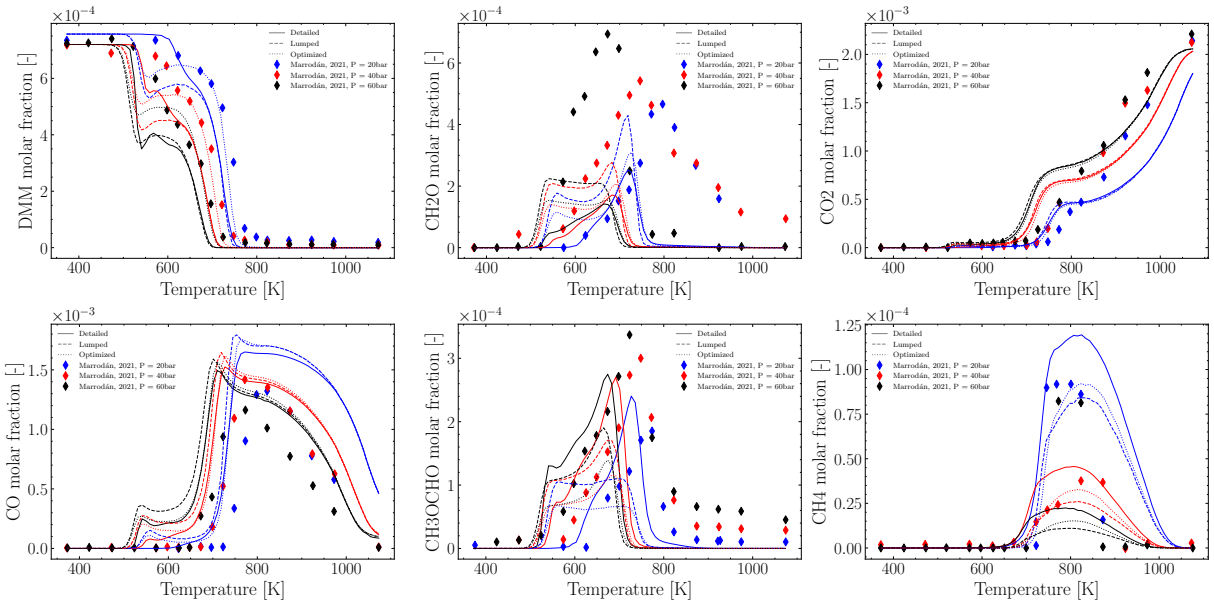

Figure 4.6: Marrodan et al. [27] experiments on DMM combustion in a PFR, measuring species mole fractions and comparing to model predictions. The experiments were carried out under conditions of $\lambda = 1$ and P = 20-60 bar, with DMM and O_2 diluted in N_2.

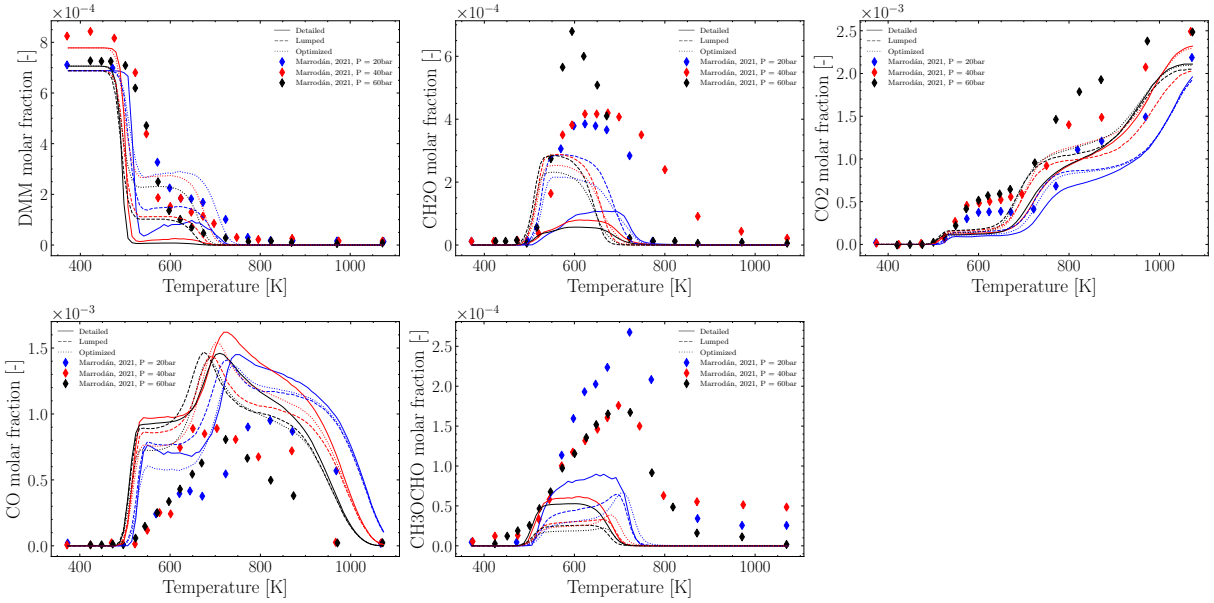

Figure 4.7: Marrodan et al. [27] experiments on DMM combustion in a PFR, measuring species mole fractions and comparing to model predictions. Experiments were carried out under conditions of $\lambda = 20$ and P = 20-60 bar, with DMM and O_2 diluted in N_2.

4.1.4. Jet Stirred Reactors

Figure 4.8 displays the concentrations of various species measured by Vermeire et al. [28] and their corresponding simulations. The JSR reactor was operated at near atmospheric pressure and temperatures ranging from 600 to 1100 K, with equivalence ratios ranging from 0.5 to 2. Simulations for equivalence ratio of 1 were only carried out for temperatures below 1000 K, as no steady-state solution could be found for higher temperatures [97].

The models accurately reproduced the mole fractions of O_2, CO, and CO_2, while CH_4, C_2H_4, and C_2H_6 exhibited minor errors, especially in the lumped model, which were corrected by the optimized one. The predictions for DMM were also quite accurate, and the optimized model improved the predictions for DMM with increasing equivalence ratio. The optimized model also improved the profiles of CH_2O and CH_3OCHO, which were better than those of the lumped model but still not very accurate.

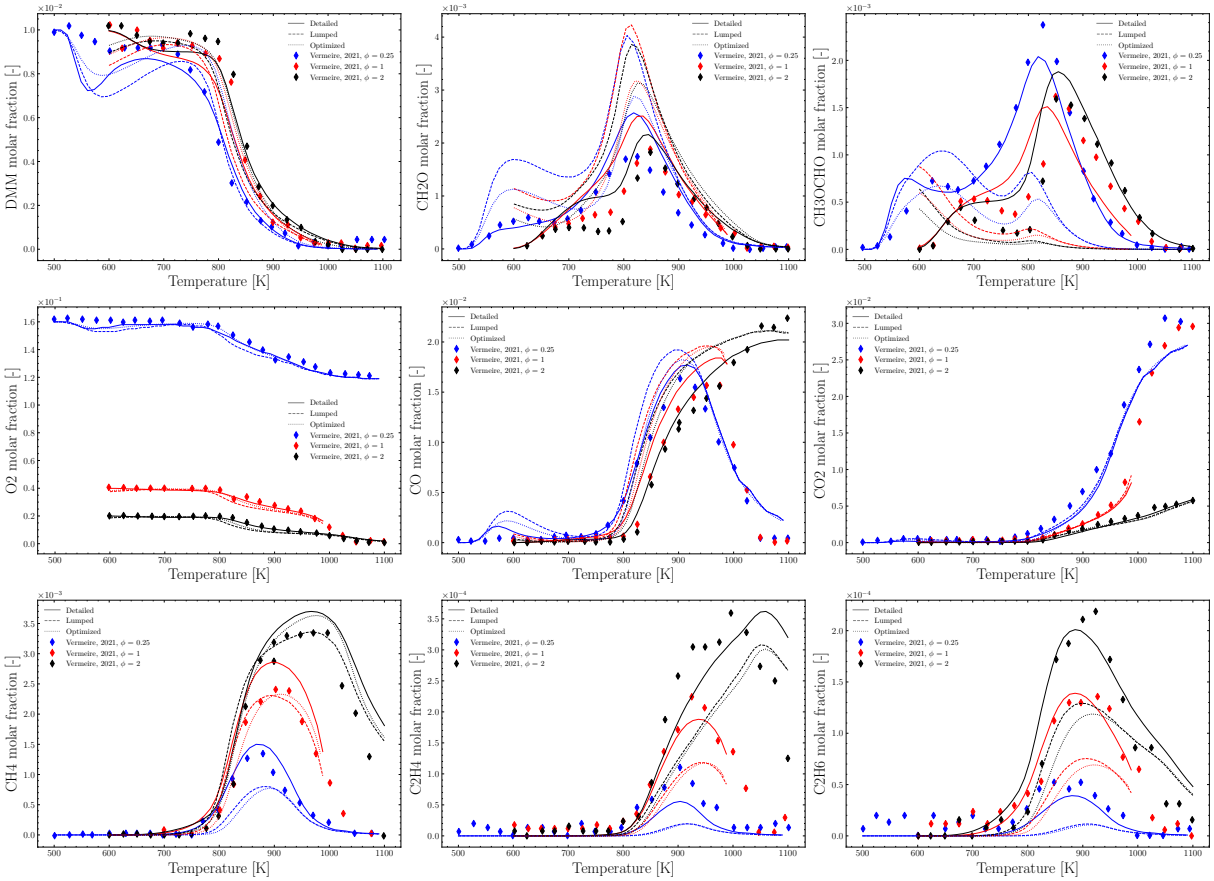

Figure 4.8: Vermeire et al. [28] experiments on DMM combustion in a JSR, measuring species mole fractions and comparing to model predictions. Experiments were carried out at $\phi = 0.5$–2 and P = 1.07 bar. DMM is diluted in 99% O_2 and Air.

4.1.5. Conclusions

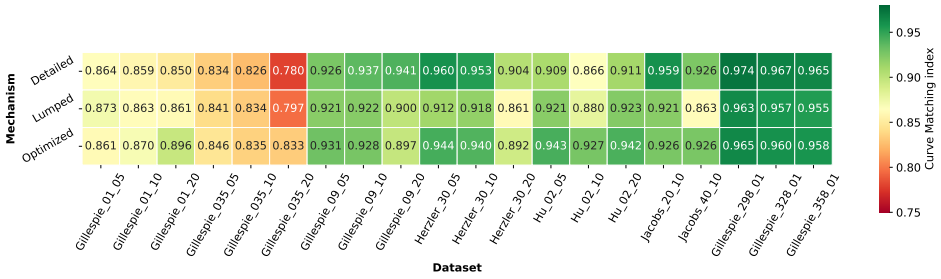

Figure 4.9: Heatmap of the CM score obtained per each simulation of IDTs and LFSs.

Figure 4.9 displays a heatmap that summarizes the CM scores of IDTs and LFSs of DMM according to the author and mechanism for the purpose of facilitating performance comparisons.

High indices of LFSs indicate a close match between detailed kinetics and experimental results, and neither the lumping nor optimization procedures significantly impacted the predictions since controlling reactions remained unchanged.

The IDTs that the detailed mechanism forecasted are highly similar to the results obtained in the experiments conducted by Gillespie, Herzler et al., and Hu et al., especially at medium to high pressures. However, it is important to point out that the accuracy of the detailed and lumped mechanisms is lower for the simulations conducted at low pressures by Gillespie, specifically at P = 3.5 bar. Nonetheless, the optimized mechanism has managed to recover most of the accuracy in these low-pressure simulations.

The optimization approach used proved successful in maintaining the consistency of the model, as demonstrated by the higher performance of nearly all optimized mechanism indices compared to those of the other two mechanisms.

4.2. OME_2

The experimental dataset for OME_2 is composed of 15 sets of data, depicted in Figure 4.10. These datasets comprise ignition delay times (IDTs) measured in shock tubes [23] and laminar flames [29–31]. Due to the lack of availability in literature of speciation data for this species, these type of experiments are not employed in this validation. Out of these 15 datasets, only two of them (as listed in Section 3.6.1) were utilized as optimization targets, while the other 13 were used for final validation purposes.

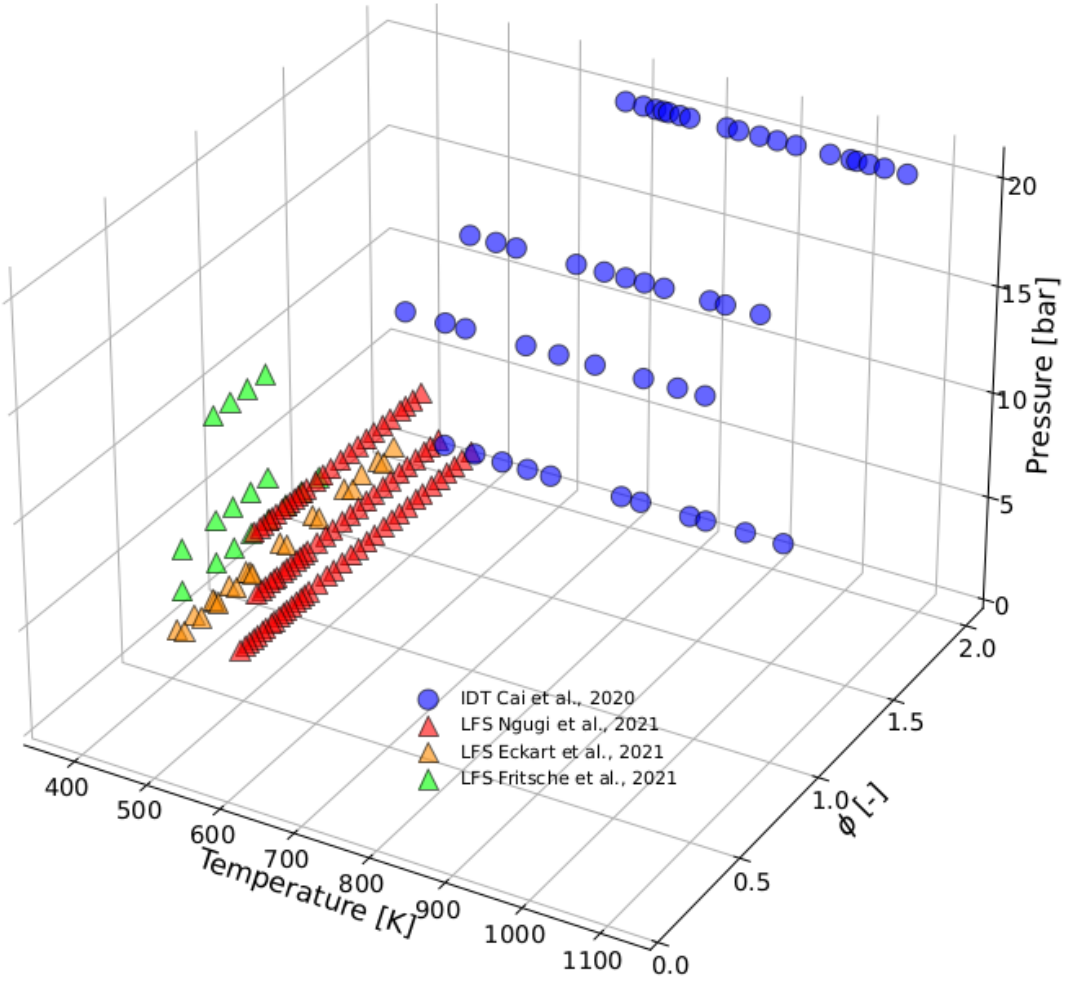

Figure 4.10: Database of experimental values for OME_2.

4.2.1. Ignition Delay Times

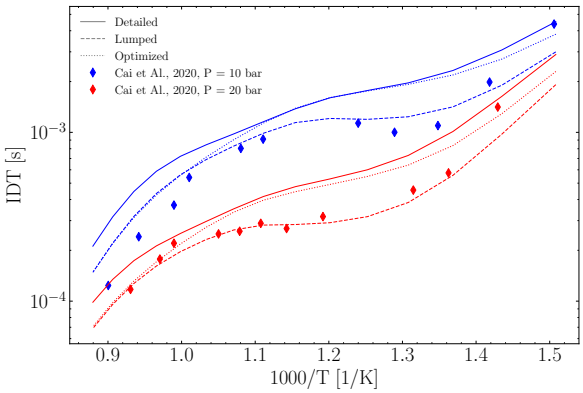

(a) IDTs of OME_2/Air at $P = 10 - 20bar$ and $\phi = 1$.

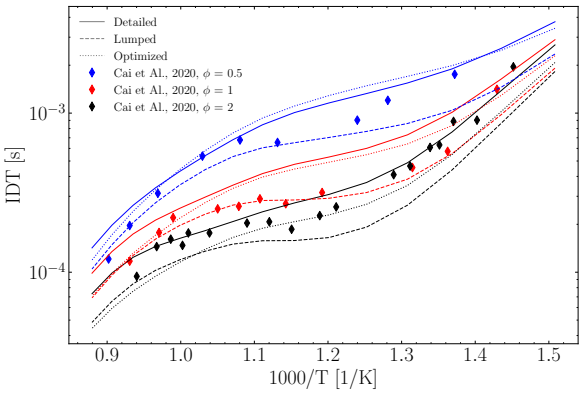

(b) IDTs of OME_2/Air at $P = 20bar$ and $\phi = 0.5$-2.

Figure 4.11: IDTs of OME_2 measured in a ST by Cai et al. [23] diluted in Air, compared with the detailed mechanism (solid line), the lumped one (dashed line) and the optimized too (dotted line).

The IDTs of OME_2 were obtained in a ST by Cai et al. [23], with a range of operating conditions including temperatures of approximately 650-1100 K, equivalence ratios of 0.5-2, and pressures of 10-20 bar. The figure depicting the experimental results and model predictions can be found in Figure 4.11.

The detailed mechanism overestimated IDTs for the majority of the relevant operating conditions. This was especially true at $\phi = 1$ and P = 20 bar, and it did not exhibit a significant negative temperature coefficient (NTC) effect that was seen in the experimental data. By contrast, the lumping procedure generally accelerated the kinetics and resulted in a more pronounced NTC effect, leading to improved model accuracy. The optimized solution tends to better replicate the detailed model at lower temperatures and the lumped model at higher temperatures in both scenarios. However, the optimization sometimes resulted in worse predictions, particularly for $\phi = 1$. Although the detailed model already performed well at $\phi = 2$ and P = 20 bar, the lumped mechanism was found to be too fast.

Figure 4.12 presents a sensitivity analysis conducted at $\phi = 1$, $P = 20bar$, and $T = 900K$ and at three different times, according to the methodology presented in Section 3.2. The initial and ultimate times refer to the point at which only 1% of OME_2 has undergone conversion and the point at which almost all of the OME_2 has reacted, with a conversion of $\chi = 0.99$. The analysis verifies that the reactions utilized in the optimization are the most sensitive ones, thereby validating the approach and the favorable outcomes achieved.

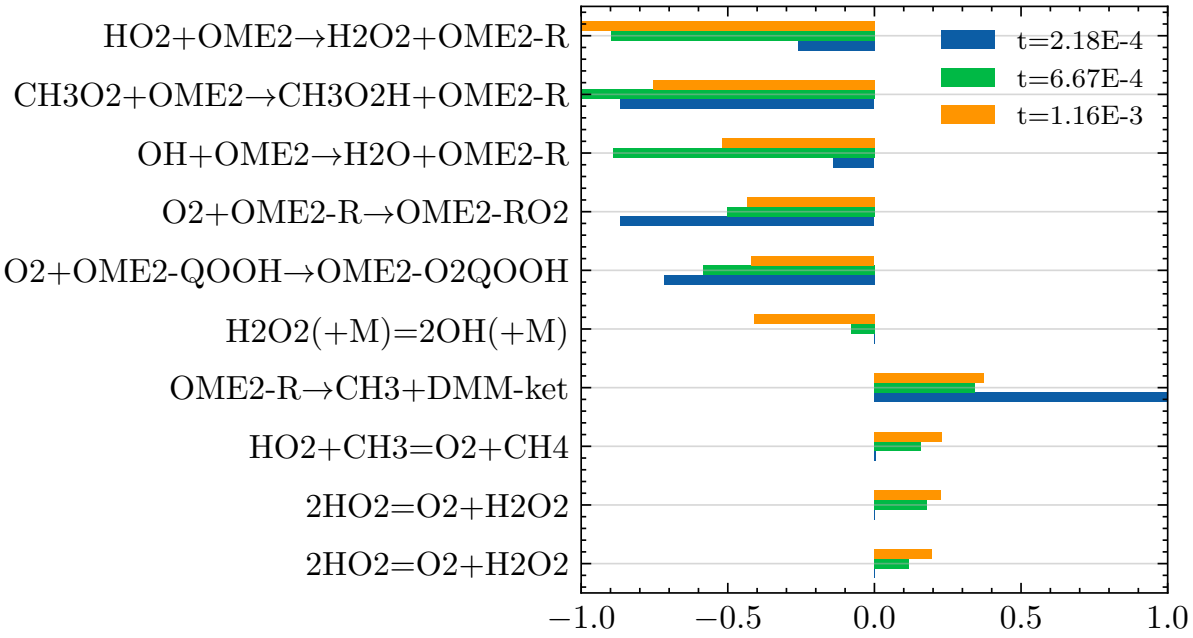

Figure 4.12: Sensitivity analysis conducted at $\phi = 1$, $P = 20bar$, and $T = 900K$

Figure 4.12 illustrates that the reactions of interest are significant both at lower and higher times, as the radical species formed in the beginning (such as CH_3 and CH_3O_2) contribute to the combustion propagation, while the lighter species (H and OH) play a crucial role in the later stages.

The sensitivity analysis indicates that the most sensitive reaction is the $H-abstraction$ by HO_2, which produces the radical H_2O_2 that subsequently decomposes into 2 OH radicals. The latter reaction displays a high sensitivity coefficient at later time when the first one becomes crucial and the species H_2O_2 is produced.

4.2.2. Laminar Flame Speeds

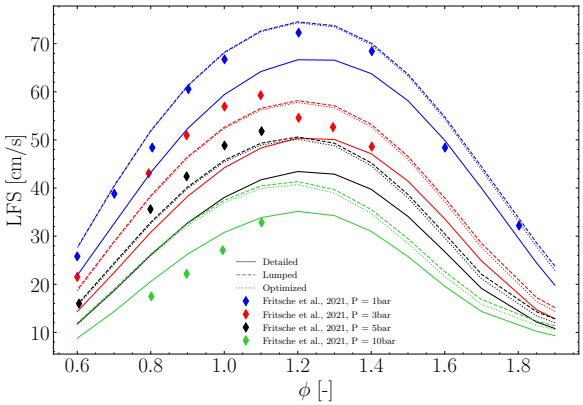

(a) LFSs of OME_2/Air at $P = 1 - 10bar$ and $T = 393K$.

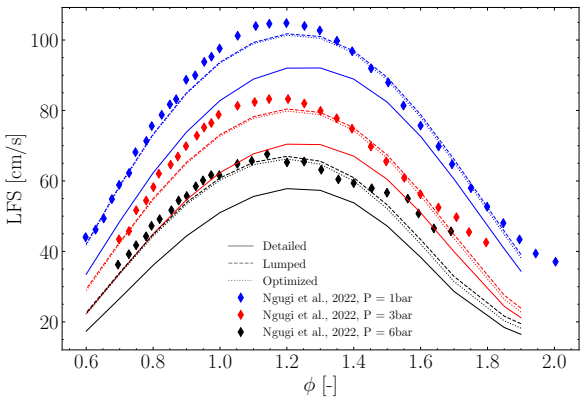

(b) LFSs of OME_2/Air at $P = 1 - 6bar$ and $T = 473K$.

Figure 4.13: LFSs of OME_2 measured by Fritsche et al [29] (Figure 4.13a) and Ngugi et al. [30] (Figure 4.13b) diluted in air, compared with the detailed mechanism (solid line), the lumped one (dashed line) and the optimized too (dotted line).

Eckart et al. [31], Fritsche et al. [29], and Ngugi et al. [30] collected the Laminar Flame Speed of OME_2 under various operating conditions, including temperatures ranging from 383 K to 473 K, equivalence ratios of 0.6 to 2, and pressures of 1 to 10 bar.

Figure 4.13 displays a comparison of the LFSs measured by Fritsche et al. and Ngugi et al. with the simulation results from the three mechanisms investigated. The detailed model consistently under-predicts the LFSs by up to 20 cm/s across all cases from ϕ = 0.6 to 1.2, except for the dataset at T = 393 K and P = 10 bar by Fritsche et al. Fig. 4.13a, where it is quite accurate. The lumped mechanism shows a significant acceleration, resulting in an improvement of all predictions except for the 10 bar dataset, which is now overestimated.

The optimized mechanism mirrors the performance of the lumped model, maintaining its good accuracy. Unfortunately, the 10 bar dataset in Figure 4.13a still exhibits poor predictions without any improvement. This is inevitable since any improvement would have conflicted with the accurate reproduction of all other LFSs, as also demonstrated by the datasets from Eckart et al. in Figure 4.14 investigated at constant temperature. Furthermore, in these experiments, the detailed model demonstrates a tendency to underestimate each dataset to a greater degree as the temperature increases. While the lumped model endeavors to bridge this disparity, the optimization process falls short due to insufficient data, especially at T = 388 K and T = 401 K. It should also be noted that none of the LFS datasets were used as an optimization target.

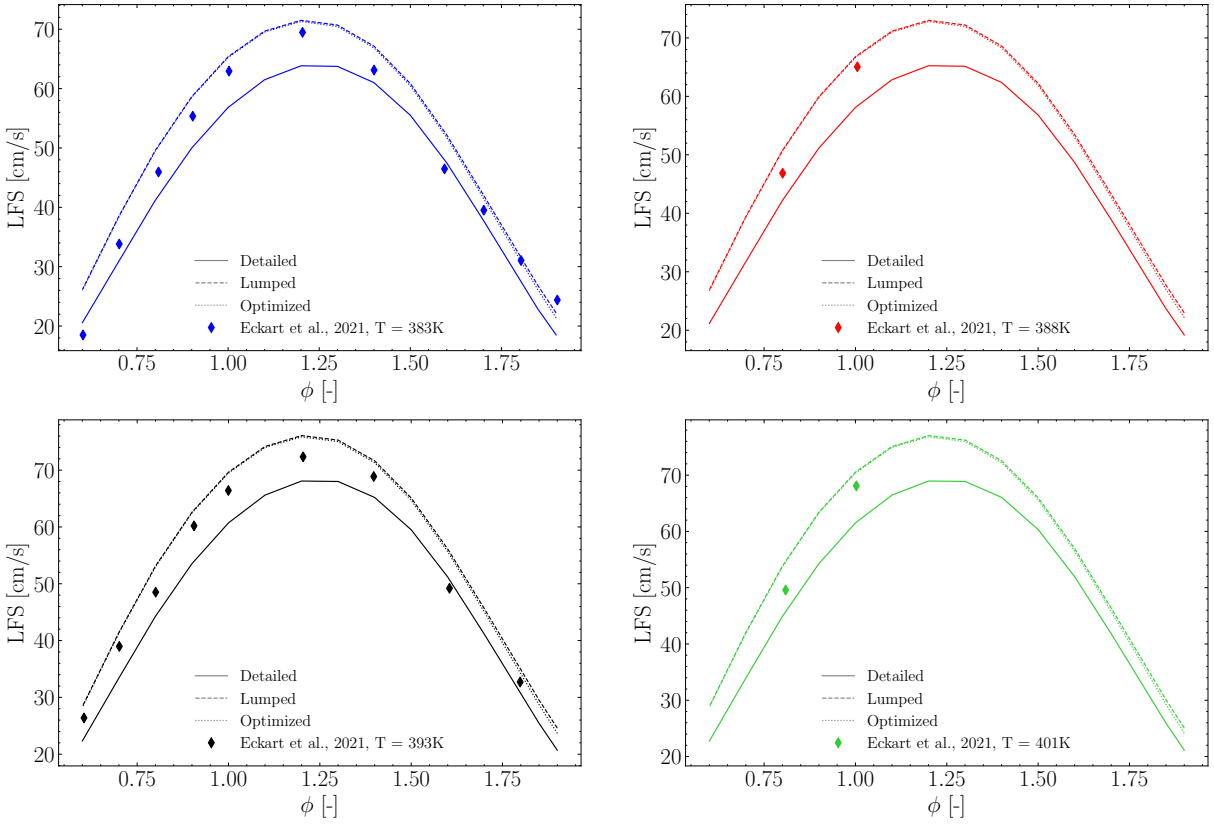

Figure 4.14: OME_2 LFSs measured by Eckart et al. [31] diluted in air, compared with the detailed mechanism (solid line), the lumped one (dashed line) and the optimized too (dotted line). The operative conditions are: P = 1 bar T = 383–401 K.

4.2.3. Conclusions

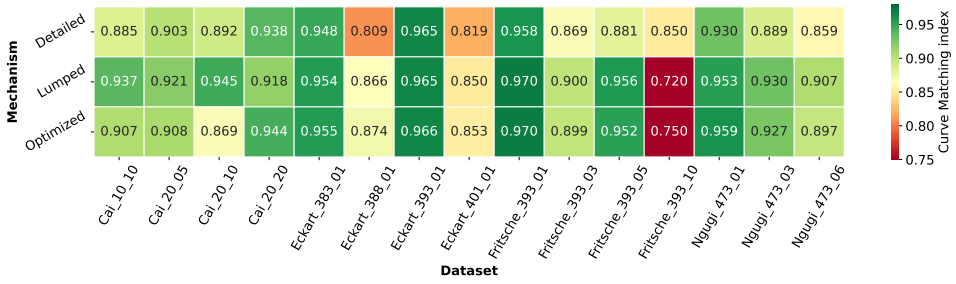

Figure 4.15: Heatmap of the CM score obtained per each simulation of IDTs and LFSs.

The heat map presented in Figure 4.15 displays all the CM scores that evaluate the performance of the OME_2 simulations. The Figure is organized according to the author and mechanism for the purpose of facilitating performance comparisons. The IDTs and LFSs scores provide quantitative confirmation of the qualitative observations seen in the plots.

The lumped model generally reproduces IDTs more accurately, and therefore, optimization is not necessary. However, the lumped reactivity increase negatively affects the $\phi = 2$ and P = 20 bar case, which is deeply recovered by the final mechanism outperforming the detailed model too.

The detailed model is less accurate than the lumped one in predicting LFSs too. Optimization leads to minor improvements also because neither of these experimental data were used as optimization targets. The datasets at P = 10 bar and T = 393 K, collected by Fritsche et al. [29], confirm previous findings that both the lumped mechanism and the optimized one tend to overestimate experimental data. Regarding the dataset of Eckart et al., the optimized mechanism shows a higher level of conformity to the experimental data compared to the two models.

4.3. OME_3

The collection of experimental data for OME_3 consists of 9 datasets, as illustrated in Figure 4.16. These datasets comprise IDTs measured in STs [23] and LFSs [29, 32], while no speciation information is available in the literature yet. Out of the 9 datasets, 2 were selected as optimization targets, whereas the remaining 7 were utilized for model validation. Further information can be found in Section 3.6.1.

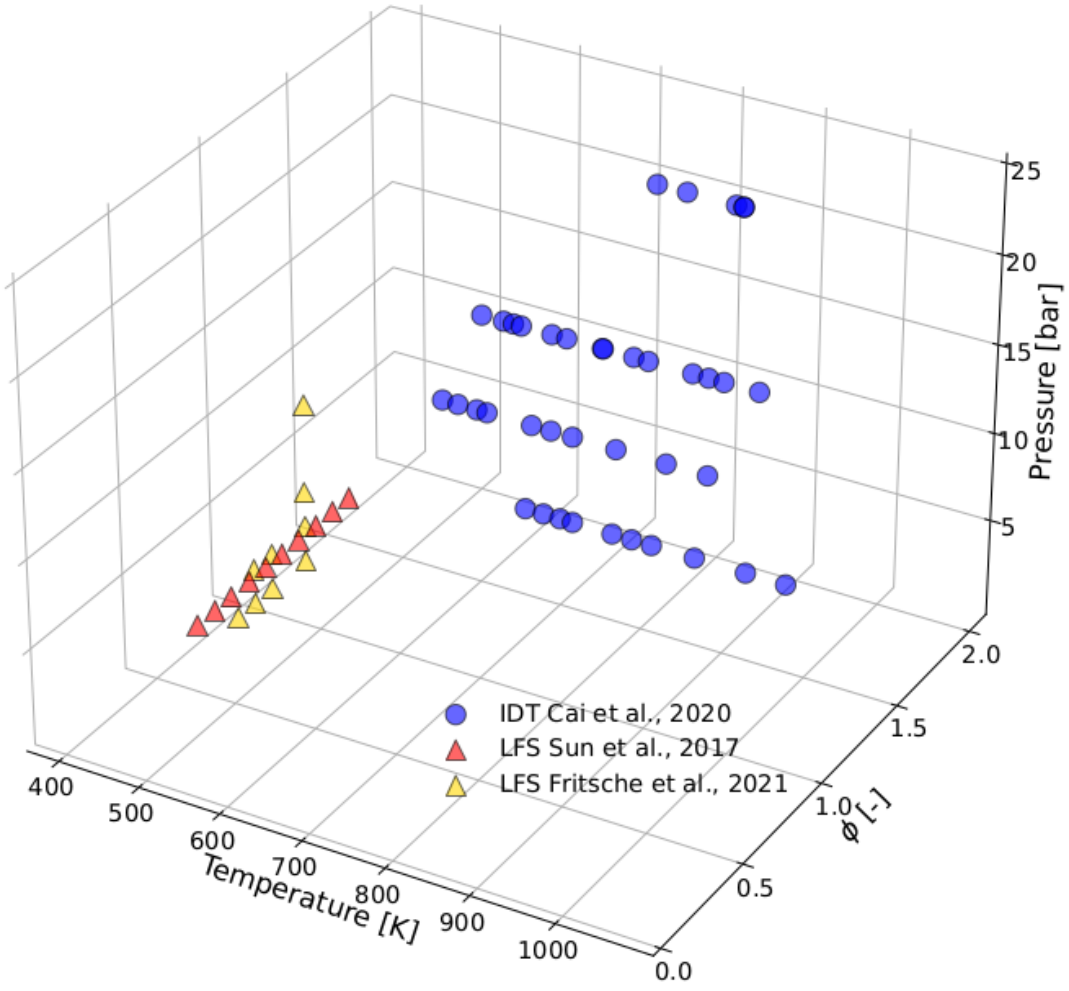

Figure 4.16: Database of experimental values for OME_3.

4.3.1. Ignition Delay Times

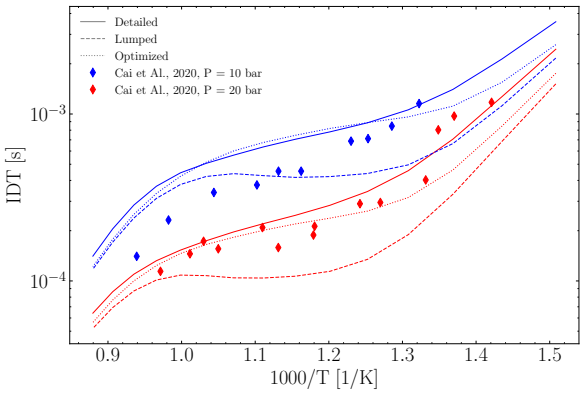

(a) IDTs of OME_3/Air at $P = 10 - 20bar$ and $\phi = 1$.

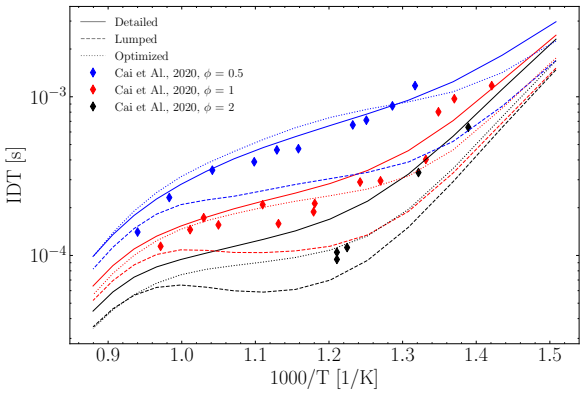

(b) IDTs of OME_3/Air at $P = 20bar$ and $\phi = 0.5$-2.

Figure 4.17: IDTs of OME_3/Air measured in a ST by Cai et al. [23] diluted in air, compared with the detailed mechanism (solid line), the lumped one (dashed line) and the optimized too (dotted line).

IDTs results in STs for OME_3 were obtained by Cai et al. [23] at T = 700–1100K, ϕ =0.5–2 and P = 20bar, and are presented in Figure 4.17 alongside the models' predictions.

Unlike OME_2, the detailed model demonstrates reasonable agreement with the experimental data for the relevant conditions. Therefore, the acceleration of the lumping procedure has resulted in a decline in the mechanism's performance. However, this enhancement of the NTC effect of the lumped model improved the agreement between the model and data for the simulation conducted at $\phi = 2$ bar and P = 20 bar. The optimization process has significantly impacted the IDTs of OME_3, reducing its reactivity at low temperatures and bringing the optimized mechanism closer to the original detailed one. This can be observed in Figure 4.17b, where the optimized model closely reproduces the detailed model with high accuracy.

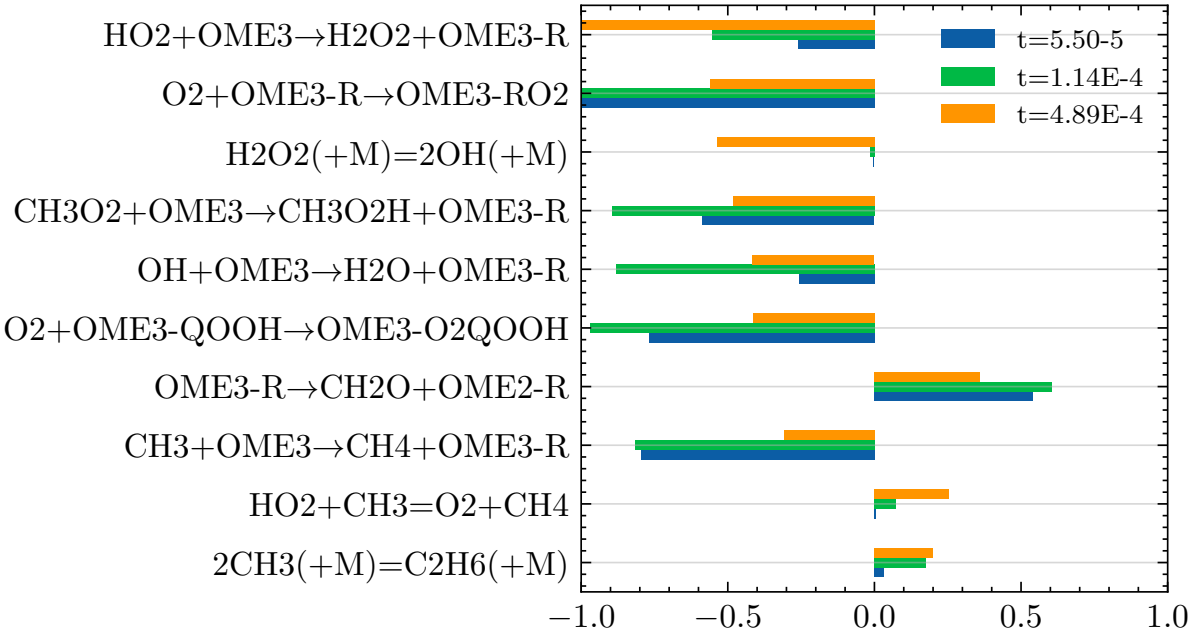

Figure 4.18: Sensitivity analysis performed at $\phi = 1$, $P = 10bar$ and $T = 950K$.

Figure 4.18 presents a sensitivity analysis conducted at $\phi = 1$, $P = 10bar$, and $T = 950K$. The analysis verifies that the reactions utilized in the optimization are the most sensitive ones, thereby validating the approach and the favorable outcomes achieved.

As for OME_2, the most sensitive reaction is the $H - abstraction$ by HO_2 due to the fact that it produces H_2O_2 which reacts forming 2 OH radicals. The sensitivity coefficient is higher for the reaction $H_2O_2 \rightarrow 2OH$ due to the higher temperature chosen at which the sensitivity analysis was performed.

4.3.2. Laminar Flame Speeds

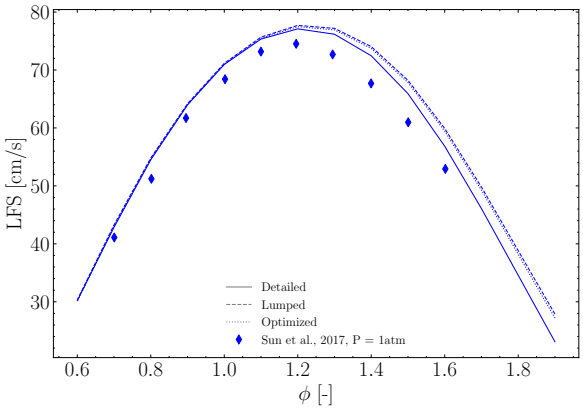

(a) LFSs of OME_3/Air at $P = 1atm$ and $T = 408K$.

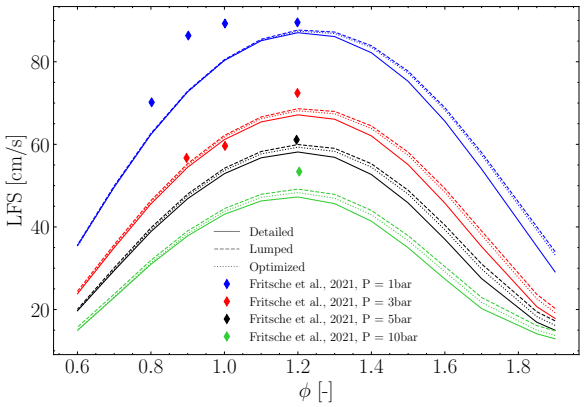

(b) LFSs of OME_3/Air at $P = 1 - 10bar$ and $T = 438K$ and .

Figure 4.19: LFSs of OME_3 measured by Sun et al. [32] (Figure 4.19a) and Fritsche et al. [29] (Figure 4.19b) diluited in air, compared with the detailed mechanism (solid line), the lumped one (dashed line) and the optimized too (dotted line).

Figure 4.19 displays the LFS measurements carried out by Sun et al. [32] and Fritsche et al. [29], as well as the simulation outcomes of the models. The studies focused on the following set of conditions: T = 408-438 K, ϕ = 0.7-1.6, and P = 1-10 bar.

The dataset from Sun et al. is reasonably well predicted by the detailed mechanism, with an overestimation of less than 5 cm/s only for rich conditions. However, both the lumped and optimized models show a slight worsening in performance compared to the detailed mechanism at higher ϕ (i.e., rich conditions), enhances the error introduced by the detailed model. On the other hand, for all pressures, the datasets by Fritsche et al. are under-predicted, with only the dataset at P = 3 bar showing good agreement. It is worth noting, however, that the limited availability of data for higher pressures reduces the reliability of the evaluation.

4.3.3. Conclusions

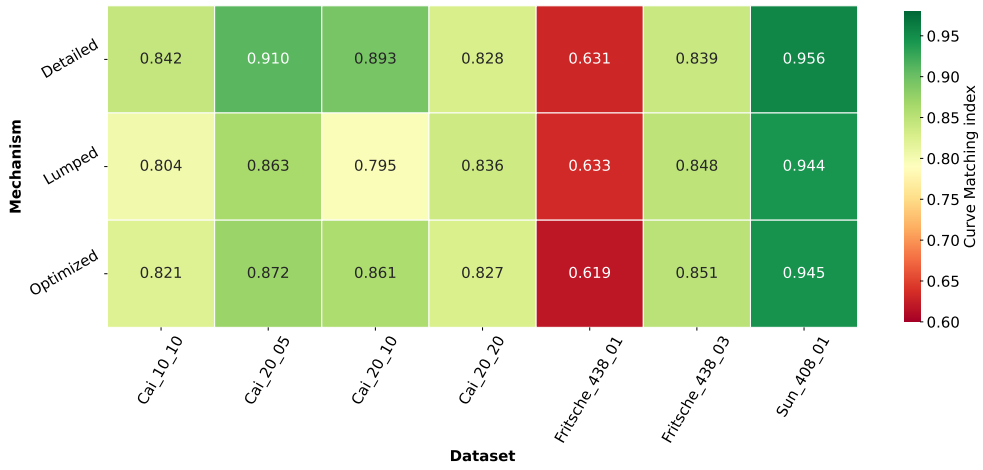

Figure 4.20: Heatmap of the CM score obtained per each simulation of IDTs and LFSs.

The performance of OME_3 models was quantitatively determined using CM indices, and the results were presented in Figure 4.20 as a heat map.

The IDTs were found to slightly deteriorate with increasing kinetics acceleration due to lumping, except for the simulation at $\phi = 2$ and P = 20 bar. However, the final optimized model was able to recover most of the original accuracy.

In contrast, the CM indices of LFSs could not be evaluated for the datasets of Fritsche et al. at P = 5-10 bar due to the presence of single data points, and the ones that could be evaluated showed poor performance due to the small number of data entries. The scores for the experiments conducted by Sun et al. were able to accurately reflect the good behavior of the models in reproducing the data.

4.4. OME_4

Figure 4.21 illustrates the five datasets included in the OME_4 experimental database, which comprise IDTs in STs [23] and LFSs [33]. Unfortunately, as in the case of OME_2 and OME_3, speciation informations of PFR and JSR are not yet available. Due to the limited quantity of data, both datasets of IDTs were used as optimization targets.

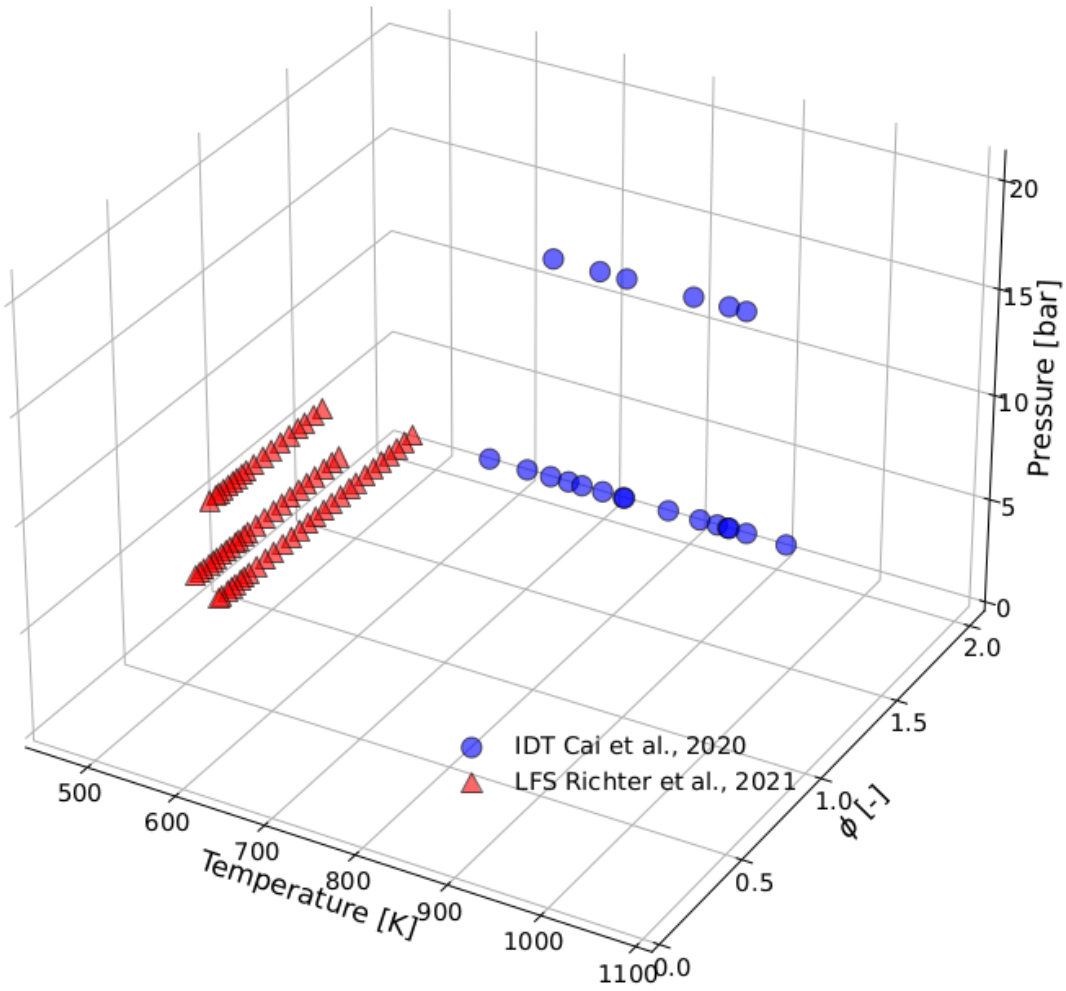

Figure 4.21: Database of experimental values for OME_3.

4.4.1. Ignition Delay Times

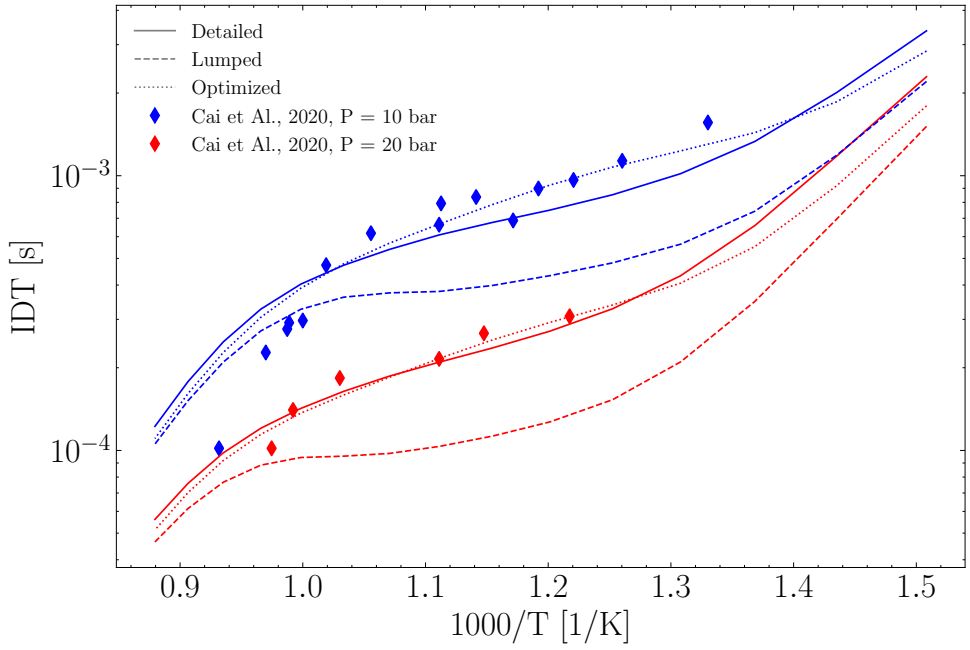

Figure 4.22: IDTs of OME_4 measured in a ST by Cai et al. [23], compared with the detailed mechanism (solid line), the lumped one (dashed line) and the optimized too (dotted line). OME_4 is diluted in air.

The sole available IDTs for OME_4 were obtained in a ST by Cai et al. [23] at T = 750–1050K, $\phi = 1$, and P = 10–20 bar.

The detailed mechanism accurately replicates the experimental data. However, similarly to OME_3, the lumped model is too rapid by a factor of approximately 2 and exhibits a noticeable NTC behavior. The optimized kinetics address these issues and precisely model the experimental data closing the gap between the model and experimental data. However, at higher temperatures and P = 10 bar, the optimized mechanism experiences some losses in accuracy, but it corrects the larger overestimation of the detailed model thus resulting in a better agreement.

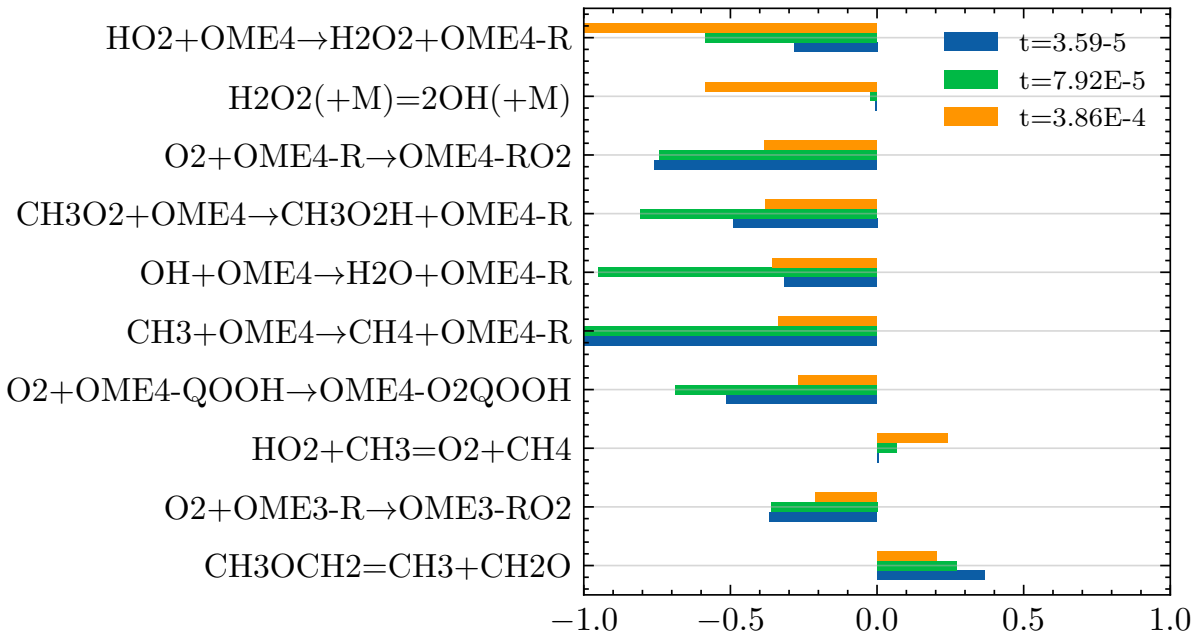

Figure 4.23: Sensitivity analysis conducted at $P = 10bar$, $T = 100K$, and $\phi = 1$.

In the same ST reactor, sensitivity analyses were conducted at three different characteristic times, as described in Section 3.2. Figure 4.23 indicates that the reactions used in the optimization are highly significant, as confirmed by the local sensitivity analysis carried out under the conditions of $P = 20bar$, $T = 870K$, and $\phi = 1$.

The H-abstractions are crucial in this case as they are part of the reactions that regulate the progression of the process. Therefore, optimizing these reactions is a valid choice. However, during the initial stages, it becomes evident that the oxidation of OME_4−QOOH is not as critical as for OME_2 and OME_3. This is due to the minimal production of OME_4−O_2QOOH at high temperatures, which is rapidly destroyed. The situation is reversed below about 1000 K. The reaction involving OME_4−O_2QOOH drives the oxidation, making it highly sensitive. It is worth noting that at such high temperature, the sensitivity coefficient of the reaction $H_2O_2 \rightarrow 2OH$ is higher than the one observed for OME_2 and OME_3.

4.4.2. Laminar Flame Speeds

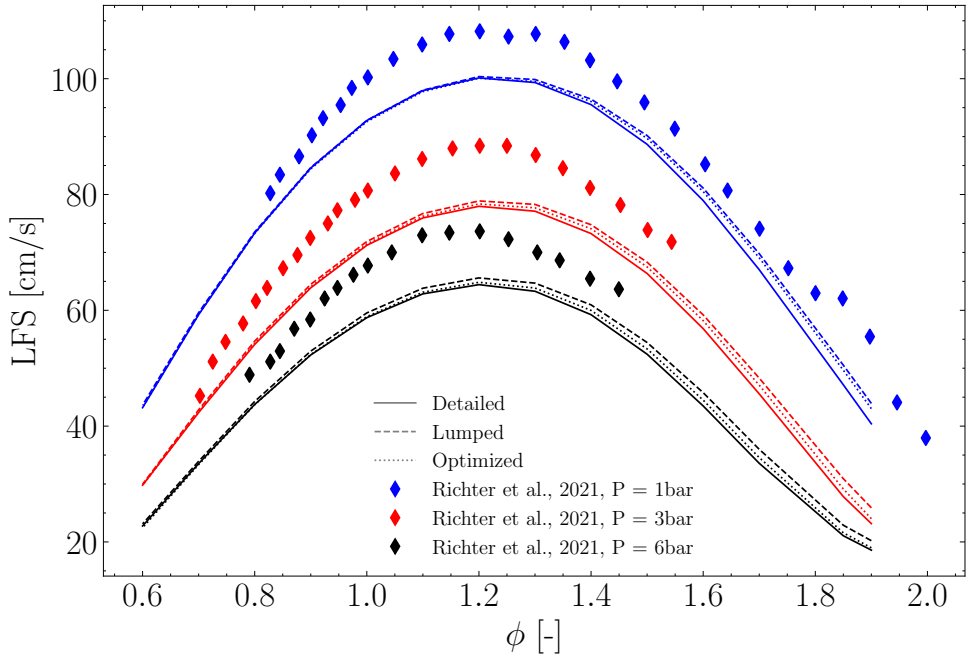

Figure 4.24: LFSs of OME_4 measured by Richter et al.[33] compared with the detailed mechanism (solid line), the lumped one (dashed line) and the optimized too (dotted line). OME_4 is diluted in air. Experiments are carried out at P = 1–6 bar and T = 473 K.

Richter et al. [33] have quantified the LFS measurements of OME_4 and presented them in Figure 4.24. The desired operating conditions are T = 473K, ϕ = 0.7–2, and P = 1–6 bar.

The detailed model and the nearly identical lumped model both underestimate the flame velocity by about 15 cm/s, particularly near the maximum value at $\phi \simeq 1.2$. Despite the optimized model, it appears unable to bridge this discrepancy with the experimental data because the reactions utilized in the optimization do not consider the C_1-C_3 reactions, which are crucial for these kinds of experiments.

4.4.3. Conclusion

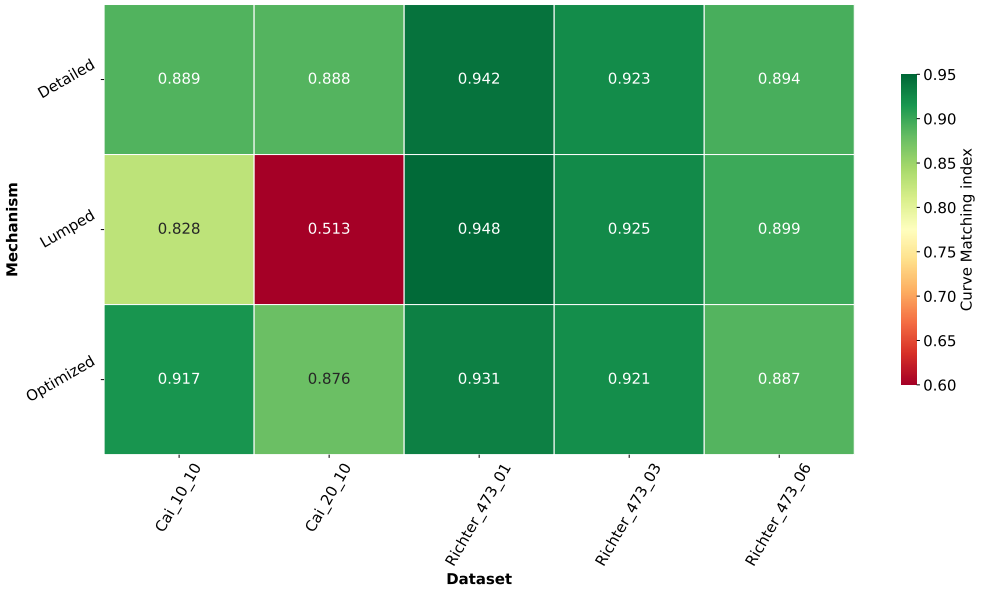

Figure 4.25: Heatmap of the CM score obtained per each simulation of IDTs and LFSs.

In Figure 4.25, the CM scores for the OME_4 datasets are summarized.

The lumping process was applied to improve LFSs predictions by increasing fuel burning velocity, but this negatively affected IDTs performance due to higher reactivity.

The poor agreement of the lumped model with the experimental results is completely recovered by the optimized model, which outperformed the initial detailed model in all cases, indicating that the selection of reactions to optimize and experimental targets was appropriate. However, the score of the lumped mechanism for IDTs at $\phi = 1$ and P = 20 bar is notably low, which can be partly attributed to the smaller amount of data available for these conditions, leading to a negative influence on curve comparison. Although the lumped model exhibited similar qualitative behaviors in both conditions, the smaller domain of experimental data at P = 20 bar caused a deterioration in the index.

5 | Conclusions and future developments

In the field of combustion, it is common to use models to simulate experiments to save time and resources. The importance of detailed kinetics has been recognized and can be implemented in heavy simulations for small fuels, but becomes limited when dealing with more complex molecules. This is due to the large number of species that must be described and the resulting increase in the number of transport equations to be solved. As a result, detailed models of heavy molecules cannot be used in demanding tasks such as CFD applications without becoming computationally unsustainable. Therefore, the search for reduced mechanisms plays a key role in chemical kinetics to find a good trade-off between accuracy and model size.

OMEs are a type of innovative fuel that is gaining attention due to their ability to reduce soot and NOx as a diesel additive. It can be blended with diesel without significantly altering its combustion, making it suitable for use in current engines with minimal modifications [23, 35, 42]. However, the available mechanisms describing OMEs are detailed and suffer from the aforementioned limitations. Hence, a reduced model is necessary to expedite CFD studies on combustion in engines.

It is important to ensure that the reduced model reflects the key features of the detailed model and preserves the physical consistency of the chemistry of the process being simulated. This is because the reduced model is used as a substitute for the detailed model and any inaccuracies in the reduced model can affect the accuracy of the simulation results. Therefore, an optimization process is required to recover the performance of the detailed model while ensuring that the reduced model remains physically consistent.

5.1. Results

In this work, a data-driven, class-based optimization methodology was applied to calibrate the reaction rate of different classes of reaction. The presented method resulted in a

kinetic mechanism that is consistent with the underlying chemistry, while also achieving good agreement with experimental data, including data points that were not included in the optimization process.

The methodology largely reduces the number of parameters to be considered and therefore it is applicable even in the case where a large number of important reactions are present. The methodology allows the discovery and calibration of parameters that are difficult to obtain with computational chemistry tools or experimental measurements, or which have not been studied yet. The new kinetic model is finally validated among wide experimental data, including IDTs from ST reactor, speciation in JSR and PFR, and laminar flames measurement.

Figure 5.1 presents the average CM index for the three models compared in this study, providing an objective evaluation of their agreement with experimental data. The CM index ranges from 0 to 1, with 1 indicating perfect agreement and 0 indicating maximum disagreement. According to the results, the new optimized approach demonstrates superior performance compared to the other models for all fuels, particularly for DMM and OME_2, where it even outperforms the detailed model. For OME_3 and OME_4, the optimized approach achieves the same level of performance as the detailed model. These outcomes confirm the success of the procedure in achieving a higher level of consistency while maintaining accuracy.

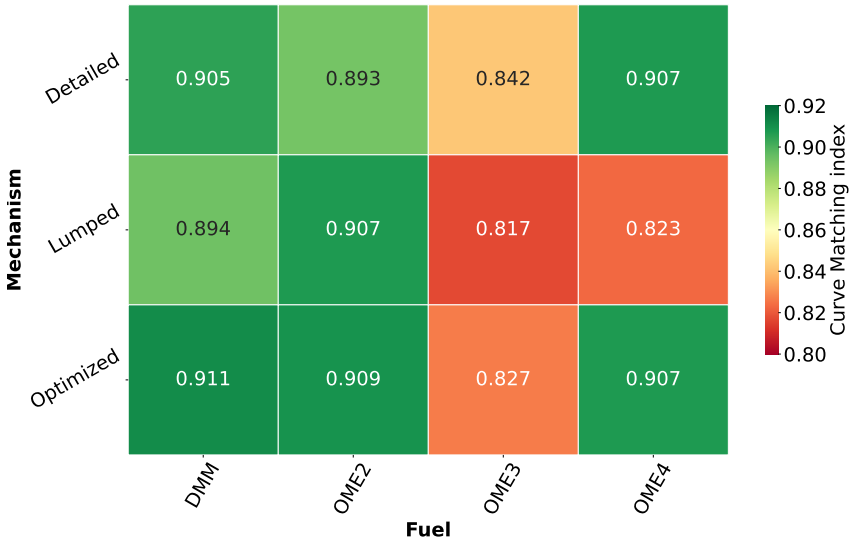

Figure 5.1: Summary of the average CM index for the three models examined per fuel.

5.2. Future work

The results obtained in this work show several interesting applications of this feature now fully implemented in `OptiSMOKE++`. First of all, it guarantees a more physical consistency between the lumped kinetic model and the detailed one. The results of the optimization itself are in many cases better than the local optimization of different reactions. Of course, there is still room for several improvements so, to conclude, a list of the possible future works it is discussed in this final part.

5.2.1. Selection of the classes

In the context of chemical kinetics, the detailed mechanism can be quite complex and challenging to work with due to the large number of species and reactions involved. Therefore, it can be helpful to divide the mechanism into classes based on similarities in chemical structure or reaction pathways. This allows for a more systematic and organized approach to analyzing the mechanism and mapping its behavior. By performing a sensitivity analysis, one can identify the most important classes and refine the selection to achieve better accuracy and computational efficiency. This can lead to a more efficient and accurate model for studying chemical kinetics and related processes. In Appendix B, there is a comprehensive list of the most sensitive reactions along with their corresponding sensitivity coefficients at the condition described in Chapter 3. In Figure 5.2 it is possible to the reactions with a sensitivity coefficient until $|0.65|$.

5.2.2. Kinetic mechanism

Once the classes have been identified, a lumped kinetic mechanism can be constructed based on these classes. This involves combining the reactions and species in each class into a single entity, reducing the total number of species and reactions in the mechanism. The lumped mechanism can then be used to simulate the chemical system of interest, while also providing insights into the key reaction pathways and species that drive the overall behavior.

The development of a lumped kinetic mechanism involves some level of simplification, as the individual reactions and species within each class are combined into a single entity. However, this simplification can greatly reduce the computational cost of simulating the chemical system, making it more feasible to perform complex simulations such as those involved in computational fluid dynamics (CFD) studies.

The idea is to use this class-based approach to develop a kinetic scheme for higher OME

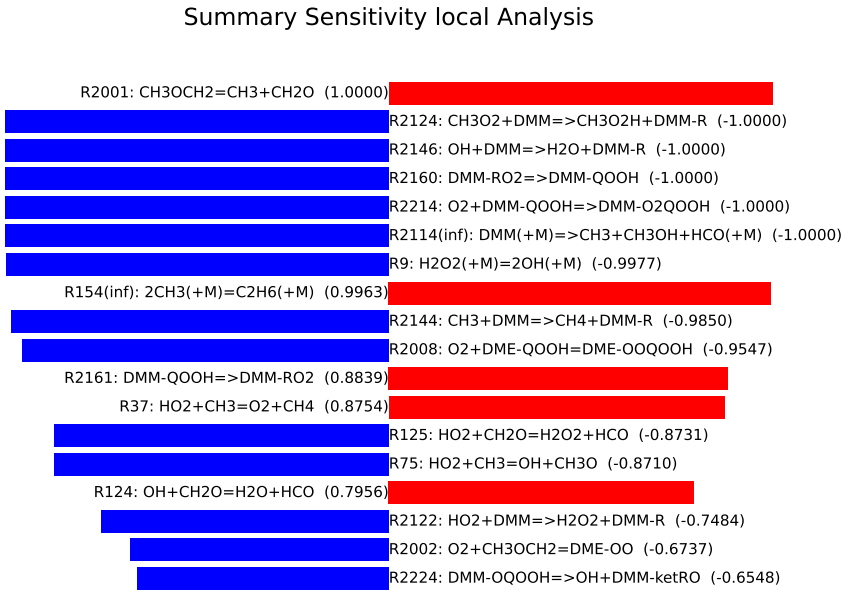

Figure 5.2: Sensitivity reactions for DMM at $P = 10atm$, $T = 600 - 1300K$ and $\phi = 1$.

too, in order to have a scheme valid for a mixture that can be used in a diesel engine.

5.2.3. Scaling factor

The crucial factor in creating a reduced kinetic mechanism is determining the appropriate scaling factor, which plays an important role in constructing a new kinetic scheme. To achieve this, the reference species must be thoroughly evaluated, using techniques such as experimental data, quantum chemical calculations, or *ab initio* calculations. Once this evaluation is completed for the identified classes, the scaling factor can be determined for the species of interest. By following this procedure, a balance can be achieved between accuracy and computational cost, enabling simulations of intricate chemical systems.

Bibliography

[1] H.-O. Pörtner, D.C. Roberts, E.S. Poloczanska, K. Mintenbeck, M. Tignor, A. Alegría, M. Craig, S. Langsdorf, S. Löschke, V. Möller, and A. Okem, editors. *Summary for Policymakers*. Cambridge University Press, Cambridge, UK and New York, NY, USA, 2022.

[2] Eurostat. *Energy, transport and environment statistics, 2019 edition*. Number 1. 2020.

[3] Hannah Ritchie, Max Roser, and Pablo Rosado. Energy. *Our World in Data*, 2022. https://ourworldindata.org/energy.

[4] Royal Society. *Sustainable synthetic carbon based fuels for transport - POLICY BRIEFING*. 2019.

[5] International Energy Agency. Global hydrogen review 2022. `https://www.iea.org/reports/global-hydrogen-review-2022`, 2022. License: CC BY 4.0.

[6] Daniel Himmel, Robin J. White, Eberhard Jacob, and Ingo Krossing. Highly correlated ab initio thermodynamics of oxymethylene dimethyl ethers (ome): formation and extension to the liquid phase. *Sustainable Energy Fuels*, 1:1177–1183, 2017.

[7] Kathrin Hackbarth, Philipp Haltenort, Ulrich Arnold, and Jörg Sauer. Recent progress in the production, application and evaluation of oxymethylene ethers. *Chemie Ingenieur Technik*, 90(10):1520–1528, 2018.

[8] Jakob Burger, Markus Siegert, Eckhard Ströfer, and Hans Hasse. Poly(oxymethylene) dimethyl ethers as components of tailored diesel fuel: Properties, synthesis and purification concepts. *Fuel*, 89(11):3315–3319, 2010.

[9] Sarah Deutz, Dominik Bongartz, Benedikt Heuser, Arne Kätelhön, Luisa Schulze Langenhorst, Ahmad Omari, Marius Walters, Jürgen Klankermayer, Walter Leitner, Alexander Mitsos, et al. Cleaner production of cleaner fuels: wind-to-wheel–environmental assessment of co 2-based oxymethylene ether as a drop-in fuel. *Energy & Environmental Science*, 11(2):331–343, 2018.

[10] Tianfeng Lu and Chung K. Law. Toward accommodating realistic fuel chemistry in large-scale computations. *Progress in Energy and Combustion Science*, 35(2):192–215, 2009.

[11] Andrea Bertolino. Optimization and uncertainty quantification of kinetic mechanisms for renewable fuels and sustainable combustion technologies. 2022.

[12] Alessandro Stagni, Steffen Schmitt, Matteo Pelucchi, Alessio Frassoldati, Katharina Kohse-Höinghaus, and Tiziano Faravelli. Dimethyl ether oxidation analyzed in a given flow reactor: Experimental and modeling uncertainties. *Combustion and Flame*, 240:111998, 2022.

[13] M.S. Bernardi, M. Pelucchi, A. Stagni, L.M. Sangalli, A. Cuoci, A. Frassoldati, P. Secchi, and T. Faravelli. Curve matching, a generalized framework for models/experiments comparison: An application to n-heptane combustion kinetic mechanisms. *Combustion and Flame*, 168:186–203, 2016.

[14] Paul D. Ronney. Effect of chemistry and transport properties on near-limit flames at microgravity. *Combustion Science and Technology*, 59(1-3):123–141, 1988.

[15] Magnus Fürst, Andrea Bertolino, Alberto Cuoci, Tiziano Faravelli, Alessio Frassoldati, and Alessandro Parente. Optismoke++: A toolbox for optimization of chemical kinetic mechanisms. *Computer Physics Communications*, 264:107940, 2021.

[16] Claudette M Rosado-Reyes and Wing Tsang. Shock tube study on the thermal decomposition of n-butanol. *The Journal of Physical Chemistry A*, 116(40):9825–9831, 2012.

[17] Mu Yujing and Abdelwahid Mellouki. Temperature dependence for the rate constants of the reaction of oh radicals with selected alcohols. *Chemical Physics Letters*, 333(1-2):63–68, 2001.

[18] Genny A Pang, Ronald K Hanson, David M Golden, and Craig T Bowman. Rate constant measurements for the overall reaction of oh+ 1-butanol→ products from 900 to 1200 k. *The Journal of Physical Chemistry A*, 116(10):2475–2483, 2012.

[19] Max R McGillen, William PL Carter, Abdelwahid Mellouki, John J Orlando, Bénédicte Picquet-Varrault, and Timothy J Wallington. Database for the kinetics of the gas-phase atmospheric reactions of organic compounds. *Earth System Science Data*, 12(2):1203–1216, 2020.

[20] Subith S Vasu, David F Davidson, Ronald K Hanson, and David M Golden. Measure-

ments of the reaction of oh with n-butanol at high-temperatures. *Chemical Physics Letters*, 497(1-3):26–29, 2010.

[21] Paula Jankowska, Krzysztof Jankowski, and Ewa Rudnicka Drożak. Alcohol use disorder manifestations and screening, August 2018.

[22] Sascha Jacobs, Malte Döntgen, Awad B.S. Alquaity, Wassja A. Kopp, Leif C. Kröger, Ultan Burke, Heinz Pitsch, Kai Leonhard, Henry J. Curran, and K. Alexander Heufer. Detailed kinetic modeling of dimethoxymethane. part ii: Experimental and theoretical study of the kinetics and reaction mechanism. *Combustion and Flame*, 205:522–533, 2019.

[23] Liming Cai, Sascha Jacobs, Raymond Langer, Florian vom Lehn, Karl Alexander Heufer, and Heinz Pitsch. Auto-ignition of oxymethylene ethers (omen, n = 2–4) as promising synthetic e-fuels from renewable electricity: shock tube experiments and automatic mechanism generation. *Fuel*, 264:116711, 2020.

[24] Fiona Rita Gillespie. An experimental and modelling study of the combustion of oxygenated hydrocarbons. *National University of Ireland*, 2014.

[25] Erjiang Hu, Zhenhua Gao, Yang Liu, Geyuan Yin, and Zuohua Huang. Experimental and modeling study on ignition delay times of dimethoxy methane/n-heptane blends. *Fuel*, 189:350–357, 2017.

[26] Jürgen Herzler, Mustapha Fikri, and Christof Schulz. High-pressure shock-tube study of the ignition and product formation of fuel-rich dimethoxymethane (dmm)/air and ch4/dmm/air mixtures. *Combustion and Flame*, 216:293–299, 2020.

[27] Lorena Marrodán, Eduardo Royo, Ángela Millera, Rafael Bilbao, and María U Alzueta. High pressure oxidation of dimethoxymethane. *Energy & Fuels*, 29(5):3507–3517, 2015.

[28] Florence H Vermeire, Hans-Heinrich Carstensen, Olivier Herbinet, Frédérique Battin-Leclerc, Guy B Marin, and Kevin M Van Geem. Experimental and modeling study of the pyrolysis and combustion of dimethoxymethane. *Combustion and Flame*, 190:270–283, 2018.

[29] Chris Fritsche, Krishna Prasad Shrestha, Sven Eckart, Fabian Mauss, and Hartmut Krause. Temperature and pressure dependency of the burning velocity in laminar premixed methanol and polyoxymethylene dimethyl ether (ome1, ome2, and ome3) flames. 2021.

[30] John M Ngugi, Sandra Richter, Marina Braun-Unkhoff, Clemens Naumann, Markus

Köhler, and Uwe Riedel. A study on fundamental combustion properties of oxymethylene ether-2. *Journal of Engineering for Gas Turbines and Power*, 144(1), 2022.

[31] Sven Eckart, Liming Cai, Chris Fritsche, Florian vom Lehn, Heinz Pitsch, and Hartmut Krause. Laminar burning velocities, co, and nox emissions of premixed polyoxymethylene dimethyl ether flames. *Fuel*, 293:120321, 2021.

[32] Wenyu Sun, Guoqing Wang, Shuang Li, Ruzheng Zhang, Bin Yang, Jiuzhong Yang, Yuyang Li, Charles K Westbrook, and Chung K Law. Speciation and the laminar burning velocities of poly (oxymethylene) dimethyl ether 3 (pomdme3) flames: An experimental and modeling study. *Proceedings of the Combustion Institute*, 36(1):1269–1278, 2017.

[33] Sandra Richter, Trupti Kathrotia, Marina Braun-Unkhoff, Clemens Naumann, and Markus Köhler. Study on the influence of oxymethylene ethers (omen) blending a diesel surrogate. In *Proceedings*, 2021.

[34] Krishna P Shrestha, Sven Eckart, Ayman M Elbaz, Binod R Giri, Chris Fritsche, Lars Seidel, William L Roberts, Hartmut Krause, and Fabian Mauss. A comprehensive kinetic model for dimethyl ether and dimethoxymethane oxidation and nox interaction utilizing experimental laminar flame speed measurements at elevated pressure and temperature. *Combustion and Flame*, 218:57–74, 2020.

[35] Ahmad Omari, Benedikt Heuser, Stefan Pischinger, and Christoph Rüdinger. Potential of long-chain oxymethylene ether and oxymethylene ether-diesel blends for ultra-low emission engines. *Applied Energy*, 239:1242–1249, 2019.

[36] IEA. Electricity market report - july 2022. *IEA*, 2022.

[37] European Council. Fir for 55, 2021.

[38] Venkata Yarlagadda, Huayang Zhu, Luming Ma, and Shijie Ge. Progress in hydrogen production via high-temperature electrolysis using solid oxide electrolysis cells: A review. *Journal of Energy Chemistry*, 56:165–177, 2021.

[39] Detlef Stolten and Joachim Scholta. Hydrogen production by solid oxide electrolysis cells (soec). *Chemical engineering science*, 63:2479–2499, 2008.

[40] Shantanu Shukla, Manas Pathak, K Suresh Kumar, Bhawana Singh, and Suman Sinha Ray. Proton exchange membrane electrolysis for hydrogen production: status and prospects. *Journal of Materials Chemistry A*, 8:19837–19868, 2020.

[41] Wenyu Sun, Guoqing Wang, Shuang Li, Ruzheng Zhang, Bin Yang, Jiuzhong Yang,

Yuyang Li, Charles K. Westbrook, and Chung K. Law. Speciation and the laminar burning velocities of poly(oxymethylene) dimethyl ether 3 (pomdme3) flames: An experimental and modeling study. *Proceedings of the Combustion Institute*, 36(1):1269–1278, 2017.

[42] M. Härtl, K. Gaukel, D. Pélerin, and et al. Oxymethylene ether as potentially co2-neutral fuel for clean diesel engines part 1: Engine testing. *MTZ Worldw*, 78:52–59, 2017.

[43] Gilles Prado, Jacques Lahaye, and Brian S Haynes. Soot particle nucleation and agglomeration. *Soot in combustion systems and its toxic properties*, pages 145–161, 1983.

[44] Sascha Jacobs, Malte Döntgen, Awad Bin Saud Alquaity, Raik Hesse, S. Kruse, Joachim Beeckmann, Leif C. Kröger, Philipp Morsch, Kai Leonhard, Heinz Pitsch, and Karl Alexander Heufer. A comprehensive experimental and kinetic modeling study of the combustion chemistry of diethoxymethane. *Energy & Fuels*, 2021.

[45] Wang Ying, Li Genbao, Zhu Wei, and Zhou Longbao. Study on the application of dme/diesel blends in a diesel engine. *Fuel Processing Technology*, 89(12):1272–1280, 2008.

[46] Wang HW, Zhou LB, Jiang DM, and Huang ZH. Study on the performance and emissions of a compression ignition engine fuelled with dimethyl ether. *Proceedings of the Institution of Mechanical Engineers, Part D: Journal of Automobile Engineering*, 89(214):101–106, 2000.

[47] Fritz Ullmann, editor. *Ullmann's Encyclopedia of Industrial Chemistry*. Wiley-VCH, Weinheim, 2006.

[48] Thomas Grützner, Hans Hasse, Neven Lang, Markus Siegert, and Eckhard Ströfer. Development of a new industrial process for trioxane production. *Chemical Engineering Science*, 62(18):5613–5620, 2007.

[49] Junzo Masamoto and Kazuhiko Matsuzaki. Development of methylal synthesis by reactive distillation. *JOURNAL OF CHEMICAL ENGINEERING OF JAPAN*, 27(1):1–5, 1994.

[50] Niklas Schmitz, Eckhard Strofer, Jakob Burger, and Hans Hasse. Conceptual design of a novel process for the production of poly (oxymethylene) dimethyl ethers from formaldehyde and methanol. *Industrial & Engineering Chemistry Research*, 56(40):11519–11530, 2017.

[51] Niklas Schmitz, Christian F Breitkreuz, Eckhard Strofer, Jakob Burger, and Hans Hasse. Separation of water from mixtures containing formaldehyde, water, methanol, methylal, and poly (oxymethylene) dimethyl ethers by pervaporation. *Journal of membrane science*, 564:806–812, 2018.

[52] Dorian Oestreich, Ludger Lautenschutz, Ulrich Arnold, and Jorg Sauer. Production of oxymethylene dimethyl ether (ome)-hydrocarbon fuel blends in a one-step synthesis/extraction procedure. *Fuel*, 214:39–44, 2018.

[53] George A. Olah. Towards oil independence through renewable methanol chemistry. *Angewandte Chemie International Edition*, 52(1):104–107, 2013.

[54] Jan-Oliver Weidert, Jakob Burger, Mario Renner, Sergej Blagov, and Hans Hasse. Development of an integrated reaction–distillation process for the production of methylal. *Industrial & Engineering Chemistry Research*, 56(2):575–582, 2017.

[55] Niklas Schmitz, Fabian Homberg, Jürgen Berje, Jakob Burger, and Hans Hasse. Chemical equilibrium of the synthesis of poly(oxymethylene) dimethyl ethers from formaldehyde and methanol in aqueous solutions. *Industrial & Engineering Chemistry Research*, 54(25):6409–6417, 2015.

[56] Benjamin G. Schieweck and Jürgen Klankermayer. Tailor-made molecular cobalt catalyst system for the selective transformation of carbon dioxide to dialkoxymethane ethers. *Angewandte Chemie International Edition*, 56(36):10854–10857, 2017.

[57] Katharina Thenert, Kassem Beydoun, Jan Wiesenthal, Walter Leitner, and Jürgen Klankermayer. Ruthenium-catalyzed synthesis of dialkoxymethane ethers utilizing carbon dioxide and molecular hydrogen. *Angewandte Chemie International Edition*, 55(40):12266–12269, 2016.

[58] Eliseo Ranzi, Carlo Cavallotti, Alberto Cuoci, Alessio Frassoldati, Matteo Pelucchi, and Tiziano Faravelli. New reaction classes in the kinetic modeling of low temperature oxidation of n-alkanes. *Combustion and Flame*, 162(5):1679–1691, 2015.

[59] Henry J. Curran. Developing detailed chemical kinetic mechanisms for fuel combustion. *Proceedings of the Combustion Institute*, 37(1):57–81, 2019.

[60] Stephen J. Klippenstein. From theoretical reaction dynamics to chemical modeling of combustion. *Proceedings of the Combustion Institute*, 36(1):77–111, 2017.

[61] Nick M Vandewiele, Kevin M Van Geem, Marie-Françoise Reyniers, and Guy B Marin. Genesys: Kinetic model construction using chemo-informatics. *Chemical Engineering Journal*, 207:526–538, 2012.

[62] Aurelio Rodríguez, Roberto Rodríguez-Fernández, Saulo A. Vázquez, George L. Barnes, James JP Stewart, and Emilio Martínez-Núñez. tsscds2018: A code for automated discovery of chemical reaction mechanisms and solving the kinetics. *Journal of Computational Chemistry*, 39(23):1922–1930, 2018.

[63] Ruben Van de Vijver and Judit Zádor. Kinbot: Automated stationary point search on potential energy surfaces. *Computer Physics Communications*, 248:106947, 2020.

[64] Michael Frenklach. Transforming data into knowledge—process informatics for combustion chemistry. *Proceedings of the Combustion Institute*, 31(1):125–140, 2007.

[65] Alison S. Tomlin. The role of sensitivity and uncertainty analysis in combustion modelling. *Proceedings of the Combustion Institute*, 34(1):159–176, 2013.

[66] Priyank Saxena and Forman A. Williams. Numerical and experimental studies of ethanol flames. *Proceedings of the Combustion Institute*, 31(1):1149–1156, 2007.

[67] Michael Frenklach, Hai Wang, and Martin J. Rabinowitz. Optimization and analysis of large chemical kinetic mechanisms using the solution mapping method—combustion of methane. *Progress in Energy and Combustion Science*, 18(1):47–73, 1992.

[68] T. Turányi, T. Nagy, I. Gy. Zsély, M. Cserháti, T. Varga, B. T. Szabó, I. Sedyó, P. T. Kiss, A. Zempléni, and H. J. Curran. Determination of rate parameters based on both direct and indirect measurements. *International Journal of Chemical Kinetics*, 44(5):284–302, 2012.

[69] L. Elliott, D.B. Ingham, A.G. Kyne, N.S. Mera, M. Pourkashanian, and C.W. Wilson. Genetic algorithms for optimisation of chemical kinetics reaction mechanisms. *Progress in Energy and Combustion Science*, 30(3):297–328, 2004.

[70] A. Bertolino, M. Fürst, A. Stagni, A. Frassoldati, M. Pelucchi, C. Cavallotti, T. Faravelli, and A. Parente. An evolutionary, data-driven approach for mechanism optimization: theory and application to ammonia combustion. *Combustion and Flame*, 229:111366, 2021.

[71] Liming Cai and Heinz Pitsch. Mechanism optimization based on reaction rate rules. *Combustion and Flame*, 161(2):405–415, 2014.

[72] Alberto Cuoci, Alessio Frassoldati, Tiziano Faravelli, ELISEO Ranzi, et al. Opensmoke: numerical modeling of reacting systems with detailed kinetic mechanisms. In *XXXIV meeting of the Italian Section of the Combustion Institute*, 2011.

[73] Edoardo Ramalli, Timoteo Dinelli, Andrea Nobili, Alessandro Stagni, Barbara Pernici, and Tiziano Faravelli. Automatic validation and analysis of predictive models by means of big data and data science. *Chemical Engineering Journal*, 454:140149, 2023.

[74] Ghobad Bagheri, Eliseo Ranzi, Matteo Pelucchi, Alessandro Parente, Alessio Frassoldati, and Tiziano Faravelli. Comprehensive kinetic study of combustion technologies for low environmental impact: Mild and oxy-fuel combustion of methane. *Combustion and Flame*, 212:142–155, 2020.

[75] Eliseo Ranzi, Alessio Frassoldati, Alessandro Stagni, Matteo Pelucchi, Alberto Cuoci, and Tiziano Faravelli. Reduced kinetic schemes of complex reaction systems: Fossil and biomass-derived transportation fuels. *International Journal of Chemical Kinetics*, 46:512–542, 2014.

[76] Matteo Pelucchi, Alessandro Stagni, and Tiziano Faravelli. Addressing the complexity of combustion kinetics: Data management and automatic model validation. In *Computer Aided Chemical Engineering*, volume 45, pages 763–798. Elsevier, 2019.

[77] Wayne K. Metcalfe, Sinéad M. Burke, Syed S. Ahmed, and Henry J. Curran. A hierarchical and comparative kinetic modeling study of c1c2 hydrocarbon and oxygenated fuels. *International Journal of Chemical Kinetics*, 45(10):638–675, 2013.

[78] Sinéad M. Burke, Ultan Burke, Reuben Mc Donagh, Olivier Mathieu, Irmis Osorio, Charles Keesee, Anibal Morones, Eric L. Petersen, Weijing Wang, Trent A. DeVerter, Matthew A. Oehlschlaeger, Brandie Rhodes, Ronald K. Hanson, David F. Davidson, Bryan W. Weber, Chih-Jen Sung, Jeffrey Santner, Yiguang Ju, Francis M. Haas, Frederick L. Dryer, Evgeniy N. Volkov, Elna J.K. Nilsson, Alexander A. Konnov, Majed Alrefae, Fethi Khaled, Aamir Farooq, Patricia Dirrenberger, Pierre-Alexandre Glaude, Frédérique Battin-Leclerc, and Henry J. Curran. An experimental and modeling study of propene oxidation. part 2: Ignition delay time and flame speed measurements. *Combustion and Flame*, 162(2):296–314, 2015.

[79] Ultan Burke, Kieran P. Somers, Peter O'Toole, Chis M. Zinner, Nicolas Marquet, Gilles Bourque, Eric L. Petersen, Wayne K. Metcalfe, Zeynep Serinyel, and Henry J. Curran. An ignition delay and kinetic modeling study of methane, dimethyl ether, and their mixtures at high pressures. *Combustion and Flame*, 162(2):315–330, 2015.

[80] Carlo Cavallotti, Matteo Pelucchi, Yuri Georgievskii, and Stephen J. Klippenstein. Estoktp: Electronic structure to temperature- and pressure-dependent rate

constants-a code for automatically predicting the thermal kinetics of reactions. *Journal of chemical theory and computation*, 15 2:1122–1145, 2019.

[81] J Nocedal and S Wright. Numerical optimization. 2nd edn springer. *New York*, 2006.

[82] Stephen Boyd, Stephen P Boyd, and Lieven Vandenberghe. *Convex optimization*. Cambridge university press, 2004.

[83] Diederik P Kingma, Jimmy Ba, Y Bengio, and Y LeCun. 3rd international conference on learning representations. *ICLR, San Diego*, 2015.

[84] Léon Bottou. Large-scale machine learning with stochastic gradient descent. In *Proceedings of COMPSTAT'2010: 19th International Conference on Computational StatisticsParis France, August 22-27, 2010 Keynote, Invited and Contributed Papers*, pages 177–186. Springer, 2010.

[85] Sebastian Ruder. An overview of gradient descent optimization algorithms. *arXiv preprint arXiv:1609.04747*, 2016.

[86] Michael JD Powell. An efficient method for finding the minimum of a function of several variables without calculating derivatives. *The computer journal*, 7(2):155–162, 1964.

[87] James Bergstra and Yoshua Bengio. Random search for hyper-parameter optimization. *Journal of machine learning research*, 13(2), 2012.

[88] Luis Miguel Rios and Nikolaos V Sahinidis. Derivative-free optimization: a review of algorithms and comparison of software implementations. *Journal of Global Optimization*, 56:1247–1293, 2013.

[89] Kalyanmoy Deb. *Multi-objective optimisation using evolutionary algorithms: an introduction*. Springer, 2011.

[90] Slowik A. and Kwasnicka H. Evolutionary algorithms and their applications to engineering problems. *Neural Comput and Applic*, 32:12363–12379, 2020.

[91] Thomas Bäck and Hans-Paul Schwefel. An overview of evolutionary algorithms for parameter optimization. *Evolutionary Computation*, 1(1):1–23, 1993.

[92] Edoardo Ramalli, Gabriele Scalia, Barbara Pernici, Alessandro Stagni, Alberto Cuoci, and Tiziano Faravelli. Data ecosystems for scientific experiments: managing combustion experiments and simulation analyses in chemical engineering. *Frontiers in big Data*, 4:663410, 2021.

[93] J. Ramsay and B.W. Silverman. *Functional Data Analysis*. Springer Series in Statistics. Springer New York, 2006.

[94] JS Urban Hjorth. *Computer intensive statistical methods: Validation model selection and bootstrap*. Chapman and Hall/CRC, 2017.

[95] Brian Adams, William Bohnhoff, Keith Dalbey, Mohamed Ebeida, John Eddy, Michael Eldred, Russell Hooper, Patricia Hough, Kenneth Hu, John Jakeman, et al. Dakota, a multilevel parallel object-oriented framework for design optimization, parameter estimation, uncertainty quantification, and sensitivity analysis: Version 6.13 user's manual. Technical report, Sandia National Lab.(SNL-NM), Albuquerque, NM (United States), 2020.

[96] M. Pelucchi, S. Namysl, E. Ranzi, A. Rodriguez, C. Rizzo, K. P. Somers, Y. Zhang, O. Herbinet, H. J. Curran, F. Battin-Leclerc, and T. Faravelli. Combustion of n-c3–c6 linear alcohols: An experimental and kinetic modeling study. part i: Reaction classes, rate rules, model lumping, and validation. *Energy & Fuels*, 34(11):14688–14707, 2020.

[97] Alessandro Stagni, Yu Song, Laurien A Vandewalle, Kevin M Van Geem, Guy B Marin, Olivier Herbinet, Frédérique Battin-Leclerc, and Tiziano Faravelli. The role of chemistry in the oscillating combustion of hydrocarbons: An experimental and theoretical study. *Chemical Engineering Journal*, 385:123401, 2020.

A | Species dictionary

Pseudospecies CHEMIKIN name	**Isomers name**
DMM	Dimetoxymethane (OME_1)
DMM-R	DMM alkyl radical
DMM-RO2	DMM peroxy radical
DMM-ROOH	DMM hydroperoxide
DMM-RO	DMM alkoxy radical
DMM-ket	DMM ketone
DMM-ketR	DMM ketone radical
DMM-cycleth	DMM cyclic ether
DMM-QOOH	DMM hydroperoxy-alkyl radical
DMM-O2QOOH	DMM hydroperoxy-alkyl-peroxy radical
DMM-OQOOH	DMM keto-hydroperoxide
CH3OCOOH	DME carboxylic acid
DMM-R2OOH	DMM dihydroperoxyl-alkyl radical
DMM-ketRO	DMM keto-alkoxy radical
DMM-cyclethOOH	DMM hydroperoxy cyclic ether
CH2OCHO	DME ketone radical
OME2	Oxymethilene ether 2
OME2-R	OME2 alkyl radical
OME2-RO2	OME2 peroxy radical
OME2-RO	OME2 alkoxy radical
OME2-QOOH	OME2 hydroperoxy-alkyl radical
OME2-ROOH	OME2 hydroperoxide
OME2-cycleth	OME2 cyclic ether
OME2-O2QOOH	OME2 hydroperoxy-alkyl-peroxy radical
OME2-OQOOH	OME2 keto-hydroperoxide
CH3OCH2OCOO	DMM keto-alkoxy radical

Pseudospecies CHEMIKIN name	Isomers name
OME3	Oxymethilene ether 3
OME3-R	OME3 alkyl radical
OME3-RO2	OME3 peroxy radical
OME3-RO	OME3 alkoxy radicals
OME3-QOOH	OME3 hydroperoxy-alkyl radical
OME3-ROOH	OME3 hydroperoxide
OME3-O2QOOH	OME3 hydroperoxy-alkyl-peroxy radical
OME3-OQOOH	OME3 keto-hydroperoxide
OME2-ketRO	OME2 keto-alkoxy radical
CH3OCH2OCH2OCHO	OME2 ketone
OME2-ketR	OME2 ketone radical
OME4	Oxymethilene ether 4
OME4-R	OME4 alkyl radical
OME4-RO2	OME4 peroxy radical
OME4-RO	OME4 alkoxy radical
OME4-QOOH	OME4 hydroperoxy-alkyl radical
OME4-ROOH	OME4 hydroperoxide
OME4-cycleth	OME4 cyclic ether
OME4-O2QOOH	OME4 hydroperoxy-alkyl-peroxy radical
OME4-OQOOH	OME4 keto-hydroperoxide
OME3-ketRO	OME3 keto-alkoxy radical
OME3-ketR	OME3 ketone radical
C4H9O4CHO	OME3 ketone

B | Summary of the sensitivity analysis

The results obtained with the local sensitivity analysis for the DMM P = 10 atm and equivalence ratio equal to 1 between T of 600-1300K are summarized in Tables below.

Sensitivity Coefficient	**Index**	**Reaction**
1.0000	R2001	CH3OCH2=CH3+CH2O
-1.0000	R2124	CH3O2+DMM=>CH3O2H+DMM-R
-1.0000	R2146	OH+DMM=>H2O+DMM-R
-1.0000	R2160	DMM-RO2=>DMM-QOOH
-1.0000	R2214	O2+DMM-QOOH=>DMM-O2QOOH
-1.0000	R2114(inf)	DMM(+M)=>CH3+CH3OH+HCO(+M)
-0.9977	R9	H2O2(+M)=2OH(+M)
0.9963	R154(inf)	2CH3(+M)=C2H6(+M)
-0.9850	R2144	CH3+DMM=>CH4+DMM-R
-0.9547	R2008	O2+DME-QOOH=DME-OOQOOH
0.8839	R2161	DMM-QOOH=>DMM-RO2
0.8754	R37	HO2+CH3=O2+CH4
-0.8731	R125	HO2+CH2O=H2O2+HCO
-0.8710	R75	HO2+CH3=OH+CH3O
0.7956	R124	OH+CH2O=H2O+HCO
-0.7484	R2122	HO2+DMM=>H2O2+DMM-R
-0.6737	R2002	O2+CH3OCH2=DME-OO
-0.6548	R2224	DMM-OQOOH=>OH+DMM-ketRO
-0.4982	R2115(inf)	DMM(+M)=CH2O+CH3OCH3(+M)
-0.4932	R126	CH3+CH2O=CH4+HCO
-0.4776	R2112(inf)	DMM(+M)=CH3+CH3OCH2O(+M)
0.4325	R2213	DMM-QOOH=>OH+CH2O+CH3OCHO
0.4307	R2007	DME-QOOH=>OH+2CH2O

Table B.1: Sensitivity coefficient until |0.40|

Sensitivity Coefficient	Index	Reaction name
0.3965	R20	2HO2=O2+H2O2
-0.3666	R2112	DMM(+M)=CH3+CH3OCH2O(+M)
0.3220	R131	O2+HCO=HO2+CO
-0.3016	R2113(inf)	DMM(+M)=CH3O+CH3OCH2(+M)
0.2854	R2006	DME-OO=>OH+2CH2O
-0.2811	R2118	O2+DMM=>HO2+DMM-R
0.2688	R22	H+O2(+M)=HO2(+M)
0.2580	R21	2HO2=O2+H2O2
-0.2543	R85	CH3O2H=OH+CH3O
-0.2492	R2142	H+DMM=>H2+DMM-R
-0.2490	R2022	O2+HCO=O2CHO
-0.2487	R2152	O2+DMM-R=>DMM-RO2
0.2292	R2148	DMM-R=>CH2O+CH3OCH2
-0.2240	R5	H+O2=O+OH
-0.2237	R2005	DME-OO=DME-QOOH
0.2210	R2153	DMM-RO2=>O2+DMM-R
0.2114	R114	O2+CH3O=HO2+CH2O
-0.1870	R2004	O2+CH3OCH2=>OH+2CH2O
0.1766	R130	HCO+M=H+CO+M
-0.1723	R2010	DME-OOQOOH=OH+DME-OQOOH
-0.1689	R68	O2+CH3=OH+CH2O
-0.1633	R81	CH3+CH3O2=2CH3O
-0.1625	R2027	HOCH2OCO=CO+HOCH2O
0.1618	R2026	HOCH2OCO=CO2+CH2OH
0.1498	R78	OH+CH3O2=O2+CH3OH
-0.1346	R9(inf)	H2O2(+M)=2OH(+M)
-0.1280	R141	CH3O(+M)=H+CH2O(+M)
-0.1223	R2126	CH3O+DMM=>CH3OH+DMM-R
-0.1195	R2011	DME-OQOOH=OH+OCH2OCHO
-0.1170	R2218	DMM-O2QOOH=>DMM-R2OOH
0.1084	R154	2CH3(+M)=C2H6(+M)
0.1001	R2167	2DMM-RO2=>O2+2DMM-RO
0.0993	R2216	DMM-O2QOOH=>OH+DMM-OQOOH
0.0970	R18	OH+HO2=O2+H2O
-0.0931	R129	CH3O2+CH2O=CH3O2H+HCO
0.0871	R1639	OH+CH3OCHO=>H2O+CH2O+HCO
0.0849	R2209	DMM-QOOH=>OH+DMM-cycleth
-0.0807	R2220	DMM-R2OOH=>OH+CH2O+DME-OQOOH
-0.0790	R2114	DMM(+M)=>CH3+CH3OH+HCO(+M)
0.0783	R2163	HO2+DMM-RO2=>O2+DMM-ROOH
0.0782	R2219	DMM-R2OOH=>DMM-O2QOOH

Table B.2: Sensitivity coefficient until |0.075|

C | Supplementary Material

In this appendix, additional validation is presented to confirm the consistency of the results obtained.

C.1. DMM

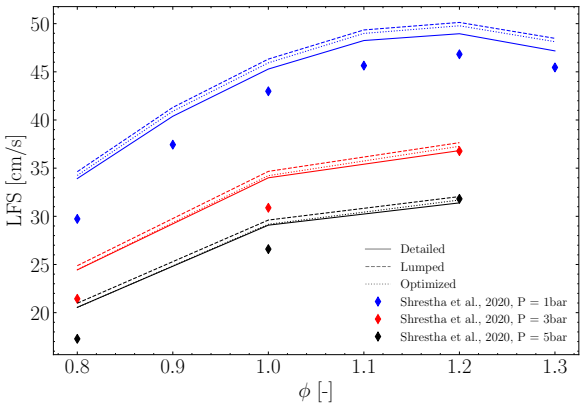

(a) LFS of DMM/Air at 1, 3 and 5 bar and 298 K.

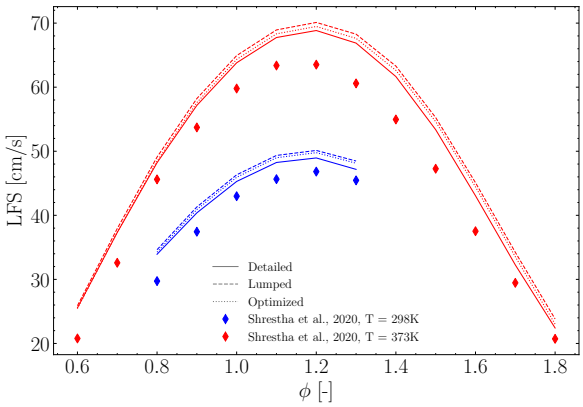

(b) LFS of DMM/Air at 1 bar, 298 K and 373 K.

Figure C.1: LFS measured by Shrestha et al. [34], compared with the detailed mechanism (solid line), the lumped one (dashed line) and the optimized too (dotted line). DMM is diluted in Air.

D | Optimized Reactions

In the table D.1 are presented the values of the lumped and optimized mechanisms.

		Lumped			**Optimized**		
Class	Species	A	β	Eatt/R	A	β	Eatt/R
H-abstraction by **OH**	OME_1	$8.52{\cdot}10^{2}$	3.21	-1860.85	$4.58{\cdot}10^{2}$	3.17	-1866.21
	OME_2	$2.91{\cdot}10^{2}$	3.33	-2002.62	$1.58{\cdot}10^{2}$	3.29	-2149.56
	OME_3	$5.20{\cdot}10^{2}$	3.27	-1926.05	$2.76{\cdot}10^{2}$	3.23	-2008.48
	OME_4	$8.22{\cdot}10^{2}$	3.22	-1870.32	$4.40{\cdot}10^{2}$	3.18	-1891.45
H-abstraction by **H**	OME_1	$1.30{\cdot}10^{6}$	2.44	4826.49	$4.11{\cdot}10^{6}$	2.38	4570.93
	OME_2	$1.57{\cdot}10^{6}$	2.31	4915.92	$4.56{\cdot}10^{6}$	2.25	4719.35
	OME_3	$4.55{\cdot}10^{6}$	2.2	4986.44	$1.33{\cdot}10^{7}$	2.15	4863.01
	OME_4	$8.26{\cdot}10^{6}$	2.15	5010.74	$2.68{\cdot}10^{7}$	2.09	4858.39
H-abstraction by **O**	OME_1	$3.31{\cdot}10^{6}$	2.36	2893.49	$1.30{\cdot}10^{6}$	2.38	2887.88
	OME_2	$4.34{\cdot}10^{6}$	2.39	2877.00	$1.71{\cdot}10^{6}$	2.41	2871.39
	OME_3	$5.38{\cdot}10^{6}$	2.40	2864.70	$2.12{\cdot}10^{6}$	2.42	2859.09
	OME_4	$6.48{\cdot}10^{6}$	2.41	2857.18	$2.55{\cdot}10^{7}$	2.43	2851.57
H-abstraction by $\mathbf{HO_2}$	OME_1	$3.69{\cdot}10^{1}$	3.48	11740.74	$2.91{\cdot}10^{1}$	3.43	11826.06
	OME_2	$4.79{\cdot}10^{2}$	3.38	11702.84	$3.78{\cdot}10^{2}$	3.33	11788.16
	OME_3	$9.69{\cdot}10^{2}$	3.33	11704.44	$7.64{\cdot}10^{2}$	3.28	11789.76
	OME_4	$1.57{\cdot}10^{3}$	3.29	11710.13	$1.24{\cdot}10^{3}$	3.24	11795.45
H-abstraction by $\mathbf{O_2}$	OME_1	$3.40{\cdot}10^{5}$	2.50	39872.39	$3.11{\cdot}10^{5}$	2.50	40558.68
	OME_2	$5.35{\cdot}10^{7}$	2.08	40249.38	$4.90{\cdot}10^{7}$	2.08	40935.67
	OME_3	$9.72{\cdot}10^{7}$	2.06	40277.11	$8.91{\cdot}10^{7}$	2.06	40963.40
	OME_4	$1.43{\cdot}10^{8}$	2.04	40292.61	$1.31{\cdot}10^{8}$	2.04	40978.90
H-abstraction by $\mathbf{CH_3}$	OME_1	$6.27{\cdot}10^{0}$	3.57	7579.45	$1.58{\cdot}10^{1}$	3.55	8048.29
	OME_2	$1.66{\cdot}10^{2}$	3.39	7733.01	$4.18{\cdot}10^{2}$	3.37	8201.85
	OME_3	$4.13{\cdot}10^{2}$	3.31	7800.83	$1.04{\cdot}10^{3}$	3.29	8269.67
	OME_4	$7.34{\cdot}10^{2}$	3.27	7840.14	$1.85{\cdot}10^{3}$	3.25	8308.98
H-abstraction by $\mathbf{CH_3O_2}$	OME_1	$2.93{\cdot}10^{1}$	3.49	11740.47	$6.53{\cdot}10^{1}$	3.05	7741.46
	OME_2	$1.67{\cdot}10^{1}$	3.61	12089.53	$5.28{\cdot}10^{1}$	3.54	11802.51
	OME_3	$1.96{\cdot}10^{1}$	3.60	11964.50	$6.19{\cdot}10^{1}$	3.53	11677.48
	OME_4	$2.44{\cdot}10^{1}$	3.58	11886.55	$7.71{\cdot}10^{1}$	3.51	11599.53

Table D.1: Kinetic constant parameters for the 7 classes identified, for the nominal mechanism and the optimized one.

E | K check

In Figures E.1, E.2, E.3 and E.4 the check for the optimized reactions is presented per each specie.

E.1. DMM

The evaluation conducted for each reaction involved in the optimization of DMM can be observed in Figure E.1. The temperature range taken into account spans from 500 K to 2000 K.

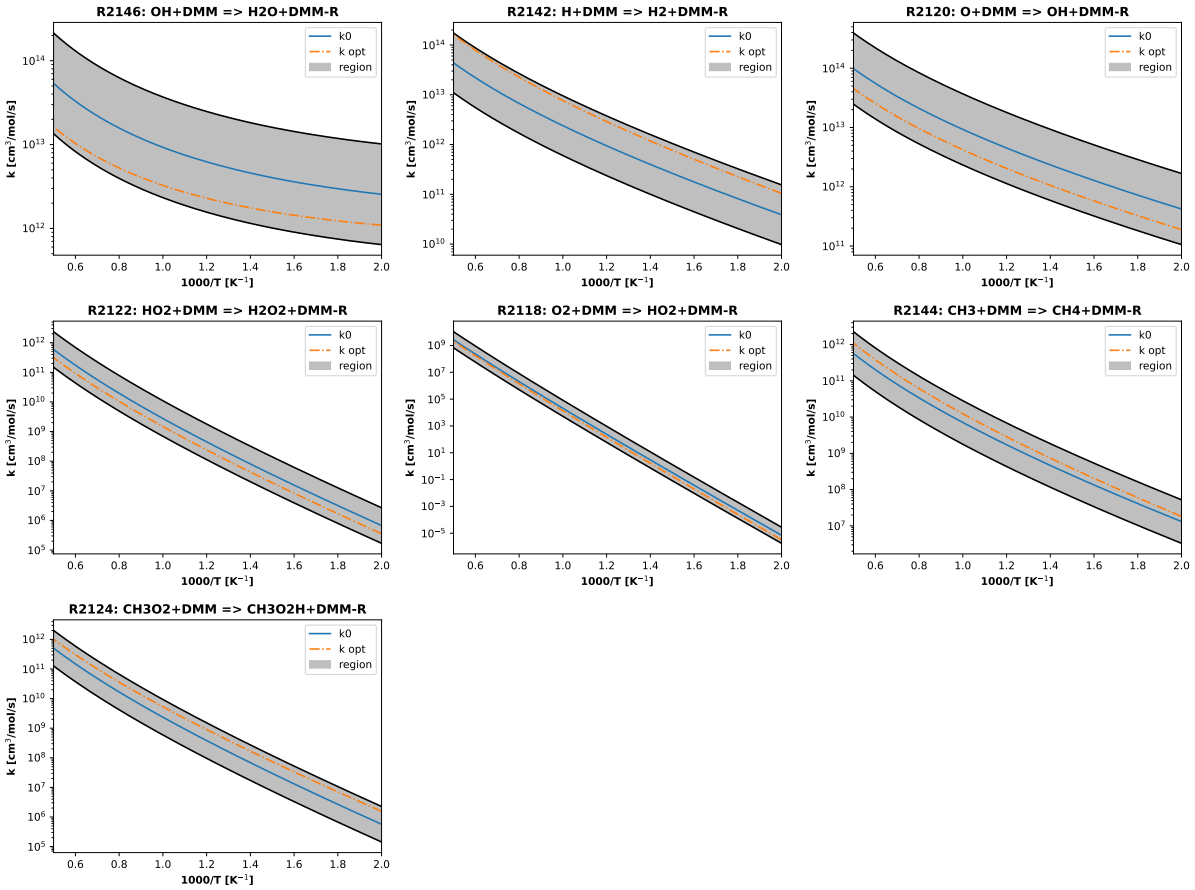

Figure E.1: Comparison between lumped (in blue, straight line) and optimized mechanism (in orange, dotted line) for considered reactions during optimization dor DMM.

E.2. OME_2

The evaluation conducted for each reaction involved in the optimization of OME_2 can be observed in Figure E.2. The temperature range taken into account spans from 500 K to 2000 K.

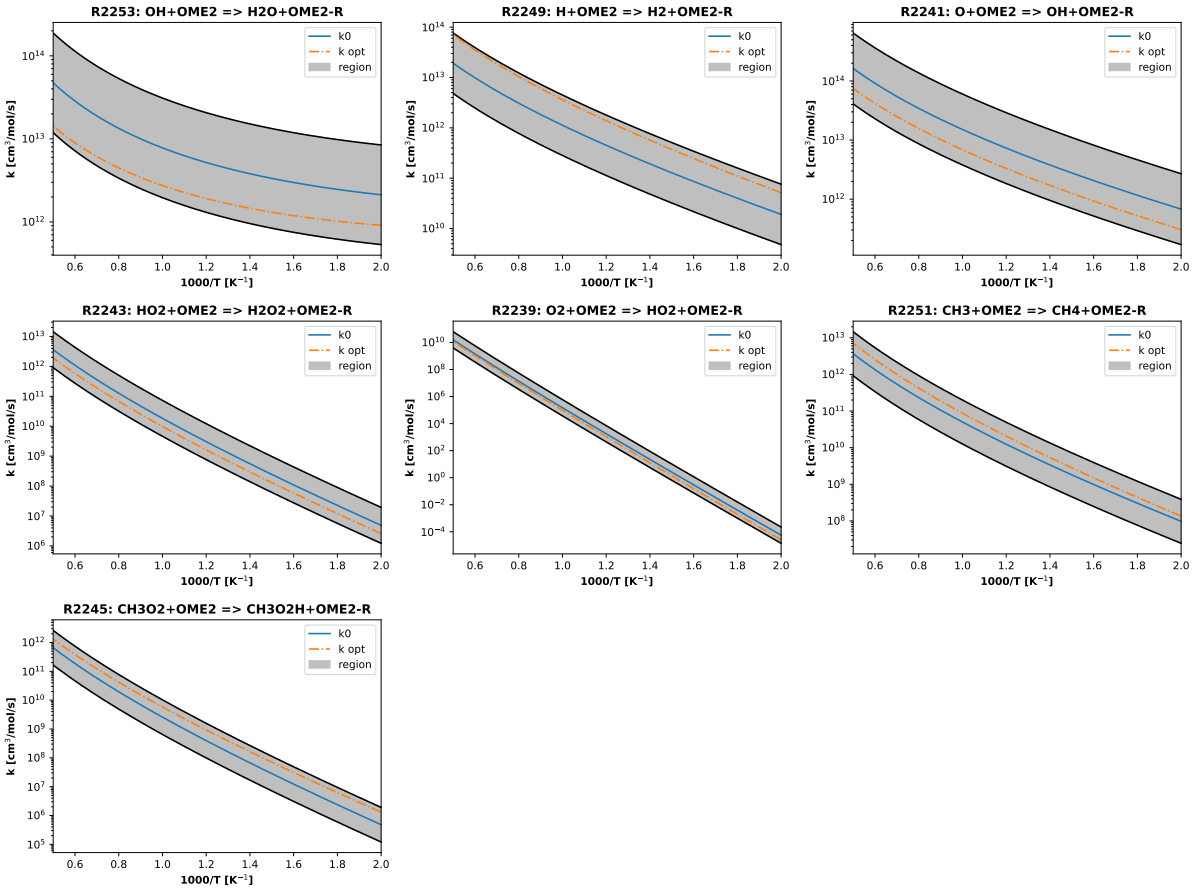

Figure E.2: Comparison between lumped (in blue, straight line) and optimized mechanism (in orange, dotted line) for considered reactions during optimization for OME_2.

E.3. OME_3

The evaluation conducted for each reaction involved in the optimization of OME_3 can be observed in Figure E.3. The temperature range taken into account spans from 500 K to 2000 K.

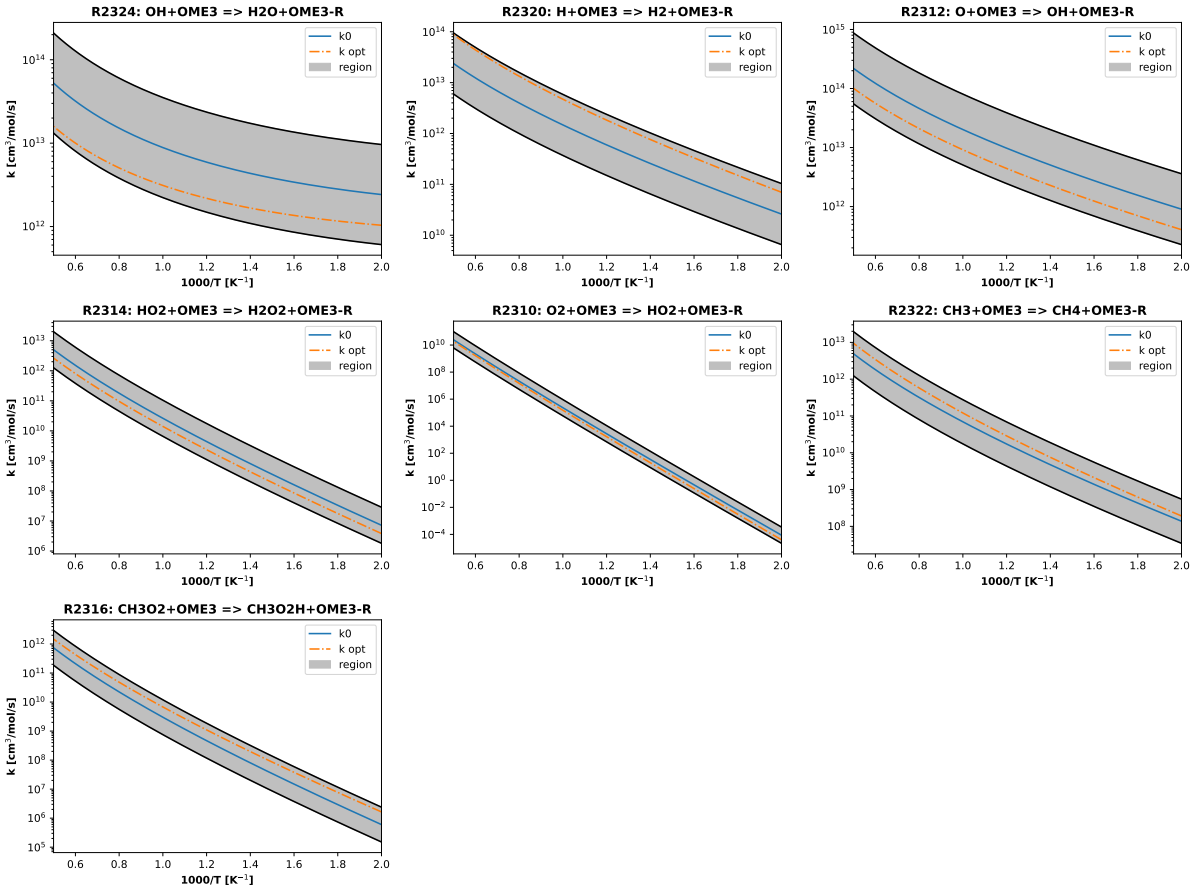

Figure E.3: Comparison between lumped (in blue, straight line) and optimized mechanism (in orange, dotted line) for considered reactions during optimization for OME_3.

E.4. OME_4

The evaluation conducted for each reaction involved in the optimization of OME_4 can be observed in Figure E.4. The temperature range taken into account spans from 500 K to 2000 K.

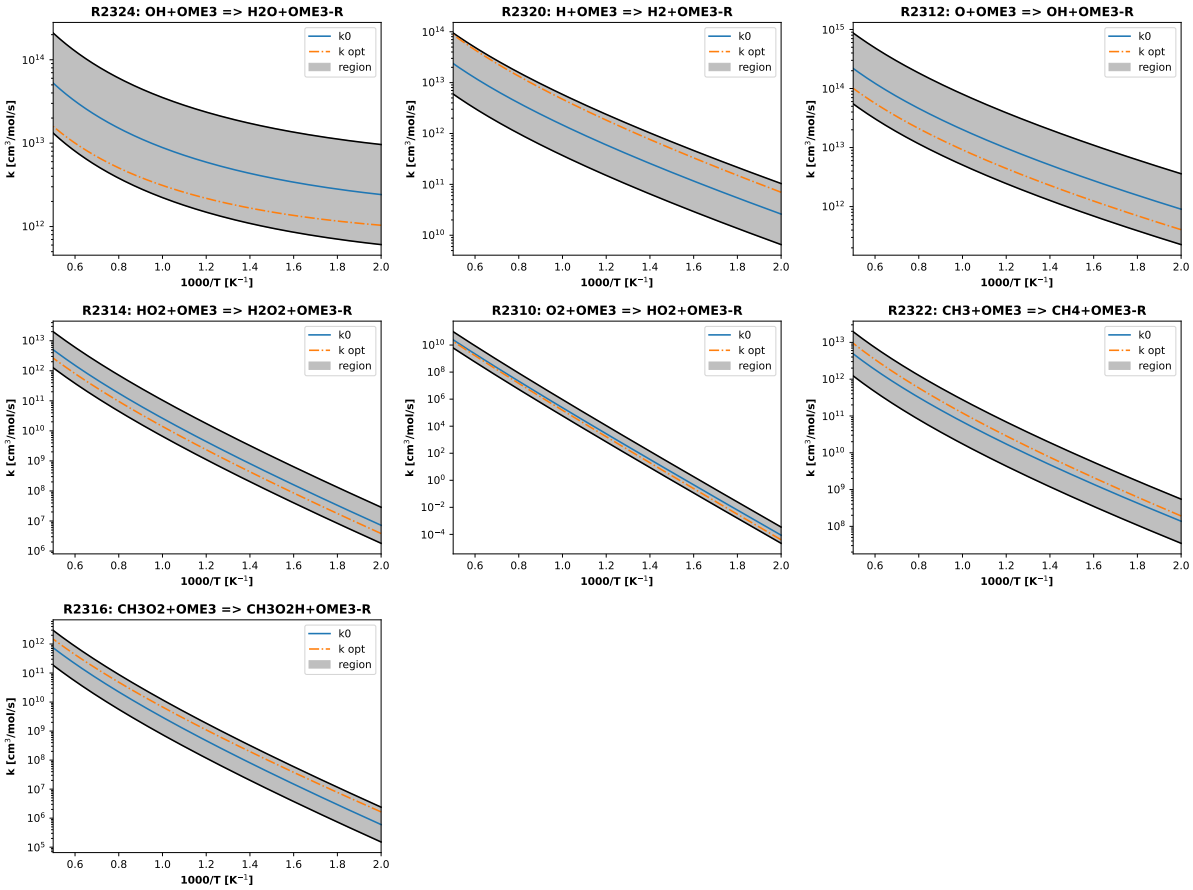

Figure E.4: Comparison between lumped (in blue, straight line) and optimized mechanism (in orange, dotted line) for considered reactions during optimization for OME_4.

Acknowledgements

I would like to take this opportunity to express my sincere gratitude to all those who have provided me with invaluable support and guidance throughout this journey.

First and foremost, I would like to thank my supervisor Professor Alessandro Stagni for his constant encouragement, invaluable insights, and expert guidance throughout my thesis. His unwavering support has been a great source of motivation and inspiration for me. I would also like to thank Professor Tiziano Faravelli for his invaluable support through the development of the Framework here proposed.

I would also like to express my sincere appreciation to the two Ph.D. candidates, Timoteo Dinelli and Alessandro Pegurri, who generously shared their knowledge, expertise and endless support, which significantly contributed to the success of my research. A special thanks to all the guys of the `Creck modeling` research group because they make me feel part of a family.

I am also deeply grateful to my family, who provided me with unconditional love, support, and encouragement throughout my academic journey. Their unwavering belief in me has been a constant source of strength, and I could not have completed this thesis without their support.

Many thanks also go to my two best friends, Lorenzo e Riccardo, who have been there for me every step of the way. Their unwavering support and encouragement, especially during these tough times, have been invaluable.

Thanks to Giacomo, Andrea, Alessio and Matteo for the days and nights spent in BCL and not only.

I would also like to thank my roommates, Filippo e Dario, who provided me with a supportive living environment, making it possible for me to focus but also to enjoy the sweet Italian doing nothing.

Lastly, I would like to express my deepest gratitude to my girlfriend Allegra, whose unwavering love, support, and encouragement kept me motivated and inspired throughout all these years. You always make me feel at home.